Modelling and control of contact in magnetic bearing/flexible rotor systems

Abulrub, Abdul-Hadi G.

Award date:
2006

Awarding institution:
University of Bath

MODELLING AND CONTROL OF CONTACT IN MAGNETIC BEARING/FLEXIBLE ROTOR SYSTEMS

Submitted by Abdul-Hadi G. Abulrub

for the degree of

Doctor of Philosophy

of the University of Bath

2006

ProQuest LLC
789 East Eisenhower Parkway
P.O. Box 1346
Ann Arbor, MI 48106-1346

Acknowledgments

I have been in the magnetic bearing group since I started my MSc. in Dynamic and Control in 2001. The first person I would like to thank is my principal supervisor Dr M. Necip Sahinkaya. During these past few years I have known Dr Sahinkaya to be a sympathetic and principle-centred person. His enthusiastic and critical observation on research and his mission to provide nothing less than the highest quality of work has made a tremendous impression on me. I owe him a great deal of gratitude for having shown me this methodology. He will not realise how much I have gained from him.

Besides being an outstanding supervisor and exceptional research advisor, Dr Sahinkaya has been as close as a relative and as good as a true friend to me. He represents the epitome of a research supervisor and others should learn from his example. I am very pleased that I have had the opportunity in my life to learn from and work with him.

I would like to express gratefulness to my co-supervisor Dr Patrick S. Keogh, for his inspiring and encouraging way to guide me to a deeper understanding of knowledge, and his invaluable comments during the whole work with this thesis. He was responsible for involving me in the magnetic bearing group in the first place. He demonstrated to me distinctive means to undertake a research problem and the need to be persistent to accomplish its objectives.

I feel a profound sense of appreciation for my father and mother who formed my vision and taught me the good morals that truly matter in life. Their unconditional support and encouragement provide a persistent inspiration for my journey in this life. I am grateful for my six brothers and a sister for rendering me the sense and the value of brotherhood. I also sense exceptional appreciation to an old family friend, Mr Ali S. Alhusseni who for all time has supported my decision and always reminds me that it is essential to recognise the implications of our science beyond the narrow path of academic research to serve good purposes for all humankind.

I am deeply obliged for my wife Ann W. Almomani, for her boundless love and unlimited patience during the PhD. One of the best experiences is that we lived through this hard and complex period successfully. I am delighted and amazed for her distinguished achievement in her dental studies while her commitment towards supporting me with love and understanding was always her first priority.

Sincere Regards,

Abdul-Hadi Abulrub
Bath, England
2006

Publications

As a result of the work reported in this thesis, the following journal and conference publications have been produced:

- M. N. Sahinkaya, **A. G. Abulrub**, P. S. Keogh and C. R. Burrows, "Multiple sliding and rolling contact dynamics for a flexible rotor/magnetic bearing system," Accepted for publication in the IEEE-ASME Transactions on Mechatronics.
- **A. G. Abulrub**, M. N. Sahinkaya, C. R. Burrows and P. S. Keogh, "Adaptive control of active magnetic bearings to prevent rotor-bearing contact," ASME International Mechanical Engineering Congress and Exposition, 5-10, November 2006, Chicago, Illinois.
- **A. G. Abulrub**, M. N. Sahinkaya, P. S. Keogh and C. R. Burrows, "A constrained Lagrangian approach for modelling multiple contacts of flexible rotors," The Seventh IFToMM Conference on Rotor Dynamics, 25-28, September 2006, Vienna, Austria.

- **A. G. Abulrub**, M. N. Sahinkaya, P. S. Keogh and C. R. Burrows, "Contact dynamics and recursive open loop adaptive controller to recover rotor position," The Tenth International Symposium on Magnetic Bearings, 21-23, August 2006, Martigny, Switzerland.

- **A. G. Abulrub**, M. N. Sahinkaya, P. S. Keogh and C. R. Burrows, "Effective model reduction for magnetically levitated flexible rotors including contact dynamics," Proceedings of ASME 2005 International Design Engineering Technical Conferences and Computers and Information in Engineering Conference, 24-28 September 2005, Long Beach, USA.

- M. N. Sahinkaya, **A. G. Abulrub** and P. S. Keogh, "Performance of synchronous controllers for rotor magnetic bearing systems under retainer bearing contact," The Seventh International Conference on Motion and Vibration Control (MOvIC' 04), 8-11 August 2004, St.Louis, USA.

- M. N. Sahinkaya, **A. G. Abulrub** and P. S. Keogh, "On the modelling of flexible rotor/magnetic bearing systems when in contact with retainer bearings," The Ninth International Symposium on Magnetic Bearings (ISMB9), 3-6 August 2004, Lexington, Kentucky, USA.

Abstract

Active Magnetic Bearings (AMBs) have industrial interest in high-speed machinery due to their advantages of no mechanical contact, no need for lubrication, high precision operation, and ability to operate at high rotational speeds. An AMB levitates a rotor by means of electro-magnetic forces at an equilibrium position at which all forces acting on the rotor are balanced. The principle of active control is to measure the rotor position; any deviation will influence the magnetic flux, which is then altered to control the rotor position. Despite many inherent advantages, active magnetic bearings suffer from limited force capacity. This restricts their applications when sudden external impacts are expected, or when a sudden change of unbalance occurs. in these cases, the rotor may make contact with an auxiliary bearing, which introduces non-linear dynamics.

This thesis details research undertaken to investigate the behaviour of a rotor in an AMB system when contact occurs with auxiliary bearings. Several techniques have been reported to examine the contact dynamics modelling, most of them represented the contact dynamics with non-linear stiffness and damping elements. These characteristics lead to computationally inefficiency. A possible approach to improve matters is to use Lagrange's energy method and introduce constraints on the system. The constrained Lagrangian equations of motion do not require the modelling of the contact forces. When contact occurs, a constraint on the generalised coordinates and the constrained equations are added to the equations

of motion through Lagrange multipliers. Contact forces are automatically calculated using the Lagrange multipliers, which are evaluated during the solution of algebraic differential equations of the system.

Smaller AMB clearance increases force capacity, but requires more precise control to prevent the machine from entering abnormal operation. A well-known open loop adaptive controller has been developed utilising a recursive Fourier transform algorithm. A recursive open loop adaptive controller is introduced to increase the speed of the controller action to changes in the vibration levels. The developed recursive open loop adaptive control strategy was examined in simulation environment and implemented experimentally.

Reduced order models are required for controller design purposes to allow practical realization and implementation in real-time applications. In the rotor dynamics field, the controllers associated with magnetic bearings are classic examples of such a requirement. A technique is introduced to reduce the order of a finite element rotor model to one involving only the required rectilinear displacements in sensor and controller nodal planes. The reduced order model is shown to predict a number of natural frequencies and responses to step changes in unbalance with considerable accuracy. The simulated rotor response for the full and reduced order model are shown to be similar.

The simulated contact of the rotor with a retainer bearing was achieved with the reduced order model. The use of a constrained Lagrangian multiplier effectively considers the retainer bearing to be a rigid boundary. The simulation results were obtained for all various scenarios; non contact, single contact, multiple contact, and backward whirl. The same cases were tested with the new designed controller. The experimental work validates the novel contact modelling technique as it is in agreement with the simulation. The experimental results show the benefits of the control technique with the ability to recover rotor position from contact and even prevent it under certain conditions.

Preface

This PhD thesis is split into seven main chapters:

Chapter 1 [Introduction]

In this chapter the author provides a literature review of rotor contact behaviour in retainer bearings in magnetic bearing systems. The author presents previous research work on impact, which uses a classical theory to model the problem. The importance of Lagrange multipliers in other fields covers studies on different physical parameters that affect the problem, including friction. The author presents a brief survey of various control techniques, which have been applied to magnetic bearing systems for vibration attenuation purposes.

Chapter 2 [Experimental Flexible Rotor-Magnetic Bearing Setup]

This chapter illustrates the experimental facilities in the Centre for Power Transmission and Motion Control, which was used for the experimental work. The author provides the design specification of the rotor and magnetic bearings. Magnetic bearing modelling and controller hardware com-

ponents are also explained.

Chapter 3 [System Modelling and Model Reduction Technique]

The author details the modelling of the rotor using the finite element method (FEM). The FEM model accuracy is investigated. A novel model condensation techniques was developed and tested for rotor/bearing systems. The technique accuracy was examined in both the frequency and time domains.

Chapter 4 [Contact Dynamic Analysis and Modelling]

In this chapter the author explains various classical contact approaches that depend on high stiffness and damping to model the contact dynamic behaviour. The author points out the deficiencies of the classical approaches. This chapter introduces a detailed explanation of a new modelling technique through the use of Lagrange multipliers. The constrained Lagrangian approach was used to model single and multiple contact occurrence. The proposed technique was used to model destructive backward whirl. Simulation results are presented and discussed.

Chapter 5 [ROLAC Control Algorithm Design]

Open loop adaptive control (OLAC) is explained. In this thesis, the OLAC technique was developed to improve the performance of the controller. It increases the speed of the controller to update its optimal force for vibration attenuation. It uses the recursive Fourier transform. The recursive open loop adaptive controller (ROLAC) is fast and effective in vibration attenuation, preventing contact and recovering rotor position from contact. Simulation results are presented and discussed.

Chapter 6 [Real-Time Implementation of ROLAC Control]

This chapter is concerned with explaining all aspects of real-time implementation of the recursive open loop adaptive controller (ROLAC). Experimental verification of the theoretical results shown in the previous chapter is demonstrated and discussed.

Chapter 7 [Conclusions and Future Work]

The main conclusions are discussed and key areas of consideration for future work are drawn.

Nomenclature

Roman Letters

A_e	Effective area of magnetic bearing pole	m^2
B	Flux density in magnetic bearing coil	T
C_b	Effective damping coefficient of magnetic bearing	Ns/m
C_r	Retainer bearing clearance	m
F	Attractive force generated by one coil	N
F_c	Contact normal force between journal and inner-race of retainer bearing	N
F_f	Friction force between journal and retainer bearing	N
f_o	Fundamental frequency	Hz
H_{gap}	The magnetic field strength in the air gap	A/m
I	Coil current	A
I_b, I_c	Bias and control current	A

I_s	Static current to balance rotor weight	A
Im	The imaginary part of a complex number	
j	$\sqrt{-1}$	
K_b	Effective stiffness coefficient of magnetic bearing	N/m
K_c	Contact stiffness	N/m
K_i	Current gain of the magnetic bearing	N/A
k_p, k_i, k_d	PID controller proportional, integral and derivative gains	
K_s	Negative stiffness of the magnetic bearing	N/m
L	The coil inductance	H
l_{gap}	Air gap length (radial clearance)	m
l_{iron}	Half of total magnetic path length	m
N	Number of turns per coil	
N_b	An integer number indicating bits per cycle	
N_{per}	Number of synchronous cycles for the rotor to reach steady state	
R_c	The coil resistance	Ω
R_e	The real part of a complex number	
R_s	Radius of journal	m
S	The sensitivity function	
T	Periodic Time	
t	Time	sec
t_{abs}	Absolute time	sec

t_{halt}	A predefined period of time before the estimation is halted	sec
x, y	Rectilinear rotor displacements	m
$\mathbf{a}_n$	Sine component vector of the Fourier transform	
$\mathbf{B}_d$, $\mathbf{B}_u$	Rotor forces distribution matrices (direct and control)	
$\mathbf{b}_n$	Cosine component vector of the Fourier transform	
$\mathbf{C}$	Symmetric positive semi-definite damping matrix	Ns/m
$\mathbf{C}_m$	Measurement coefficient matrix	
$\mathbf{C}_R$	Reduced damping matrix	Ns/m
$\mathbf{C}_{mm}$, $\mathbf{C}_{ms}$, $\cdots$	Sub-damping matrices of $\mathbf{C}$	Ns/m
$\mathbf{F}_d$	Complex amplitude vector of direct forces acting on the rotor	N
$\mathbf{f}_d$	Vector of direct forces acting on the rotor	N
$\mathbf{f}_R$	Reduced vector of external forcing	N
$\mathbf{f}_m$, $\mathbf{f}_s$	Sub-force vectors of $\mathbf{f}_d$	N
$\mathbf{G}$	Symmetric positive semi-definite gyroscopic matrix	Ns/m
$\mathbf{G}_R$	Reduced gyroscopic matrix	Ns/m
$\mathbf{G}_{ss}$	Sub-gyroscopic matrix of $\mathbf{G}$	Ns/m
$\mathbf{H}$	The system dynamic control matrix	

$\mathbf{I}_p$, $\mathbf{I}_t$	Polar and Translatory moment of inertia of the disks	kgm^2
$\mathbf{J}$	Jacobian row vector of the constrained equation	
$\mathbf{K}$	Symmetric positive semi-definite stiffness matrix	N/m
$\mathbf{K}_R$	Reduced stiffness matrix	N/m
$\mathbf{K}_{mm}$, $\mathbf{K}_{ms}$, $\cdots$	Sub-stiffness matrices of $\mathbf{K}$	N/m
$\mathbf{M}$	Symmetric positive definite mass matrix	kg, kgm^2
$\mathbf{M}_R$	Reduced mass matrix	kg, kgm^2
$\mathbf{M}_{mm}$, $\mathbf{M}_{ms}$, $\cdots$	Sub-mass matrices of $\mathbf{M}$	kg, kgm^2
$\mathbf{Q}$	Complex synchronous rotor response	m, rad
$\mathbf{q}$	Vector of rotor responses	m, rad
$\mathbf{Q}_m$	Complex synchronous response at measurement sites	m, rad
$\mathbf{q}_m$, $\mathbf{q}_s$	Sub-state vectors of $\mathbf{q}$	m, rad
$\mathbf{R}$	The complex partial receptance matrix	
$\mathbf{R}_D$, $\mathbf{R}_E$	Model reduction matrices	
$\mathbf{U}$	Complex synchronous control force vector	N
$\mathbf{u}$	Vector of control forces	N

Greek Letters

α	The integral gain of ROLAC control	
β	Half angle between double pole faces	rad
Δ	Influence coefficient (receptance) matrix	N/m
δ_i	Deformation at the contact point	m
γ	Phase shift in SPHS	rad
λ	Lagrange multiplier	
μ	Coulomb coefficient of friction	
μ_o	Permeability of free space	Vs/Am
μ_r	Relative permeability of iron	
Ω	Rotor rotational frequency	rad/s
ω	Angular frequency	rad/s
ω_{coil}	The coil cutoff frequency	rad/s
π	Ratio of a circle's circumference to its diameter	
ψ	Phase shift	rad
θ, ϕ	Angular rotor displacements	rad
υ	Relative tangential velocity between journal and retainer bearing	m/s^2
ε	Coefficient of restitution	
ϑ	Angle of incidence at contact point	rad

Abbreviations

ADC	Analogue to digital convertor
AMB	Active magnetic bearing
DAC	Digital to analogue convertor
FEM	Finite element method
GUI	Graphical user interface
MB1	Non driven side magnetic bearing
MB2	Motor side magnetic bearing
MSDC	Modified static condensation in displacement space
OLAC	Open loop adaptive control
PD	Proportional - derivative
PDEs	Partial differential equations
PID	Proportional - integral - derivative
PWM	Pulse width modulation
ROLAC	Recursive open loop adaptive control
RTI	Real time interface
SDC	Static condensation in displacement space
SPHS	Schroeder phased harmonic sequence

Contents

1 Introduction **1**

1.1 Background on AMB Systems 2

1.2 Control Issues in AMB Systems 7

1.3 Faults in AMB systems 11

1.3.1 System Internal Malfunctions 12

1.3.2 System External Malfunctions 13

1.4 Contact Dynamic Modelling 14

1.5 Project Aims and Objectives 19

2 Experimental Flexible Rotor/Magnetic Bearing Setup **21**

2.1 Design Requirements and System Outline 21

2.2 Magnetic Bearing Modelling 23

2.3 Controller Hardware Setup 28

2.3.1 Eddy-Current Position Transducers 28

2.3.2 Signal Conditioning 30

2.3.3 Power Amplifiers 31

2.3.4 Data Acquisition System - dSPACE 32

2.4 Control System Setup 33

2.5 Summary 35

3 System Modelling and Model Reduction Technique 44

3.1 Flexible Rotor Modelling 44

3.2 FEM Model Accuracy 48

3.3 Model Reduction Technique 49

3.4 Model Reduction Comparison 54

3.5 Summary 57

4 Contact Dynamic Analysis and Modelling 70

4.1 Introduction 70

4.2 Classical Contact Model 71

4.2.1 Friction Forces 74

4.2.2 Classical Model Deficiencies 75

4.3 Lagrangian Approach for Forward Whirl 77

4.3.1 Single Contact Dynamics Modelling 78

4.3.2 Single Contact Simulation Results 83

4.3.3 Multiple Contact Dynamics Modelling 85

4.3.4 Multiple Contact Simulation Results 88

4.4 Experimental Verification of the Constrained Lagrangian Modelling Technique 91

4.5 Lagrangian Approach for Backward Whirl 93

4.5.1 Backward Whirl and Rolling Motion Modelling 93

4.5.2 Backward Whirl and Rolling Simulation Results 97

4.6 Summary 100

5 ROLAC Control Algorithm Design **121**

5.1 Passive Local Closed Loop Control 121

5.2 Open Loop Adaptive Control 123

5.3 The Estimation of the Partial Receptance Matrix 125

5.4 Recursive Open Loop Adaptive Control 130

5.5 Simulation Results 133

5.6 Summary 135

6 Real-Time Implementation of ROLAC **142**

6.1 On-Line Recursive Fourier Transform 143

6.2 On-Line Identification of the Partial Receptance Matrix 144

6.3 Implementation of ROLAC 149

6.4 Experimental Verification of ROLAC 150

6.4.1 Vibration Attenuation using ROLAC 150

6.4.2 Preventing Contact using ROLAC 151

6.4.3 Recovering Rotor Position using ROLAC 152

6.5 Summary 154

7 Conclusions and Future Work **175**

7.1 Conclusions 175

7.2 Future Work 180

References **181**

Chapter 1

Introduction

Active Magnetic Bearings (**AMBs**) offer advantages over conventional bearings. Their unique features and the appeal towards high speed machines make them attractive for certain common rotor/bearing applications. Thus, AMBs have been researched significantly since the 1980s, and a number of advance improvements in performance have been achieved. These developments will be discussed in different sections covering the general background, control strategies, system faults and the rotor-retainer bearing contact problem.

1.1 Background on AMB Systems

The use of magnetic forces to levitate a body without contact is an old idea. In 1842, Earnshaw showed that a passive magnetic bearing is unstable [1]. The instability problem in passive magnetic bearings occurs since the natural tendency of the stator is to attract the rotor until they come into contact. This problem led to research work towards active systems. The term "active" implies that stable control action has been incorporated into the system to adjust the electromagnetic forces and maintain the rotor position. Thus, it is extremely important to provide some position feedback control in order to overcome the negative stiffness effect [2].

Electromagnetic poles may be placed in various arrangement around the rotor to form an active bearing and to provide radial force [3]. Each electromagnetic pole is driven by an amplifier. The electromagnetic force axes are generally orientated at 45° to the perpendicular so that forces due to gravity are compensated by the upper two adjoining actuators, increasing the system stability and adding to the load capability of the system. These forces can be conformed to any changes in system conditions with the use of an electronic control scheme [4].

A typical approach is to use decentralized Proportional-Integral-Derivative (**PID**) control. The controller operates on measured signals within the air gap using sensors to determine the control current (hence force) required by the bearing. The fundamental control principle is to stabilize the rotor position at the bearing centre. This requires high resolution sensors and adequate signal processing.

The function of the controller is to receive voltage signals from the calibrated positional sensors and process them. The voltage signals are passed through anti-aliasing filters to remove any high frequency noise that may lead to fictitious low frequency components [5]. The required current to correct the shaft position is compared to the demand, which will produce an error signal that is proportional to the force produced by the magnetic bearing. This force is reduced when the shaft is above the demand position and vice versa.

AMBs are designed to levitate a rotor against gravity. They may also operate as actuators through feedback control force capabilities to attenuate rotor vibration and automatically adapt the rotor dynamics to changes in operating condition. AMB technology offers a wide range of advantages for industrial, medical and scientific applications [6, 7, 8] including:

- The elimination of physical contact between the shaft and the bearing minimises the friction and eliminates the wear inherent in conventional bearings
- Magnetic bearings are capable of precise control of rotor position, attenuation of vibration and control of flexible structural resonance modes using advanced control
- Magnetic bearings offer advanced monitoring and diagnostic capabilities. This allows for early detection of emerging faults, organisation of maintenance and optimisation of performance
- Magnetic bearings operate at high speeds with low power consumption in applications such as spindles

- Magnetic bearings offer a dry and clean environment eliminating the need for lubrication and chances of contamination
- They offer high reliability with long life expectancy due to no wear during run up, run down or when in full operation
- Magnetic bearings provides high reliability and long service life that is critical in applications such as vacuum pumps; and natural gas pipeline compression equipment
- Magnetic bearings are able to operate under extreme conditions such as high or low pressures (vacuum pumps) and a wide range of temperatures

Active magnetic bearings have limitations that arise from physical constraints, design and material. Some of these limitations are summarized below:

- Magnetic bearings have lower load capacity (maximum load per unit of area) than conventional bearings
- Magnetic bearings require power to control the system, and to drive sensors and electromagnets increasing system complexity and initial cost
- Losses in magnetic bearings are mainly due to eddy currents that limit the rotational frequency of rotors (heating up, driving power). The eddy-current losses can be reduced by dividing the iron core in to insulated sheets (laminations)
- Magnetic bearings with high precision control of the rotor position require adequate signal processing and high resolution sensing

AMB technology is a novel mechatronic application that combines and integrates mechanics, electronics and computer science [9]. It is widely used in various engineering fields such as aerospace applications [10]. The National Aeronautics and Space Administration (NASA) and the Air Force Research Laboratory (AFRL) have collaborated to develop flywheel energy storage for integrated power and attitude control systems (IPACS) in mid-large satellite applications [11]. It is important to minimise the losses in a flywheel to achieve efficient energy storage. Recently, Sivrioglu *et al.* [12] have reported a non-linear control technique that produces a zero bias current (switched off) in one of the magnets while the opposite side is switched on to generate the attractive force. The switching algorithm will continue until the rotor is stabilised. This on-off approach lowers the powers consumption in the flywheel when compared to PID control. Another development of magnetic bearing applications is for use in gas turbine engines [13].

AMB applications in machine tools include electro-spindles, for milling and grinding. A recent study shows substantial benefits for high-speed machining due to increased metal cutting productivity [14]. Light industry applications of AMBs having a rotor of less than 50kg are in X-ray tubes, liquid helium pumps and turbomolecular vacuum pumps [15, 16]. Heavy industry applications are related to turbomachines and electrical machines including compressors and turbo expanders [16]. They are also used in the biomedical industry for blood pumps, neurosurgery catheter systems [17] and artificial heart pumps [18]. Magnetic bearings have also been usefully applied to non-rotating systems [19], and applications requiring precision motion control and wind tunnel model levitation.

In rotating machinery applications, rotors maybe classified into two main groups: rigid and flexible. To some extent, all rotors are flexible, they are referred to as flexible or rigid according to whether the first critical speed occurs within the operational speed range. Flexibility may cause a problem in control design if the flexural mode node coincides with sensor positions. The vibration control problem in a rigid rotor is more straightforward and typically controlled with PID feedback. The development of control strategies for a flexible rotor/active bearing system is crucial to extend the range of future AMB applications.

1.2 Control Issues in AMB Systems

Plenty of work has been reported in the literature examining the vibration control of flexible rotors [12, 20, 21, 22]. Comparison between classical PID control and μ-synthesis, Linear Quadratic Regulator (**LQR**)and fuzzy logic control is demonstrated in [23, 24]. Modern control schemes for vibration attenuation have been developed in the field of magnetic bearing research as a powerful tool to achieve the desired performance. Fuzzy logic control has been considered as a potential approach to design robust controllers [25]. Experimental and simulation implementation of a fuzzy logic based controller was used to investigate robustness performance against harmonic disturbances and modelling errors [26]. A fuzzy logic controller was designed for turbomolecular pumps to optimise the bias current according to operational conditions that is a function of the desired bearing stiffness and the rotor vibration amplitudes [27].

When vibrations are non synchronous or when a rotor is subjected to wide-band forcing frequencies, a closed loop feedback controller is preferable. H_∞ schemes are well documented in the literature [28, 29, 30, 31]. It is well known that the ability of H_∞ optimisation to minimise the effect of modelling errors and plant variations provides robustness. The main target is to minimise the least upper bound value of the frequency response of a closed-loop transfer function. The least upper bound value is defined for a stable system as the highest peak amplitude of a Bode plot of that system. H_∞ optimisation control based on the use of measured harmonic components of rotor vibration has been designed and implemented experimentally [32]. The control forces were evaluated to attenuate

transient and steady-state vibration response due to step changes in disturbances with attention to practical limitations such as delays and measurements errors.

Synchronous vibration control has been investigated using closed-loop feedback strategies. This development increases the system ability to respond to changes in synchronous vibration components caused by sudden changes in unbalance and transient vibration [21, 33]. Moreover, adaptive controllers designed by using the impulse response-based model predictive control (IMPC) and generalized predictive control (GPC), have been evaluated experimentally [34]. These methods are effective in attenuating the periodic disturbances due to constant and variable rotational speed. Gain scheduled adaptive control approaches are used for the reduction of active magnetic bearing speed-synchronous current over wide range of operating speeds for a high speed spindle application [35].

Significant progress has already been made towards closed-loop control of synchronous vibration of flexible rotors. However, closed-loop strategies are complex and may exhibit stability problems [20]. There are various well understood strategies for controlling magnetic bearings systems. The Open Loop Adaptive Control (**OLAC**) technique uses a least-squares algorithm to determine the optimal control forces in frequency domain to minimise the amplitude of the measured synchronous components of flexible rotor vibration [36, 37]. This technique does not require any prior knowledge of the system characteristics. The crucial element in using an open-loop strategy is its ability to avoid system instability and performance problems, which are associated with all closed-loop strategies [38].

The OLAC strategy uses a magnetic bearing as an actuator and updates the

open loop control signal when any change in the measured rotor displacements is detected. Also a wide range of statistical information can be made available for system monitoring and fault detection. Its ability to identify the system status on-line was the key issue for fault detection in the control of a flexible rotor supported with magnetic bearings using stochastic approach developed by Sahinkaya *et al.* [39]. Various fault detection algorithms have been considered in the literature. A model-based identification in the frequency domain of multiple faults is presented in [40], which was tested in numerical simulations and experimentally. It is based on identifying faults with the use of a residual map to localize faults effectively. Vyas and Satishkumar [41] present an identification method by means of neural network approach for five primary faults and their combinations. Theoretical and experimental results illustrate the effectiveness of the method.

A synchronous vibration controller applied in an open-loop sense has been developed considering the case where a rotor/retainer bearing contact is induced with transient or temporary abnormal faults when full control is still available [42]. The author introduces a control strategy that uses recursive open-loop adaptive control [43]. The controller was tested numerically and experimentally on a flexible rotor supported by magnetic bearings. The technique is able to restore the rotor position without violating stability. The rotor/retainer bearing contact dynamic behaviour needs to be accurately and reliably modelled for the development of controllers to recover rotor position.

The described control techniques deal with active magnetic bearings under normal operation. They are concerned mainly with synchronous or transient vibration

attenuation arising from external disturbances. Due to the limited force capacity of AMBs, they incorporate retainer bearings to protect rotor/stator laminations from faults or large rotor displacements. Rotor contact interaction with retainer bearing changes the dynamics of a rotor/magnetic bearing system. Accurate prediction of retainer bearing dynamics under contact conditions is crucial to enable design of controllers to handle the rotor dynamics during and after contact [44]. A controller design that does not take these changes into consideration may result in undesirable performance or a stability problem. Therefore, further research on the problem of rotor contact to recover the system to minimise normal contact force and/or duration is essential for the future applications of magnetic bearings. This is undertaken by the author in the present study.

1.3 Faults in AMB systems

Important issues in the design of magnetic bearings are cost and reliability. The initial cost of a magnetic bearing system is high, thus it is essential to consider the cost of maintenance. The principal objective for fault-tolerant control is to allow the continued safe running of the rotor during the occurrence of a fault so that it can subsequently be run down safely for maintenance.

There are many different techniques to identify magnetic bearing faults. A technique based on an extension of open-loop adaptive control, which utilizes the variance of the measured system response and identified parameters was developed by Sahinkaya *et al.* [39]. Techniques to identify faults by fitting the measured vibration data to a model defined under various malfunction conditions and by pattern recognition methods using neural network have been reported [41, 45].

The ability of a magnetic bearing to be fault tolerant is critical in its development for many future applications. Thus magnetic bearings have been introduced into the industrial world as safe and reliable devices which are dependent upon the system ability to attenuate any excessive vibrations resulting from faults. The safety and reliability issues are discussed in detail by Schweitzer [46]. Potential malfunctions can be classified into main groups that are external or internal to the magnetic bearing system.

1.3.1 System Internal Malfunctions

Sensors Failures: In an active magnetic bearing system, sensors provide the measurements of the rotor position relative to the bearing centre and consequently produce the correct control force in phase and magnitude. Sensor faults may rise from dislocation, signal distortion due to physical damage of the transmission line. Sensor faults tend to deteriorate the system performance and may cause rotor to come into contact with its retainer bearing or cause instability problems.

Bearing Coil and Power Amplifier Failures: Any one of the coil currents affects the flux in the air gap. Partial loss of a coil may arise from a short circuit or unexpected fault, which reduces the number of windings in operation leading to less effective control force. One or more coil failures will result in the loss of one or more control force axes and consequently the contact problem will occur. High speed contact events due to total power loss could be catastrophic due to rotor bounces and uncontrolled vibration. Power amplifier failure causes the same problem may occur as a results of physical damage, transmission line signal loss or over loading.

1.3.2 System External Malfunctions

The following faults are categorized as external since the fault itself or its effects can be represented by an external disturbance acting on the system. The disturbance force always has transient components together with steady-state components.

Base Motion: With further research and development, magnetic bearings may be considered for use in motion environments. This would open new application areas, such as jet engines, land transportation (i.e trains and vehicles), sea transportation (i.e submarines and ships), air transportation and space stations. In these cases a rotor bearing system may be subjected to sudden external excitation and shutting down the system is out of consideration. In these applications, the base motion will have a great effect on the dynamic behaviour. In some cases, the sudden increase of rotor vibrations, which may cause contact, is transient or temporary.

Rotor Mass Unbalance: Mass unbalance occurs when the geometric centre does not coincide with the mass centre of a rotor. It is an inevitable fault in rotor machinery i.e mass loss. Its effect is to cause vibration at the rotational speed (synchronous vibration). Higher harmonics of rotational speed may also be excited. Rotor vibration can be detected by monitoring the rotor displacement magnitude and phase. The rotor whirl orbits are normally elliptical. In many cases, external and internal faults are the main cause of rotor/bearing contact.

1.4 Contact Dynamic Modelling

Retainer bearings perform many tasks such as the protection of sensors and lamination under abnormal situations, together with extra support for the rotor if large displacements occur. These are typically rolling element bearing or simple bushes having smaller clearance than the magnetic bearing. Under certain circumstances, a rotor may come into contact with retainer bearings initiating non-linear behaviour. When contact happens, impact forces and sudden increases in temperature are experienced, which are responsible for the damage of retainer bearings [47]. It may require the system to be shut down in order to prevent further damage.

The life expectancy of retainer bearings following contact is very short, measured in hours or minutes [48]. A study undertaken by Sun [49] presents an estimated retainer bearing life based on Hertzian contact dynamic loads between bearing ball and races during touchdown. The dynamic behaviour of a rolling element bearing following rotor impact in active magnetic bearings is examined in [44]. The influence of bearing parameters are analyzed with the implications of energy dissipation in the bearing. A development study undertaken by SKF/Revolve to design a long life retainer bearing for turbomachinery and high-speed motors is described by Reitsma [48]. Increasing the life expectancy of retainer bearings requires knowledge of the interaction between the rotor and the retainer bearing. One of the parameters in bearing design is the gap between the rotor and the inner race of the retainer bearing, which influences the non-linear rotor/magnetic bearing dynamic behaviour and efficiency under contact conditions [50].

Research work related to rotor-stator contact when the magnetic bearings are still functional is limited. Contact may occur due to a sudden change in system status or due to a transient or temporary disturbance forces [51, 52], while the magnetic bearings are in perfectly good condition. Some controllers may worsen the dynamic response of the rotor if interaction is not considered in their design [53]. However, it may be possible to recover the system with proper control action, which would help in reducing the contact forces and extending the life expectancy of the retainer bearings [22, 54]. That would open new opportunities for various future applications such as in medical instruments i.e. blood pumps, and land, sea and air transports, where system shut-down is not an option. This is one of the problems tackled in chapter 4. The safety and reliability issues are critical for these applications, which has been assessed by Schweitzer [46].

Plenty of work has been reported in the literature examining the contact dynamics associated with rotor drop. The sub-harmonic transient response and non-linearities have been investigated by Ehrich [55]. The rotor response under partial rub phenomena is analyzed theoretically and shows the existence of steady-state subharmonics of the order 1/2, 1/3, 1/4 etc [56]. Childs also investigated subharmonic response of a Jeffcott rotor, and studied theoretically the instability of rotor contacting with its housing [57]. The synchronous whirl behaviour was studied using the receptance technique by Johnson [58]. Most of the work has concentrated on understanding the contact dynamics of the rotor to identify the dominant components that affect the rotor response. A drop test of a one ton compressor rotor when magnetic bearings fail was reported by Schmied and Pradetto [59]. Studies examining the influence of bearing clearance on flex-

ible rotor dynamic behaviour have been conducted to compare and verify the simulation results presenting various system responses [60, 61, 62].

Kirk *et al.* [63] reported an explanatory study describing classical modelling techniques to predict the dynamic of the rotor and the instantaneous forces acting on the retainer bearing. In classical contact modelling, the contact forces are expressed as a function of the rotor penetration depth into the bearing inner surface at the contact point [50, 64]. In modelling of the contact forces, the stiffness coefficient is also related to the rotor penetration depth by an exponential function [63]. The spring-damping contact modelling technique suffers from a few drawbacks [65, 66, 67] as discussed in details in section 4.2.2. Fumagalli and Schweitzer [65] used a non-linear stiffness and damping model of rotor-stator contact and made comparison between predicted and measured contact forces and rotor dynamic response.

Wang and Noah [68] analyzed the behaviour of a rigid rotor in clearance bushes using the same bearing model. A full scale experimental setup was designed to enhance the understanding of dynamic of the rotor drop and evaluate various retainer bearing configurations for turbomachinery applications supported by AMBs [69]. More practical studies concerning calculation of the transient response and contact forces on the radial retainer bearing are represented in the literature [70, 71, 72]. A theoretical formulation was proposed and solved numerically to examine the transient response of the flexible rotor when the active magnetic bearing shuts down initiating the rotor drop onto the retainer bearing. The backward whirl of the rotor has been predicted and also the contact forces

have been computed [73].

Recently, a new approach to control a rotor when in contact with the retainer bearing is introduced [74, 75]. The control forces are applied on the rotor in indirect way using the retainer bearings. They are mounted on two electromagnetic actuators in a 45°. The contact forces were measured in the normal and tangential directions experimentally [76]. This work was extended with an objective to minimise the contact forces using piezo actuators controlled with feedback linearization and sliding mode control [75].

Contact dynamic behaviour is a complex phenomenon and involves many physical elements [77]. One dimension of complexity is modelling the friction forces, which depends on contact geometry, displacement relative velocity, level of lubrication, bulk and surface material properties, and temperature [63, 78]. Coulomb developed the classic model friction force being proportional to the normal load where its magnitude is independent of velocity and contact area; the model is known as Coulomb friction. The literature is rich with various studies on different modelling representation of friction forces [78].

The classical estimation of the friction force known as Coulomb friction is expressed as the force exerted in the direction opposite the object's motion. The model is given in the figure 1.1(a). The friction force caused by the viscosity of lubricants is combined with the Coulomb friction gave the model depicted in the figure 1.1(b). When static friction is added, another friction model appears that is the static plus Coulomb plus viscous friction model. This model is given in the figure 1.1(c). It was observed that for low velocities, the friction force is de-

creasing continuously with increasing velocities and not in a discontinuous matter as described above. This phenomenon of a decreasing friction at low-increasing velocities is called the Stribeck friction. This model is given in the figure 1.1(d).

Although coulomb model is a simple representation of friction, it is adequate for the analysis of contact dynamic in rotor dynamic applications. For this reason, the author considered the Coulomb friction model in this thesis.

1.5 Project Aims and Objectives

The aims and objectives of the research project are categorised into three main groups:

- To investigate the contact dynamic behaviour of a flexible rotor/bearing system. The aim is to model the complicated dynamic behaviour of a rotor when it is in contact with the retainer bearings using a computationally efficient technique. The objective is to eliminate the computational inefficiency associated with non-linear stiffness and damping elements used in the conventional techniques.

- To enhance the computational efficiency using model reduction techniques. The aim is to introduce a finite element rotor model involving only the required rectilinear displacements in sensor and controller nodal planes. The reduced order model is required to predict the natural frequencies of interest and system responses to step changes in unbalance with an acceptable level of accuracy.

- To use the computationally efficient reduced model to develop controllers to prevent contact or recover rotor position if contact occurs. The new controller will be designed to act quickly in case of sudden change of synchronous force and also to attenuate vibration due to unknown out of balance forces. Also, the developed controller will be applied in real-time using flexible rotor magnetic bearing system.

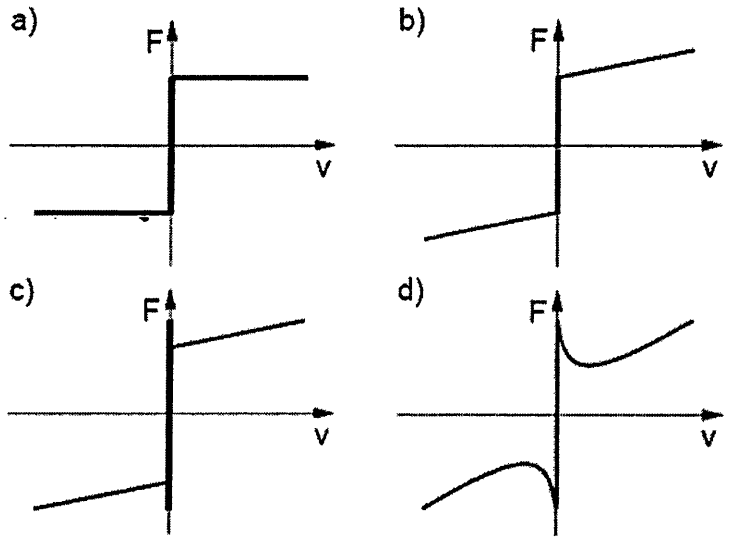

Figure 1.1: The friction force is given by a static function except possibly for zero velocity; a) shows Coulomb friction b) Coulomb plus viscous friction c) Stiction plus Coulomb and viscous friction d) Coulomb plus viscous plus Stribeck friction [78].

Chapter 2

Experimental Flexible Rotor/Magnetic Bearing Setup

2.1 Design Requirements and System Outline

An active electromagnetic bearing is a mechatronic system. The basic elements of the system are sensors to measure displacements from a reference position, a digital processor to derive a control signal, a power amplifier to generate suitable control current, an electro-magnet to produce the appropriate control force, and a rotor to suspend. The existing rotor/active magnetic bearing experimental facility used in this study was designed by Rutland and Keogh [79, 80, 81].

The system comprises of a uniform flexible steel shaft of length 2 m and radius

0.025 m. Four 10 kg rigid discs of radii 0.120 m are added to the rotor to provide more inertia giving a total mass of 100 kg. The flexible rotor is capable of running at a speed range up to 100 Hz covering the first two flexural critical speeds. The rotor is horizontally mounted on two radial magnetic bearings, each with a maximum dynamic force capacity of 1700 N [81]. Each has eight poles (four coil pairs) placed in two orthogonal opposing pairs at $\pm 45°$ with the vertical line to provide maximum static load. The magnetic bearings have 1.2 mm radial clearance and are protected by rolling element retainer bearings with radial clearance of 0.75 mm clearance. Two bronze retainer bearings are placed at the ends of the rotor with clearance of 0.90 mm.

The shaft is connected through a universal coupling to an AC motor that runs at speeds up to 6000 rev/min (100 Hz). The motor is controlled by a separate controller, with 16-bit microprocessor and configurable I/O panel, with built-in fault alarm. A schematic lay out of the magnetic bearing/flexible rotor system is shown in figure 2.1

One of the most important aspects for designing flexible rotor systems is the critical speeds. The system requires sufficient damping to pass through these speeds. Disks were placed such that the second flexural frequency is well below the maximum designed running speed. The rotor design specifications are given in Table 2.1.

Table 2.1: Flexible rotor design specification

Rotor Length	2m
Rotor Shaft Diameter	0.05m
Rotor Total Mass	100kg
Disk Mass	10kg
Maximum Running Frequency	628rad/s (100Hz)

2.2 Magnetic Bearing Modelling

A photograph of the experimental rig is shown in figure 2.2. A photograph and schematic layout of the AMB coils, and the laminated stack are shown in figures 2.3(a) and 2.3(b), respectively.

An active magnetic bearing design is based on a common assumption known as "zero leakage". For a high permeability magnetic structure with small air gap, all flux is confined to the iron and the gap volume. In practice, the maximum coil force is limited by saturation and hysteresis effects. Therefore, the maximum control force is limited for magnet core flux saturation and the power amplifier capabilities. Another significant factor limiting the maximum coil force is the inductance effects of electromagnets. The design specification of each of the experimental active magnetic bearing given in Table 2.2 is specified according to the procedure described by Rutland and Keogh [79] and from where the following analysis is derived.

The coil cut-off frequency decreases due to inductance. Using the magnetic bearing design specification data in Table 2.2, the cutoff frequency can be calculated

Table 2.2: Design specification of each magnetic bearing

Maximum Control Force	1700 N
Static Weight to be levitated	500 N
Nominal Air Gap	1.2mm
Pole Face Area	1399mm^2
Bias Current	-4.43A
Static Load Current	1.14A
Power Amplifier Peak Current	10A
Coil Resistance	0.365 Ω
Coil Inductance	0.0732 H
Number of Turns per Pole	158

as follows:

$$\omega_{coil} = \frac{R_c}{L} = \frac{0.365}{0.0732} = 5\ rad/s \tag{2.1}$$

However, the power amplifiers are current controlled and can compensate for the coil frequency response roll-off to a frequency well above ω_{coil}. This prevents the need for higher voltage input to maintain the current at 10A up to the maximum running frequency of 100 Hz before the amplifier voltage input enters saturation. It is important to mention that the controller produces a voltage input to the amplifier, which is then converted to current through the coils. The flux-current relationship in the coils is:

$$B = \frac{\mu_o N I}{(l_{gap} + l_{iron}/\mu_r)} \tag{2.2}$$

A simple theoretical analysis provides the attraction force generated by a single magnet coil with a double pole, as shown in figure 2.4, as:

$$\begin{aligned} F &= \frac{1}{2} B H_{gap} A_e = \frac{B^2}{2\mu_o} A_e \\ F &= \frac{\mu_o N^2 I^2 A_e}{2\left(l_{gap} + {}^{l_{iron}}/_{\mu_r}\right)^2} \end{aligned} \tag{2.3}$$

The magnetic bearing coils are constructed with dual opposing pairs of poles in such a way that they can be considered as two "horse-shoe" electromagnets. The bearing configuration is operated in the so called differential driving mode, where a constant bias current (I_b) is supplied to the coils of both electromagnets. A control force is generated by adding a control current (I_c) on the bias current in one electromagnet and subtracting it from the opposite side. The current (I_s) is the constant current necessary to levitate against the rotor weight. Since in the iron, $\mu_r \gg 1$, i.e $({}^{l_{iron}}/_{\mu_r} \ll l_{gap})$, the magnetization of the iron $({}^{l_{iron}}/_{\mu_r})$ is often neglected. Rotor positive displacement is defined when the air gap between the upper coils and rotor decreases as shown in figure 2.4. The currents in the coils expressed in differential mode are as follows:

$$I = \begin{cases} I_s + I_b + I_c, & \text{for upper coils} \\ I_b - I_c, & \text{for lower coils} \end{cases} \tag{2.4}$$

The force relationship for the dual opposing poles can be written as:

$$F = \mu_o N^2 A_e \times \left\{ \frac{(I_s + I_b + I_c)^2}{(l_{gap} - x)^2} - \frac{(I_b - I_c)^2}{(l_{gap} + x)^2} \right\} \tag{2.5}$$

In the case of a radial bearing, the forces of both magnetic poles affect the rotor with half angle between double pole faces (β). In the case of the experimental radial bearing with four double pole pairs as shown in figure 2.3(a), β is 22.5°. Considering this angle we obtain:

$$F = \mu_o N^2 A_e \cos\beta \times \left\{ \frac{(I_s + I_b + I_c)^2}{(l_{gap} - x)^2} - \frac{(I_b - I_c)^2}{(l_{gap} + x)^2} \right\} \tag{2.6}$$

Electro-magnetic forces depend in a non-linear manner on the currents flowing in the electromagnet coils and on the distance between the rotor and the stator poles. Equation (2.6) is linearized in the vicinity of the operating point, defined at $(x, I_c) = (0, 0)$. Using the small perturbation technique, the linearized force equation can be written as follows:

$$\begin{aligned} F &= \left.\frac{\partial F}{\partial x}\right|_{\substack{x=0 \\ I_c=0}} x + \left.\frac{\partial F}{\partial I_c}\right|_{\substack{x=0 \\ I_c=0}} I_c \\ &= K_s x + K_i I_c \end{aligned} \tag{2.7}$$

Obviously, the accuracy of equation (2.7) decreases as the distance from the operating point increases causing some non-linearity. The force is differentiated with respect to the displacement of the rotor in order to obtain the negative stiffness of the bearing (K_s), and differentiated with respect to the control voltage in order to obtain the current gain of the bearings (K_i), which are represented as

$$K_s = \frac{2\mu_o A_e N^2}{l_{gap}^3} \cos\beta \, [(I_s + I_b)^2 + I_b^2] \tag{2.8}$$

and

$$K_i = \frac{2\mu_o A_e N^2}{l_{gap}^2} \cos\beta \, [I_s + 2I_b] \tag{2.9}$$

Using the values from Table 2.2 and substitutes in equations (2.8) and (2.9), the calculated theoretical values give 563 N/A for the current gain and 2377 N/mm for the negative stiffness coefficient.

The K_s and K_i values were determined experimentally by positioning a stub rotor shaft at the centre of the nominal air gap with four strain gauges attached to the rotor mounts. The negative stiffness of the bearing was determined by applying appropriate static and bias currents to a single coil pair and measuring the rate of change in force with the displacement. A least-squares first order polynomial fit over the range of ±0.5 mm resulted in K_s=1944 N/mm and K_s=2156 N/mm for MB1 and MB2, respectively, as shown in figures 2.5(a) and 2.5(b) given by Rutland and Keogh [80]. The current gain of the bearing was measured with the rate of change in control current with a least-squares first order polynomial fit over the range of ±2 A gives K_i=544 N/A and K_i=539 N/A for MB1 and

MB2, respectively, as shown in figures 2.5(c) and 2.5(d) given by Rutland and Keogh [80].

2.3 Controller Hardware Setup

Due to the inherent instability of active magnetic bearings, they have to incorporate closed loop controllers incorporating position transducers, data acquisition, signal processing and power amplifiers.

2.3.1 Eddy-Current Position Transducers

There are three types of non-contact displacement transducers commonly used in rotating machinery; capacitance, inductance and eddy current types. The common practice is to use the eddy current sensors for magnetic levitation. These are based on the eddy current induced in a conductive material of the rotor as a result of the magnetic field of the active coil. The eddy current induces an opposite magnetic field and reduces the inductance in the active coil. When the distance between the rotor and the transducer probe changes, the impedance of the coil changes accordingly. Eddy current sensors have an excellent frequency response with extremely small phase shift, which is important for stable rotor levitation. The sensor output is usually linearized. A photograph of the four pairs of eddy current transducers used in the experimental setup are shown in figure 2.6 and specifications are detailed in Table 2.3.

Table 2.3: Specification of eddy current sensors

Body Material	Stainless Steel
Linear Range	± 1% of full scale 0.125 to 2.5 mm
Power Supply	-24 V dc at 30 mA
Frequency Range	DC to 10 kHz
Sensitivity	8 mV/μ m
Probe Temperature Sensitivity	< 5% at 150 °C
Probe Operating Temperature	− 30 to +180 °C

Eddy current position transducers are installed in pairs at each measurement plane at an angle of 90° with respect to each other. The angular orientation of a pair of transducers arranged in four axial planes is at ±45° with the vertical line. The sensors are fixed to the system base such that their location can be varied along the axial direction. Four of them were positioned adjacent and as close as possible (nearly collocated) to both magnetic bearings. The non-collocated sensors do not provide the exact position of the rotor at the bearing locations when the rotor passes through the bending modes or for higher flexural modes. The motion at the bearing locations can have opposite phase to the transducer locations in these cases. Thus, the choice of sensor positions will have an influence on the controller performance and stability. Four other position sensors are placed in pairs at both ends of the rotor close to the end disks as shown in figure 2.6. The effect of placing the sensors at the vibration nodes makes the corresponding modes unobservable. This problem leads to higher gain parameters to control these modes coupled with noise and poor performance problems.

2.3.2 Signal Conditioning

Rotor displacement signals contain unwanted high-frequency noise components and hence, low-pass and anti-aliasing filtering are common signal conditioning operations for magnetic bearings. The aliasing noise problem occurs when the sampling frequency is less than twice the highest frequency (Nyquist frequency) in the voltage signals of the sensors. However, the controller regularly samples the signals thus some of the high-frequency noise may fold over into aliased low frequency signals. Therefore, aliased information received by the controller will result in unnecessary control signals, which may degrade the rotor performance. To eliminate this problem, the position sensor voltage signals are passed through anti-aliasing filters.

Generally, the anti-aliasing filters are low-pass filters that do not pass frequencies above the Analog to Digital (A/D) range. After removing the high frequency components, the voltage position signals are sampled by an A/D converter which converts these signals to a form that can be processed by the digital signal processor. The digital controller output is current demand signal, which is then passed to the Pulse Width Modulation (PWM) generators, which provide PWM wave signals sent to the amplifiers.

2.3.3 Power Amplifiers

Each bearing axis has a pair of amplifiers to provide current to the bearing coils producing a control force to correct the rotor position along that particular axis. The amplifiers are simply high voltage switches that use transistors that are either switched on or off at a high frequency to represent positive or negative voltage values, as commanded by the pulse width modulation wave signal from the controller.

To achieve an increase in the output control current, the positive voltage is switched on for longer period than the negative voltage and vice versa for negative voltage. When a transistor is off, the current through it is zero and when it is on, the voltage across it is small. Thus, the power dissipation is very low reaching efficiencies greater than 80%. Due to high frequency switching oscillation in the coil current the output control signal will contain harmonic distortions and be contaminated with high frequency signal associated with the switching noise. The disadvantage of switching amplifiers is that the current oscillation cause re-magnetization losses in the magnetic bearings. The shorter switching period the weaker current oscillation and so lower losses.

The pulse width modulation uses a square wave whose duty cycle is modulated resulting in the variation of the average value of the waveform as shown in figure 2.7. The pulse width modulation frequency (switching frequency) is 22 kHz. The current limit and the amplifier gain of the voltage input to current output was adjusted to 10 A and 0.5 A/V, respectively. The technical data of the power

Table 2.4: The technical data of power amplifier

Amplifier Type	Voltage controlled current
Input Gain	0.5 A/V
Max Output Current	10 A
Switching Frequency	22 kHz
Signal Band Width	1.4 kHz
Self Check	Over-current, over-and under-voltage

amplifier that used in the experimental setup is given in Table 2.4. The power amplifiers are current controlled and can compensate for the low cut-off frequency of the coils maintaining the control current at 10 A up to the maximum running speed of the rotor 100 Hz before roll-off as explained in section 2.2.

2.3.4 Data Acquisition System - dSPACE

The controller is implemented with a dSPACE hardware/software system, which supports the model-based design using the Matlab®/Simulink® environment. The ControlDesk software of dSPACE is a comprehensive experimental environment that provides a virtual instrument panel. This enables the user to alter experimental parameters and monitor system signals, while the real-time interface (RTI) offers full control over all variables without delay for the controller implementations.

Capturing real-time data to a file is a significant feature of dSPACE. The graphical user interface (GUI) provides an easy way to link a variable to a data acquisition instrument for real-time display and also the data can be saved to a file for

further off-line processing and displaying. A more efficient method to save data to an external file is to use dSPACE/Matlab interface library, which is known as MLIB/MTRACE. It provides real-time data capture capabilities of free-running or triggered mode, recording pre/post-triggered data, adjustable trace capture sampling rate and ability to transfer the captured data to matlab workspace. In addition, MLIB/MTRACE functions are suited to modify parameters online and to send sequences of test data to real-time applications.

2.4 Control System Setup

A schematic diagram of control setup used in experiment is shown in figure 2.8. A digital implementation of a discrete time controller will include an analog to digital converter (ADC) on the input of the controller and a digital to analog converter (DAC) on the output of the controller. The controller will be implemented in Matlab®and Simulink software using a computer. The data exchange between the computer and the dSPACE is achieved with a fibre optic cable. ControlDesk software permits full access to the dSPACE memory in real-time to allow the user to alter the controller and/or experimental test parameters.

After the high frequency noise is removed, the transducers signals are sampled through multi-channel ADC Board, DS2002, to a form that can be processed by the dSPACE digital processor. It has 32 input channels, 16-bit programmable resolution and $\pm$ 5V or $\pm$ 10V programmable input voltage range. The minimum resolution of conversion time is 5.0 μs. Then the dSPACE control processor

evaluates the required control output signals. The DS1005 processor card features a IBM PowerPC 750GX processor running at 1 GHz capable of building the multiprocessor system. With full host access to the global memory, it has 128 MB SDRAM global main memory for host data exchange and application and 16 MB flash memory for user-specific applications and data recording. The DS1005 PPC Board can be programmed using set of Simulink blocks via Real-Time Interface giving access to the entire range of dSPACE I/O Boards. The digital information is passed through a digital filter by the digital signal processor. This produces an output proportional to the amount of current required to correct the rotor position error.

The controller digital signals are converted to analogue signals through, a DS2003 Board. It features 32 parallel converter channels with 14-bit programmable resolution, $\pm$ 5V or $\pm$ 10V programmable output voltage range and resolution of conversion time is 200 ns. This information is sent to PWM generators. The requested control current is used to characterize the PWM wave signal sent to the amplifiers. The control current action must occur well before the next sample. The sampling and control algorithm is processed at a sampling frequency of 4 kHz.

2.5 Summary

The author illustrates the experimental facilities in the Centre for Power Transmission and Motion Control, which was used for the experimental work. The author provides the design specification of the rotor and magnetic bearings. Magnetic bearing modelling and controller hardware components are also explained.

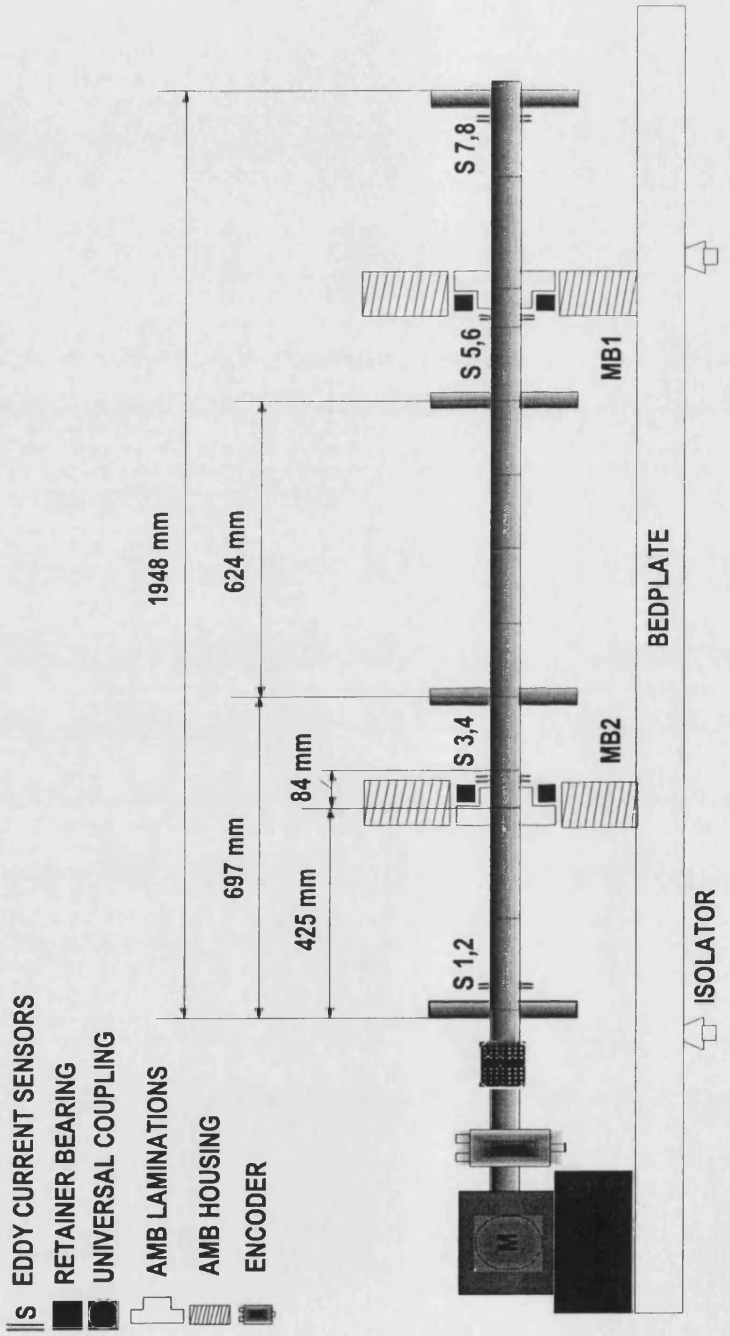

Figure 2.1: A schematic layout of magnetic bearing/flexible rotor system

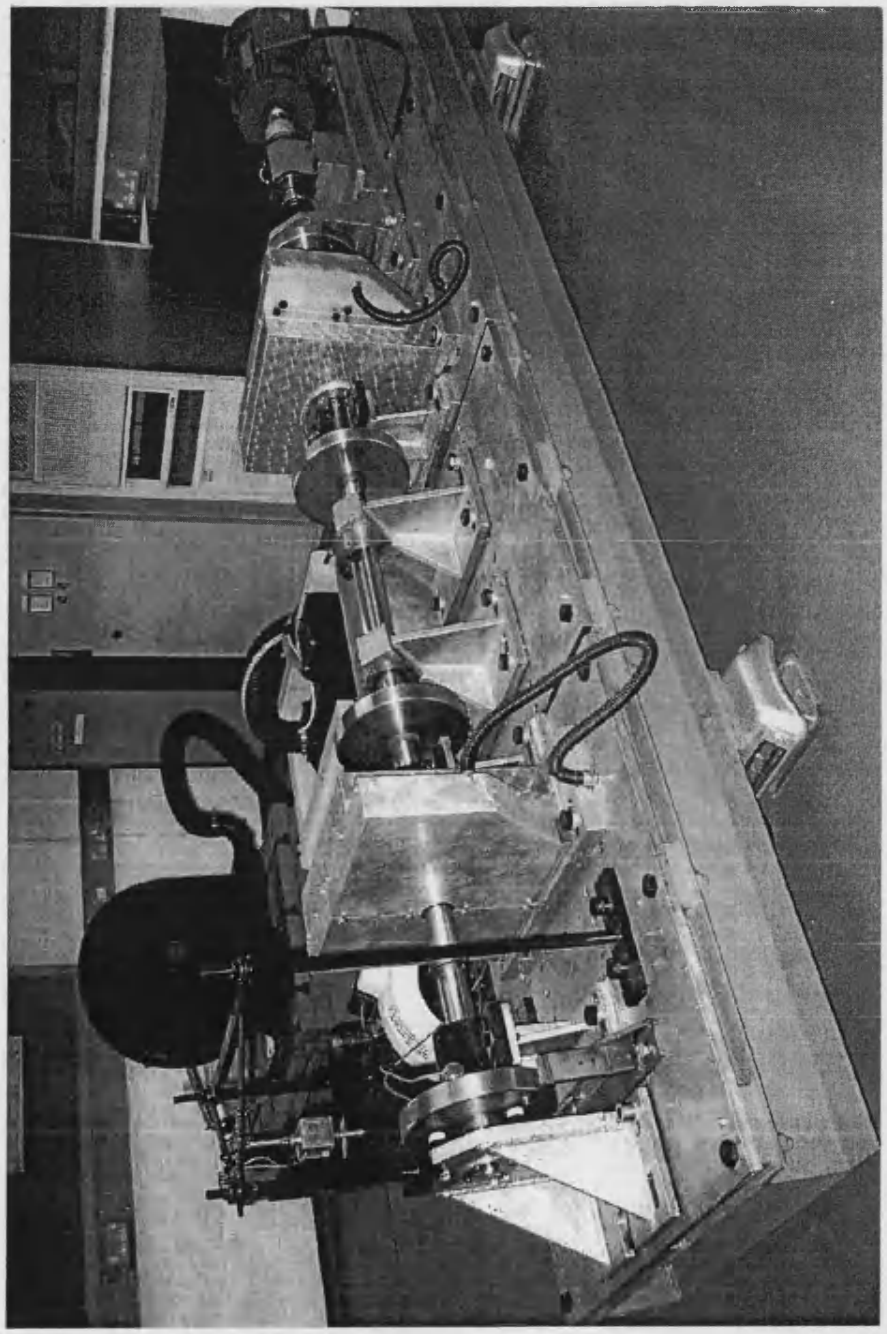

Figure 2.2: Flexible rotor/magnetic bearing system and power amplifiers

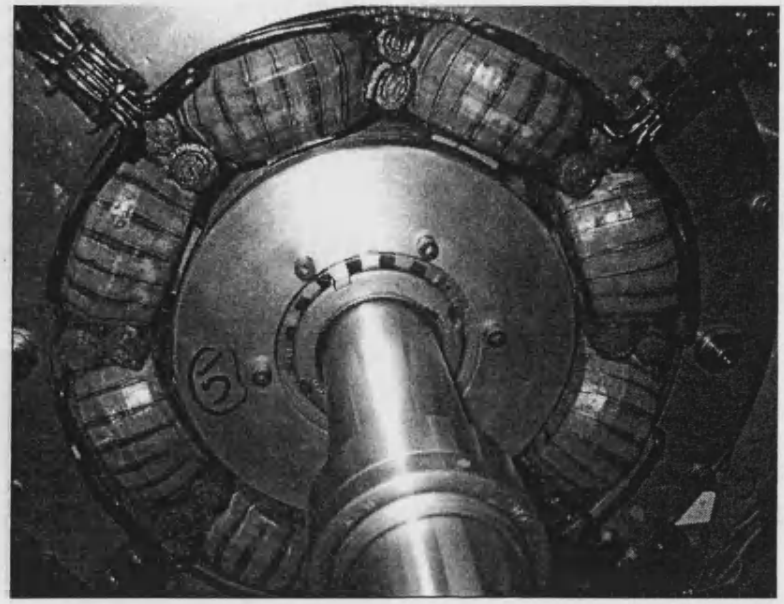

(a) Active magnetic bearing showing the coils and the laminated stack

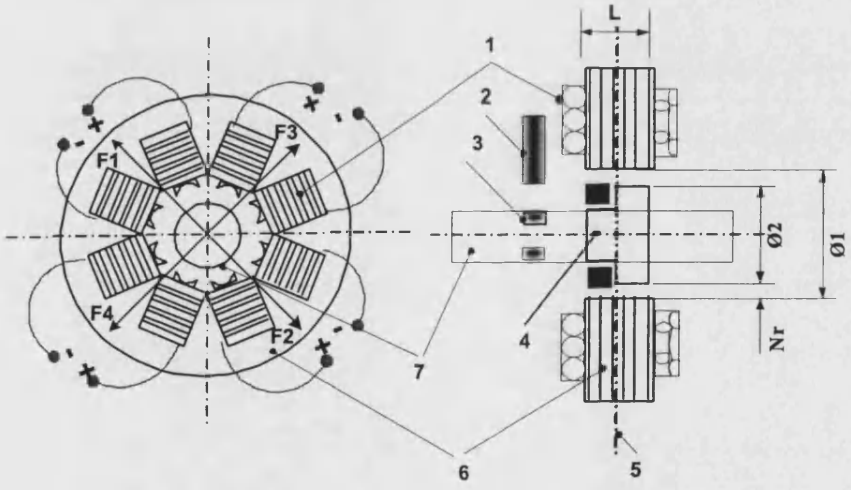

1	Radial Core.	Ø1	Inner Diameter of radial Stator core.
2	Positional Sensor.	Ø2	Outer Diameter of Lamination core.
3	Sensor Measurement.	L	Effective Radial Bearing Length.
4	Radial Lamination Core.	Nr	Nominal Air Gap (Ø2-Ø1)/2.
5	Axial Centre of AMB.	Fi	Radial Active Control Forces (i = 1,2,3,4).
6	Radial Stator Core.		
7	Rotor.		

(b) Schematic layout of an active magnetic bearing

Figure 2.3: The experimental active magnetic bearing

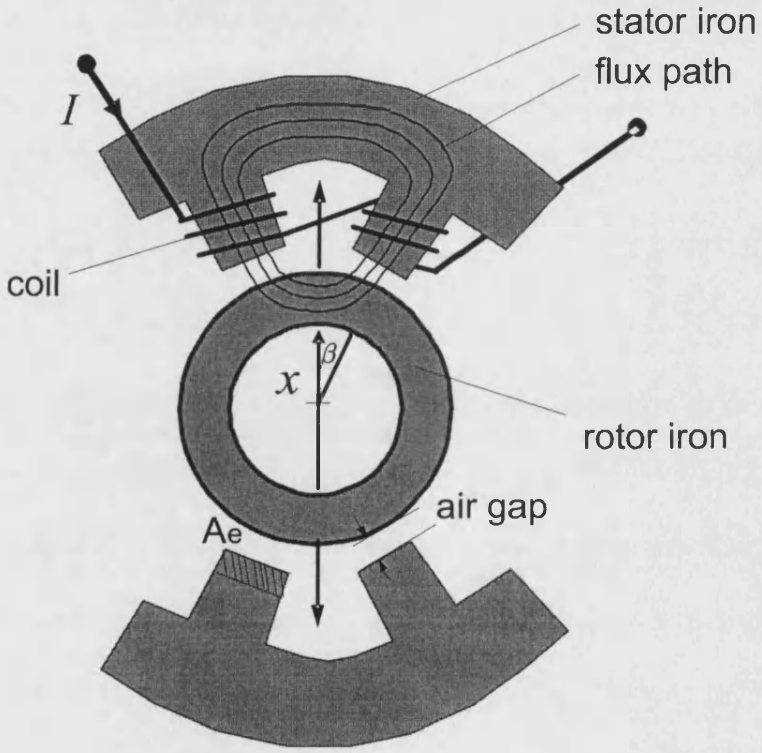

Figure 2.4: A single magnet coil with double pole

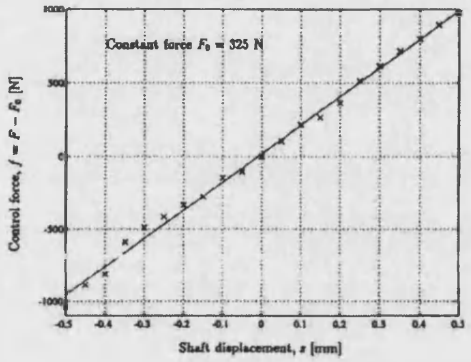

(a) Forces-shaft displacement of MB1, the slope of the straight line is 1944 N/mm

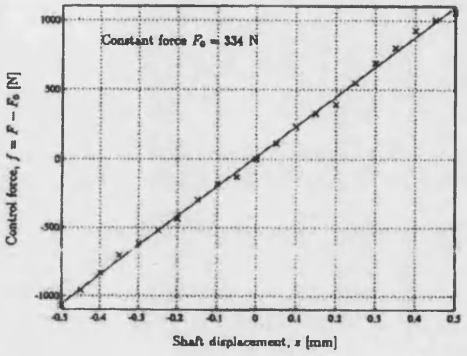

(b) Forces-shaft displacement of MB2, the slope of the straight line is 2156 N/mm

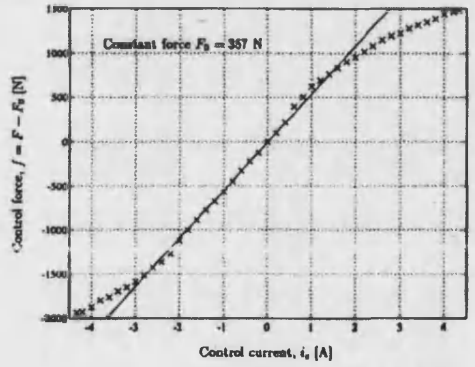

(c) Forces-current of MB1, the slope of the straight line is 544 N/A

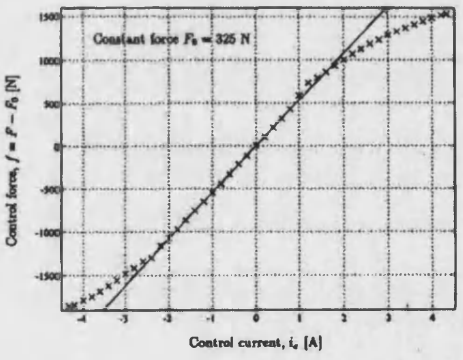

(d) Forces-current of MB2, the slope of the straight line is 539 N/A

Figure 2.5: The experimentally measured magnetic bearing characteristics [80]

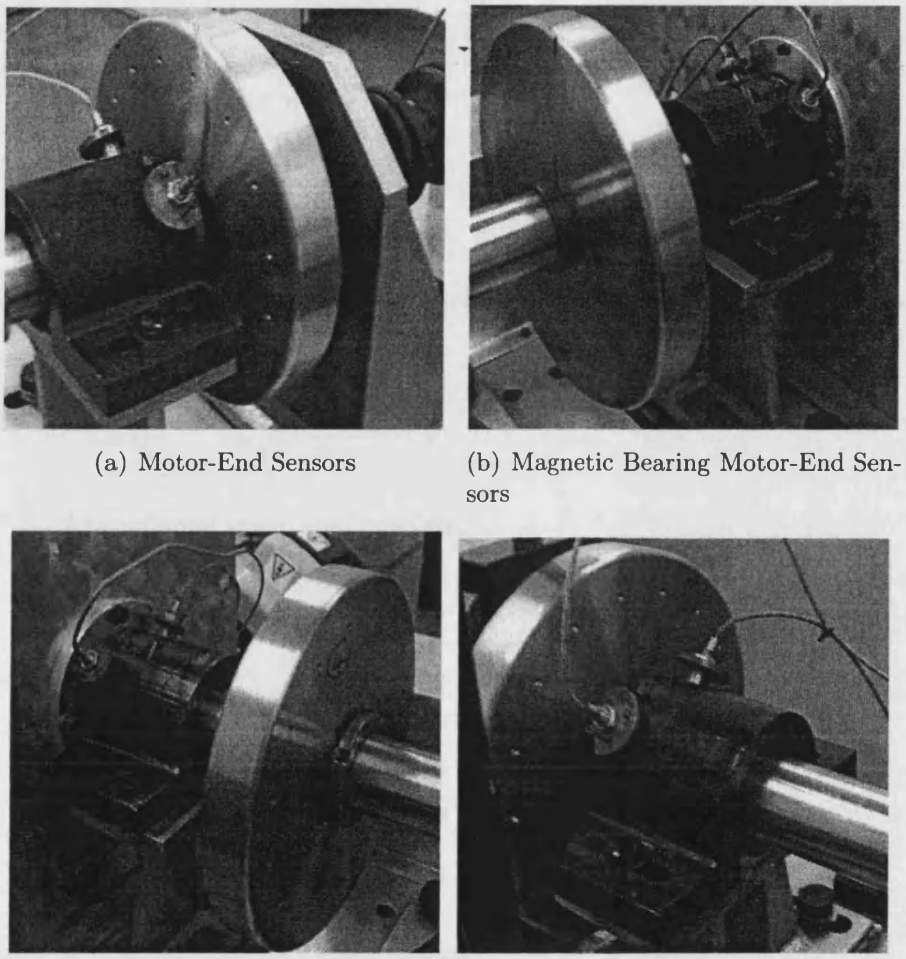

(a) Motor-End Sensors

(b) Magnetic Bearing Motor-End Sensors

(c) Magnetic Bearing Far-End Sensors

(d) Far-End Sensors

Figure 2.6: The eight eddy current displacement sensors arrangements showing their positions at $\pm 45°$ to the vertical

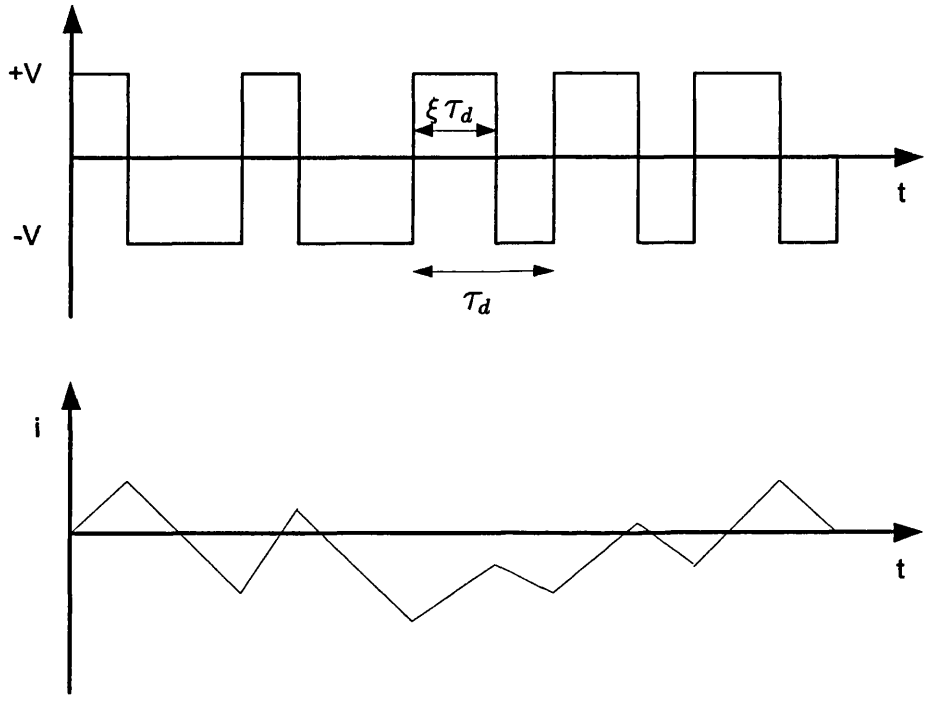

Figure 2.7: Current at pulse width modulation voltage

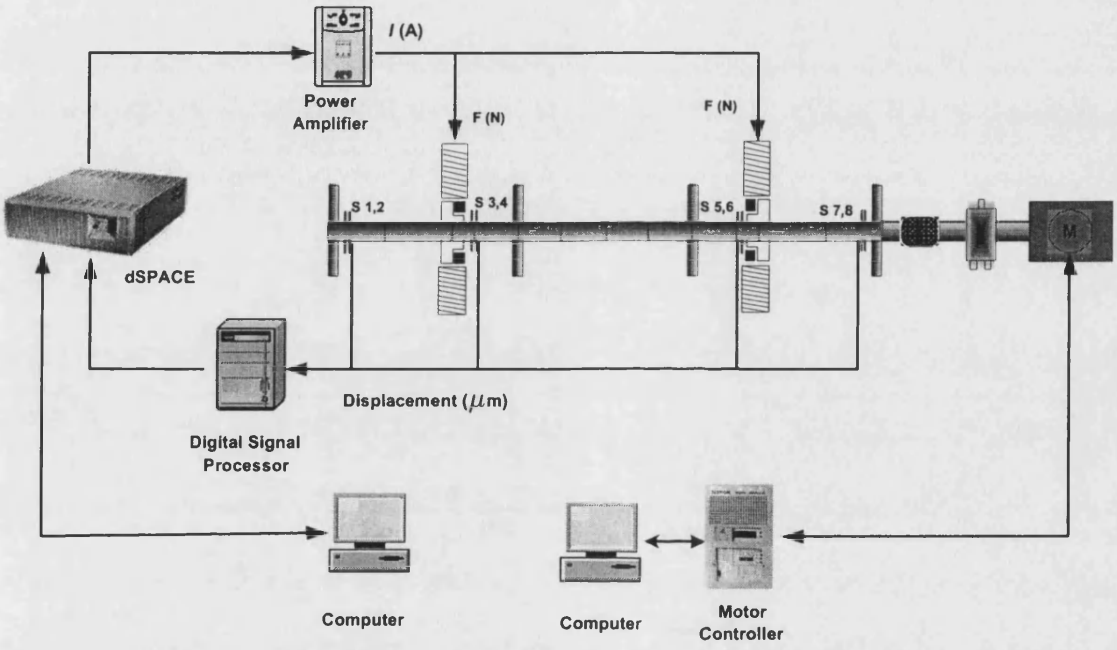

Figure 2.8: Schematic control system of magnetic bearing system

Chapter 3

System Modelling and Model Reduction Technique

3.1 Flexible Rotor Modelling

The rotor can be modelled using the finite element method (FEM) to form mass, stiffness, and damping matrices [82]. Each mass station has four degrees of freedom represented by two orthogonal radial displacements x_i and y_i, and two angular deflections θ_i and ϕ_i corresponding to rotations around the x and y axes respectively. The rotor was divided into twelve sections, which provides a sufficient accuracy for the purpose of this analysis [83] covering the operational speed range up to 3000 rev/min. This gives $N = 13$ nodal planes and 52 degrees of freedom represented by 26 linear and 26 angular deflections. The rotor dynamic

behaviour satisfies the following general equation of motion:

$$\mathbf{M}\ddot{\mathbf{q}} + (\mathbf{C} + \Omega\mathbf{G})\dot{\mathbf{q}} + \mathbf{K}\mathbf{q} = \mathbf{B_d}\mathbf{f_d} + \mathbf{B_u}\mathbf{u} \tag{3.1}$$

where

$$\mathbf{q} = [x_1, \cdots, x_N, y_1, \cdots, y_N, \theta_1, \cdots, \theta_N, \phi_1, \cdots, \phi_N]^T \tag{3.2}$$

and

$$[\mathbf{M}] = \begin{bmatrix} \mathbf{M}_x & 0 & 0 & 0 \\ 0 & \mathbf{M}_y & 0 & 0 \\ 0 & 0 & \mathbf{I_t} & 0 \\ 0 & 0 & 0 & \mathbf{I_t} \end{bmatrix} \quad [\mathbf{K}] = \begin{bmatrix} \mathbf{K}_{xx} & 0 & \mathbf{K}_{x\theta} & 0 \\ 0 & \mathbf{K}_{yy} & 0 & \mathbf{K}_{\phi y} \\ \mathbf{K}_{\theta x} & 0 & \mathbf{K}_{\theta\theta} & 0 \\ 0 & \mathbf{K}_{\phi y} & 0 & \mathbf{K}_{\phi\phi} \end{bmatrix} \tag{3.3}$$

$$[\mathbf{C} + \Omega\mathbf{G}] = \begin{bmatrix} \mathbf{C}_{xx} & 0 & 0 & 0 \\ 0 & \mathbf{C}_{yy} & 0 & 0 \\ 0 & 0 & 0 & -\Omega\mathbf{I_p} \\ 0 & 0 & \Omega\mathbf{I_p} & 0 \end{bmatrix} \tag{3.4}$$

M, **C**, and **K** embody the flexible rotor dynamic characteristics and local proportional and derivative (PD) controller parameters at magnetic bearing nodes,

and the matrix $\mathbf{G}$ describes gyroscopic effects. $\mathbf{f_d}$ is the disturbance vector of synchronous forces and moments, and $\mathbf{B_d}$ is the distribution matrix of these external forces. $\mathbf{u}$ is the four control force vector generated by the two magnetic bearings and $\mathbf{B_u}$ represents the control input coefficient matrix specifying the magnetic bearing locations. The $4N$ second order differential equations in equation (3.1) can be converted to $8N$ first order differential equations in a state space form, which can be integrated to obtain the time response of the system. The state space representation of magnetic bearing system can be formed as follows:

$$\dot{\mathbf{z}} = \mathbf{A}(\Omega)\mathbf{z} + \mathbf{B}_{\bar{\mathbf{d}}} f_d + \mathbf{B}_{\bar{\mathbf{u}}} u, \qquad \mathbf{z} = \left[\mathbf{q}^T, \dot{\mathbf{q}}^T\right]^T \tag{3.5}$$

where

$$\mathbf{A} = \begin{bmatrix} \mathbf{0} & \mathbf{I} \\ -\mathbf{M}^{-1}\mathbf{K} & -\mathbf{M}^{-1}(\Omega\mathbf{G} + \mathbf{C}) \end{bmatrix}, \mathbf{B}_{\bar{\mathbf{d}}} = \begin{bmatrix} \mathbf{0} \\ \mathbf{M}^{-1}\mathbf{B_d} \end{bmatrix}, \mathbf{B}_{\bar{\mathbf{u}}} = \begin{bmatrix} \mathbf{0} \\ \mathbf{M}^{-1}\mathbf{B_u} \end{bmatrix} \tag{3.6}$$

The system frequency response from equation (3.1) is:

$$\mathbf{Q}(j\omega) = [-\mathbf{M}\omega^2 + \mathbf{K} + j\omega(\mathbf{C} + \Omega\mathbf{G})]^{-1} \times [\mathbf{B_d}\mathbf{F_d}(j\omega) + \mathbf{B_u}\mathbf{U}(j\omega)] \tag{3.7}$$

The complex vectors $\mathbf{Q}(j\omega)$, $\mathbf{F_d}(j\omega)$ and $\mathbf{U}(j\omega)$ are the Fourier transform coefficients of $\mathbf{q}(t)$, $\mathbf{f_d}(t)$ and $\mathbf{u}(t)$, respectively. Setting $\omega = \Omega$ and $\mathbf{F_d}(j\omega) = \Omega^2\mathbf{F_o}$ gives the steady state frequency response of the rotor with respect to a given unbalance distribution represented by the complex vector $\mathbf{F_o}$ (kgm), where the elements corresponding to angular displacement are set to zero.

The closed loop mode shapes, natural frequencies and damping values of the rotor-bearing system can be extracted from the eigenvalues and eigenvectors of the system matrix $\mathbf{A}$. The eigenvalues of the system are speed dependent and vary significantly with the bearing stiffness. For a stable system, the real part of all eigenvalues should be negative. The imaginary parts are the damped natural frequencies. Figure 3.1 shows the damped natural frequencies as a function of rotational speed. This is known as a Campbell diagram, and intersection points with the synchronous line gives the critical speeds of the system. However, each modal frequency splits into two with increasing rotational speed due to gyroscopic effects.

The rotor mode shapes shown in figure 3.2 and 3.3 include a PD controller for each magnetic bearing with proportional and derivative gains of 2.7×10^6 N/m and 5000 Ns/m, respectively. The two lowest frequencies correspond to near rigid body modes of the rotor. The conical mode has a frequency of 61 rad/s and the cylindrical mode has a frequency of 106 rad/s. The next two modes correspond to the first and second flexural modes of the rotor at frequencies of 179 rad/s and 429 rad/s, respectively.

3.2 FEM Model Accuracy

The Finite Element Method (FEM) is a numerical technique for obtaining approximate solutions when solving partial differential equations (PDEs) i.e approximating distributed dynamics. It has been successfully applied to many of the problems encountered in engineering disciplines such as solid mechanics (automotive, mechanical, biomedical, electronic), fluid mechanics (aerospace, hydraulics, chemical) and heat transfer (automotive, aerospace, electronic, chemical). The first step of the FEM is to discretize the problem into a number of uniform or non-uniform finite elements. The elements are connected to each other at nodal boundaries.

Errors due to discretization are inevitable because of expressing the mathematical modeling of an infinite degree of freedom system by a finite number of degrees of freedom. However, the accuracy of the FEM can be improved by refining the mesh in accordance with the modelling requirement. In the view of the above, the dynamic equation of motion of the experimental rotor/bearing system are initially obtained by using a large number of nodal planes N= 23 and N= 19.

There are two approaches used in this work to generate the mass matrix. The modelling approach suggested by Nelson and McVaugh [82] results in a non-diagonal mass matrix. A simpler and computational efficient approach is to represent the mass matrix in a diagonal from where the lumped mass and transitional moment of inertia for each element is placed on the diagonal [84, 85].

The accuracy of these models are assessed here in terms of flexural frequencies. The eigenvalues were calculated at different speeds (90, 120 and 145 rad/sec) for both 23 and 19 nodal plane non-diagonal finite element modelling. The 23 nodal planes with non-diagonal mass matrix is selected as a reference model. The number of nodes are then reduced gradually as in Table 3.1 (the numbers are truncated to two decimal places) to find the minimum model size which would predict the eigenvalues within 1.5% error bound in the operating range compared to the reference model in the operating range. First of all, the results presented in Table 3.2 confirm that the 23 nodal non-diagonal model is accurate enough and there is no need to increase the number of nodes. The 13-nodal plane diagonal mass matrix model satisfies the selection criteria as shown in Table 3.3. This model will be called full model.

3.3 Model Reduction Technique

The dynamic equations of motion of the experimental rotor/bearing system are obtained by using a total of $N = 13$ nodal planes resulting in mass, stiffness, damping and gyroscopic matrices of dimension 52×52. This is the minimum size required to achieve an acceptable accuracy for the prediction of the first three critical speeds as discussed in section 3.2. In practice, the control strategy requires only the displacements at measured nodal planes and the planes where the control forces are applied. Thus the four disk positions (two of which corresponds to transducer positions) and two magnetic bearing locations can be selected thereby reducing the mass, stiffness and damping matrices to 24×24. Half of the coor-

dinates, namely the angular displacements, are still redundant because they are neither measured nor controlled. As the number of nodes cannot be reduced further in the finite analysis modelling because of accuracy considerations, a model reduction method, which maintains the required physical coordinates, is needed to minimise the system size.

Using classical techniques, such as Guyan reduction [86], it is possible to reduce the size of the matrices, but at the expense of poor modal accuracy. The main requirement is that the reduced model should be expressed in terms of the physical displacements at the measured locations, and inputs to the reduced model should be the forces applied by the mass unbalance distribution and control forces generated by the magnetic bearings. Qu et al. [87] present a simple technique to reduce the order of constant parameter second order linear system equations. Their approach must be modified to be applicable to flexible rotor magnetic bearing systems, since the matrices are not symmetric and gyroscopic effects imply that the damping term is rotational speed dependent. Before applying Qu's method, the system equations and the variables must be separated into master and slave coordinates and equations. This requires re-ordering of the variables in such a way that the rectilinear displacements of the 6 planes and the corresponding equations are placed at top. If $\mathbf{q_m}$ is the sub-vector of $\mathbf{q}$ that contains the rectilinear displacements at the 6 planes in orthogonal x and y directions, and $\mathbf{q_s}$ contains the remaining rectilinear and angular displacements, re-ordering gives:

$$\begin{bmatrix} \mathbf{M_{mm}} & \mathbf{M_{ms}} \\ \mathbf{M_{sm}} & \mathbf{M_{ss}} \end{bmatrix} \begin{bmatrix} \ddot{\mathbf{q}}_\mathbf{m} \\ \ddot{\mathbf{q}}_\mathbf{s} \end{bmatrix} + \begin{bmatrix} \mathbf{C_{mm}} & \mathbf{C_{ms}} \\ \mathbf{C_{sm}} & \mathbf{C_{ss}} + \Omega\mathbf{G_{ss}} \end{bmatrix} \begin{bmatrix} \dot{\mathbf{q}}_\mathbf{m} \\ \dot{\mathbf{q}}_\mathbf{s} \end{bmatrix} + \begin{bmatrix} \mathbf{K_{mm}} & \mathbf{K_{ms}} \\ \mathbf{K_{sm}} & \mathbf{K_{ss}} \end{bmatrix} \begin{bmatrix} \mathbf{q}_\mathbf{m} \\ \mathbf{q}_\mathbf{s} \end{bmatrix} = \begin{bmatrix} \mathbf{f}_\mathbf{m} \\ \mathbf{f}_\mathbf{s} \end{bmatrix} \quad (3.8)$$

Using the second block row in equation (3.8), and setting the first and second derivatives to zero gives the following static elimination of $\mathbf{q_s}$ in terms of $\mathbf{q_m}$:

$$\mathbf{q_s} = -(\mathbf{K_{ss}}^{-1}\mathbf{K_{sm}})\mathbf{q_m} = -\mathbf{R_D}\mathbf{q_m} \quad (3.9)$$

The insertion of equation (3.9) into the first block row in equation (3.8) gives a reduced order model known as "Guyan Reduction". However, this reduction has the disadvantage that the second row coefficient sub-matrices in **M** and **C** do not appear in the process and the accuracy of the reduced model is compromised. This produced poor results in this application.

An alternative approach is developed by the author. Firstly, the vector $\mathbf{q_s}$ is eliminated from the equations by multiplying the second block row in equation (3.8) by a weighing matrix

$$\mathbf{R_E} = \mathbf{K_{ms}}\mathbf{K_{ss}}^{-1} \quad (3.10)$$

and then subtracting from the first block row of equation (3.8). The resulting equations are as follows:

$$(\mathbf{M_{mm}} - \mathbf{R_E M_{sm}})\ddot{\mathbf{q}}_\mathbf{m} + (\mathbf{M_{ms}} - \mathbf{R_E M_{ss}})\ddot{\mathbf{q}}_\mathbf{s} + (\mathbf{C_{mm}} - \mathbf{R_E C_{sm}})\dot{\mathbf{q}}_\mathbf{m} + (\mathbf{C_{ms}} - \mathbf{R_E C_{ss}} - \Omega \mathbf{R_E G_{ss}})\dot{\mathbf{q}}_\mathbf{s} + (\mathbf{K_{mm}} - \mathbf{R_E K_{sm}})\mathbf{q}_\mathbf{m} = \mathbf{f_m} - \mathbf{R_E f_s} \quad (3.11)$$

This equation does not contain $\mathbf{q_s}$ terms. However, the first and second derivatives of $\mathbf{q_s}$ still exist, which can be approximated by differentiating equation (3.9) twice with respect to time and substituting into equation (3.11), that will result in the following condensed equations:

$$\mathbf{M_R}\ddot{\mathbf{q}}_\mathbf{m} + (\mathbf{C_R} + \Omega \mathbf{G_R})\dot{\mathbf{q}}_\mathbf{m} + \mathbf{K_R}\mathbf{q}_\mathbf{m} = \mathbf{f_R} \quad (3.12)$$

where the reduced mass, damping, stiffness and gyroscopic matrices are given by:

$$
\begin{aligned}
\mathbf{M_R} &= \mathbf{M_{mm}} - \mathbf{R_E M_{sm}} - \mathbf{M_{ms} R_D} + \mathbf{R_E M_{ss} R_D} \\
\mathbf{C_R} &= \mathbf{C_{mm}} - \mathbf{R_E C_{sm}} - \mathbf{C_{ms} R_D} + \mathbf{R_E C_{ss} R_D} \\
\mathbf{G_R} &= \mathbf{R_E G_{ss} R_D} \\
\mathbf{K_R} &= \mathbf{K_{mm}} - \mathbf{R_E K_{sm}} \\
\mathbf{f_R} &= \mathbf{f_m} - \mathbf{R_E f_s}
\end{aligned}
\tag{3.13}
$$

The modified static displacement condensation (MSDC) technique developed here deals with symmetric and non-symmetric stiffness matrices. However, in the case of symmetric stiffness matrices, $\mathbf{R_E} = \mathbf{R_D^T}$. This is equivalent to the static condensation in displacement space (SDC) method suggested in [87]. Because the algorithm is partly static, the selection of master coordinates has a significant effect on the accuracy of the reduced order model. Therefore, the accuracy needs to be checked before using the model. If the accuracy is acceptable within the system bandwidth of interest, then this approach can be used. One important advantage of this model condensation compared with the use of 6 nodal planes in finite element modeling is that the reduced system has now only 12 degrees of freedom (instead of 24), but still covers the same 6 selected nodal planes. For completeness, a direct reduced order model was generated by using only 6 nodal planes in the finite element formulation.

Three criteria, namely time response, frequency response and eigenvalue plots, were used to assess the performance of the proposed model reduction tech-

nique [83], as discussed in section 3.4.

3.4 Model Reduction Comparison

The accuracy of reduced models are assessed here in the frequency and time domains. First, the natural frequencies calculated by the two reduced order models are compared with these obtained from the 12 element FEM (13 nodal planes) model at three different speeds (90, 120 and 145) rad/s in Table 3.4. Errors are calculated relative to the first column, and clearly indicate that the MSDC condensation method gives more accurate results than the 5 element FEM model. The first four pairs of natural frequencies are predicted within 0.1% accuracy.

Figures 3.4 and 3.5 show the average error value of the first four natural frequencies at running speeds of (90, 120 and 145) rad/s. Figures 3.4 shows the result for all models namely; 19-nodal plane model 76 × 76, 13-nodal plane model (full model) 52 × 52, 6-nodal plane model 24 × 24 and reduced model 12 × 12 with diagonal and non-diagonal system mass matrices representation when compared to the reference model of 23 model planes FEM model (92×92). Figure 3.5 indicates clearly that the 6-plane FEM model develops significant errors and deviates from the reference model with 18.61% for the non-diagonal model and 20.44% for the diagonal model.

The comparison clearly indicates that both models, the FEM 13-nodal non-

diagonal and the condensed non-diagonal model, have approximately the same error of 0.82% and 0.85%, respectively, as shown in figure 3.4.

The comparison in figure 3.4 shows the accuracy of the FEM 19-nodal diagonal mass matrix with the the highest accuracy of 0.64% with appropriate number of elements. The FEM 13-nodal plan model and the condensed model with diagonal representation have acceptable accuracy of 0.86% and 0.83%, respectively. While these models have the same mass matrix representation (diagonal) and have approximately the same precision, the condensed model has the minimum number of nodes that covers the required planes to develop an acceptable simulation environment. In conclusion, the condensed model with diagonal matrix representation will be used in this research.

A map of natural frequencies of the system (Campbell diagram) is generated by using the 6-nodal plane model and the reduced order model. The results are compared with the 13-nodal FEM reference model in figure 3.6. The condensed MSDC method results cannot be distinguished from the full model results. However, the reduced 6-nodal plane FEM produces significant shifts in all critical speeds (intersection points between the imaginary part of the eigenvalues and the synchronous line).

The unbalance responses in frequency domain were calculated for an unbalance of 0.5 gm at disk at non-driven end of the rotor for the rotational speed range of (0-500) rad/s. The amplitudes of maximum displacement along the shaft are plotted against the rotational speed in figure 3.7. Again, the response predicted by the condensed MSDC method can not be distinguished from the full model (13-nodal

plane) results, whereas the 5-element FEM model (6 nodal planes) predictions deviate from the full model results especially around the natural frequencies.

The final test is to compare the transient response in simulation with respect to changes in-out-of-balance disturbances at a constant rotational speed in the time domain. Initially an unbalance of 0.5 gm is placed at the disk at the non-driven end of the rotor. After 5 synchronous cycles, an additional unbalance of 22 gm is introduced at 120 rad/s and 11 gm at 145 rad/s is introduced at the same station. Figures 3.8 and 3.9 compare the unbalance response (normalized with respect to retainer bearing radial clearance) of the condensed model at the second magnetic bearing (MB2) location with that obtained from the reference model at rotational speeds of 120 rad/s and 145 rad/s respectively. The inaccuracies introduced by using 6-nodal plane can clearly be observed from these figures, whereas the condensed MSDC method results are very close to the full model results.

These tests clearly indicate that MSDC gives more accurate results than the 6-nodal plane FEM model. Furthermore, the 12×12 model generated by MSDC has half the size of the 6-nodal plane FEM model that of system matrices of size 24×24. It is therefore beneficial to use as many mass stations as needed for accurate prediction of modes within the operational bandwidth, and then apply MSDC condensation, which preserves the selected physical displacements and the external inputs such as unbalance distribution and the control forces.

3.5 Summary

The author details the modelling of the rotor using the finite element method (FEM). The FEM model accuracy is investigated. A novel model condensation techniques (MSDC) was developed and tested for rotor/bearing systems. The technique accuracy was examined in both the frequency and time domains.

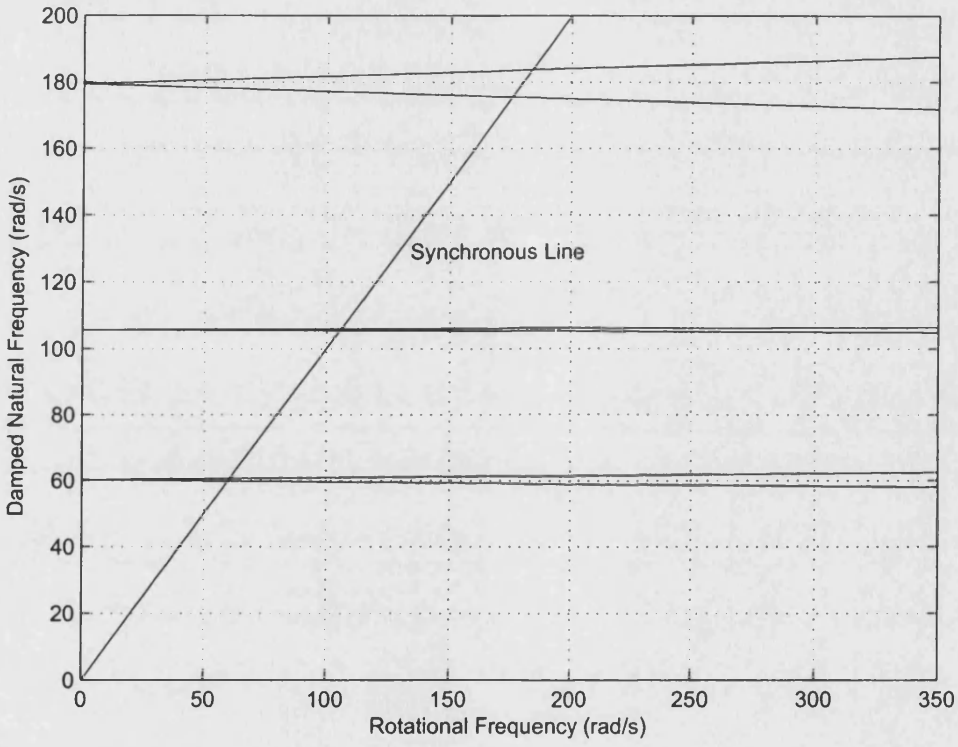

Figure 3.1: Campbell diagram for FEM 13-node model

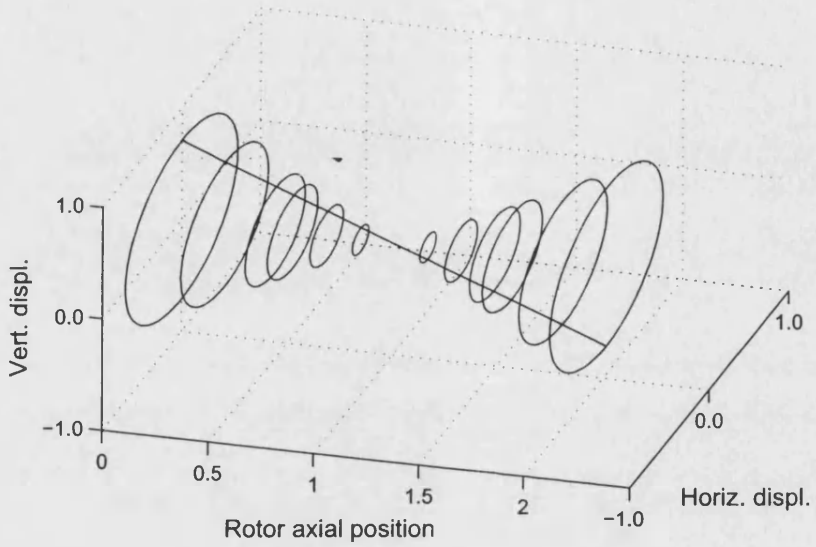

(a) Conical mode at $\omega_n \approx$ 61 rad/s (10 Hz)

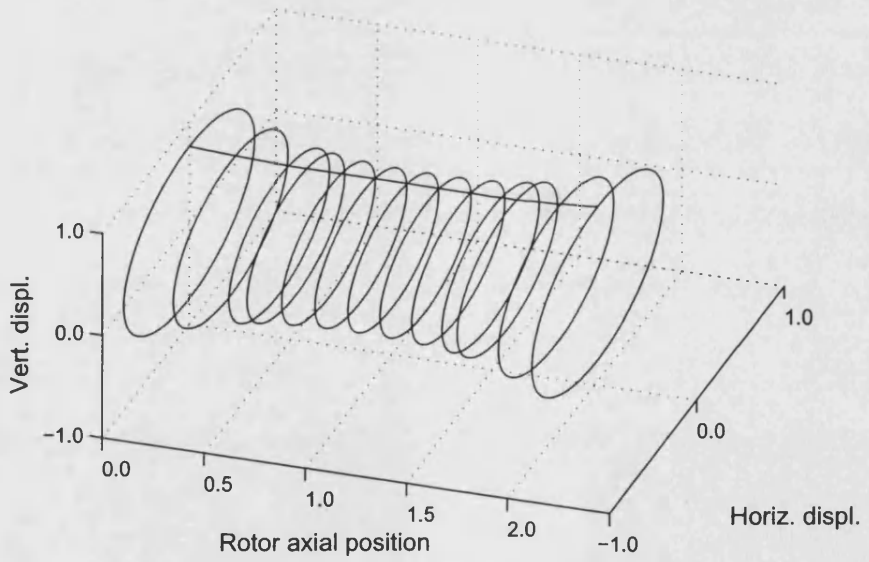

(b) Cylindrical mode at $\omega_n \approx$ 106 rad/s (17 Hz)

Figure 3.2: Rigid body mode shapes of the rotor

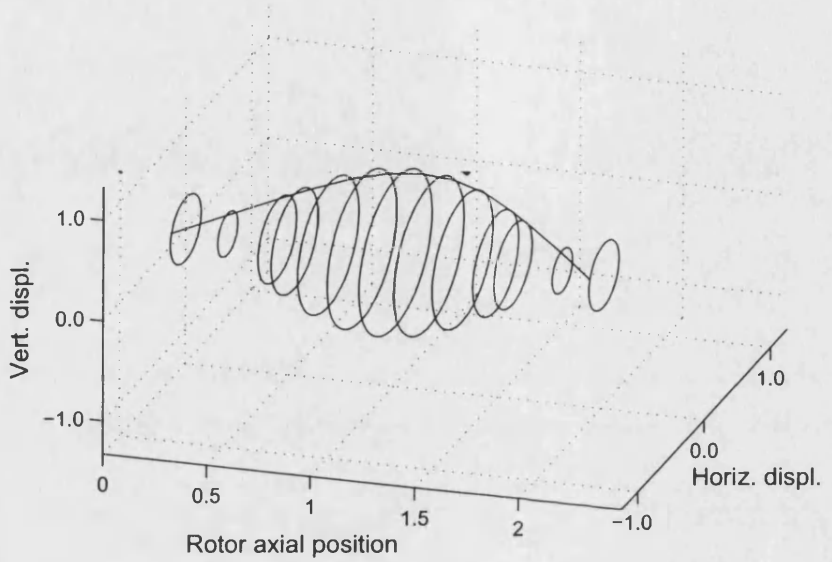

(a) First flexural mode at $\omega_n \approx$ 179 rad/s (28 Hz)

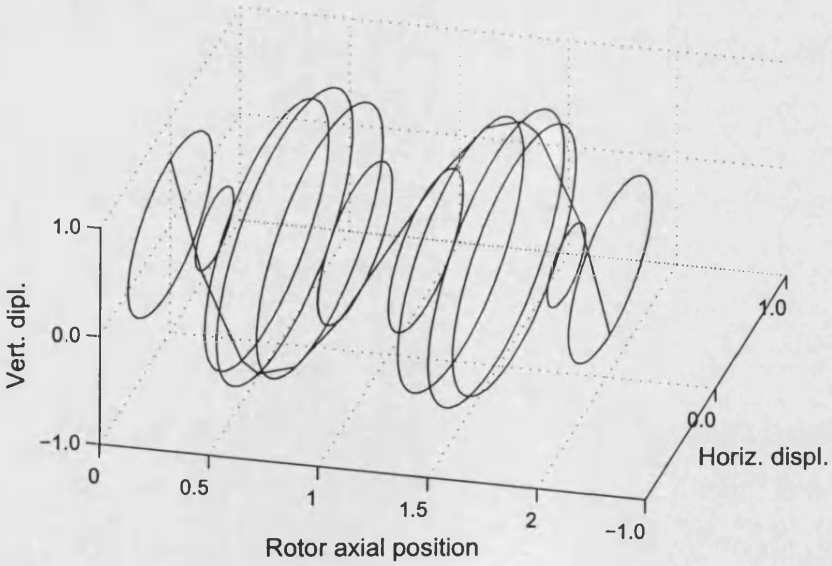

(b) Second flexural mode at $\omega_n \approx$ 429 rad/s (70 Hz)

Figure 3.3: Flexural mode shapes of the rotor

Table 3.1: Eigenvalues of various FEM

23-Nodal Plane Model					
Non-diagonal (*Reference Model*)			Diagonal		
90 rad/sec	120 rad/sec	145 rad/sec	90 rad/sec	120 rad/sec	145 rad/sec
60.94	60.74	60.57	60.90	60.71	60.55
62.16	62.36	62.53	62.08	62.28	62.45
106.01	105.91	105.83	105.93	105.85	105.77
106.53	106.62	106.69	106.46	106.55	106.61
179.20	178.53	177.97	178.88	178.23	177.69
183.30	183.99	184.58	182.87	183.55	184.11
429.17	427.91	426.85	428.47	427.24	426.21
436.69	437.93	438.96	435.81	437.02	438.03
19-Nodal Plane Model					
Non-diagonal			Diagonal		
90 rad/sec	120 rad/sec	145 rad/sec	90 rad/sec	120 rad/sec	145 rad/sec
60.95	60.75	60.58	60.78	60.59	60.43
62.15	62.36	62.53	61.96	62.16	62.32
106.01	105.92	105.84	105.79	105.70	105.62
106.53	106.62	106.68	106.32	106.41	106.48
179.22	178.55	178.00	177.60	176.97	176.44
183.28	183.97	184.54	181.51	182.17	182.72
429.21	427.96	426.91	424.48	423.27	422.27
436.65	437.88	438.91	431.65	432.83	433.82
13-Nodal Plane Model					
Non-diagonal			Diagonal		
90 rad/sec	120 rad/sec	145 rad/sec	90 rad/sec	120 rad/sec	145 rad/sec
61.75	61.55	61.38	61.53	61.33	61.16
62.97	63.18	63.35	62.73	62.93	63.10
107.42	107.33	107.26	107.14	107.05	106.97
107.91	107.99	108.05	107.65	107.73	107.79
179.68	179.00	178.44	178.17	177.51	176.96
183.84	184.55	185.14	182.19	182.87	183.44
430.84	429.59	428.54	425.62	424.40	423.38
438.31	439.54	440.56	432.87	434.07	435.07

Table 3.2: Percentage errors in eigenvalues when reducing from 23 to 19 nodes in non-diagonal FEM modelling

90 rad/sec	120 rad/sec	145 rad/sec
0.0086	0.0115	0.0139
0.0085	0.0113	0.0137
0.0030	0.0040	0.0048
0.0025	0.0033	0.0040
0.0111	0.0148	0.018
0.0115	0.0153	0.0185
0.0084	0.0110	0.0133
0.0076	0.0102	0.0124

Table 3.3: Percentage errors in eigenvalues comparing beween the reference model and 13-node diagonal FEM

90 rad/sec	120 rad/sec	145 rad/sec
0.9593	0.9664	0.9722
0.9171	0.9100	0.9042
1.0700	1.0742	1.0780
1.0439	1.0400	1.0364
0.5731	0.5680	0.5638
0.6043	0.6097	0.6140
0.8286	0.8209	0.8144
0.8736	0.8810	0.8870

Table 3.4: Eigenvalues and errors with reference to the FEM 13-node model at $\Omega = 120$ rad/s and $\Omega = 145$ rad/s

FEM-13	Condensed		FEM-6	
ω_n(rad/s)	ω_n(rad/s)	% error	ω_n(rad/s)	% error
Ω =90 rad/s				
61.5265	61.5268	0.0005	92.9079	51.0046
62.7287	62.7294	0.0012	94.1161	50.0368
107.1388	107.1400	0.0011	115.6904	7.9818
107.6457	107.6508	0.0048	115.6861	7.4694
178.1691	178.2578	0.0498	158.8308	-10.8539
182.1904	182.2475	0.0314	163.2246	-10.4099
425.6153	425.9769	0.0849	387.4924	-8.9571
432.8727	432.9693	0.0223	393.5813	-9.0769
Ω =120 rad/s				
61.3277	61.3283	0.0009	92.7069	51.1663
62.9306	62.9318	0.0019	94.3178	49.8760
107.0498	107.0506	0.0007	115.6929	8.0739
107.7259	107.7319	0.0056	115.6875	7.3906
177.5112	177.6085	0.0549	158.1038	-10.9331
182.8724	182.9279	0.0304	163.9623	-10.3406
424.3953	424.8178	0.0996	386.4715	-8.9360
434.0712	434.1408	0.0160	394.5896	-9.0957
Ω =145 rad/s				
61.1625	61.1633	0.0013	92.5394	51.3010
63.0992	63.1008	0.0025	94.4860	49.7420
106.9746	106.9751	0.0004	115.6954	8.1522
107.7919	107.7987	0.0063	115.6893	7.3265
176.9657	177.0710	0.0595	157.4990	-11.0003
183.4431	183.4981	0.0300	164.5782	-10.2838
423.3765	423.8534	0.1127	385.6195	-8.9181
435.0675	435.1183	0.0117	395.4283	-9.1110

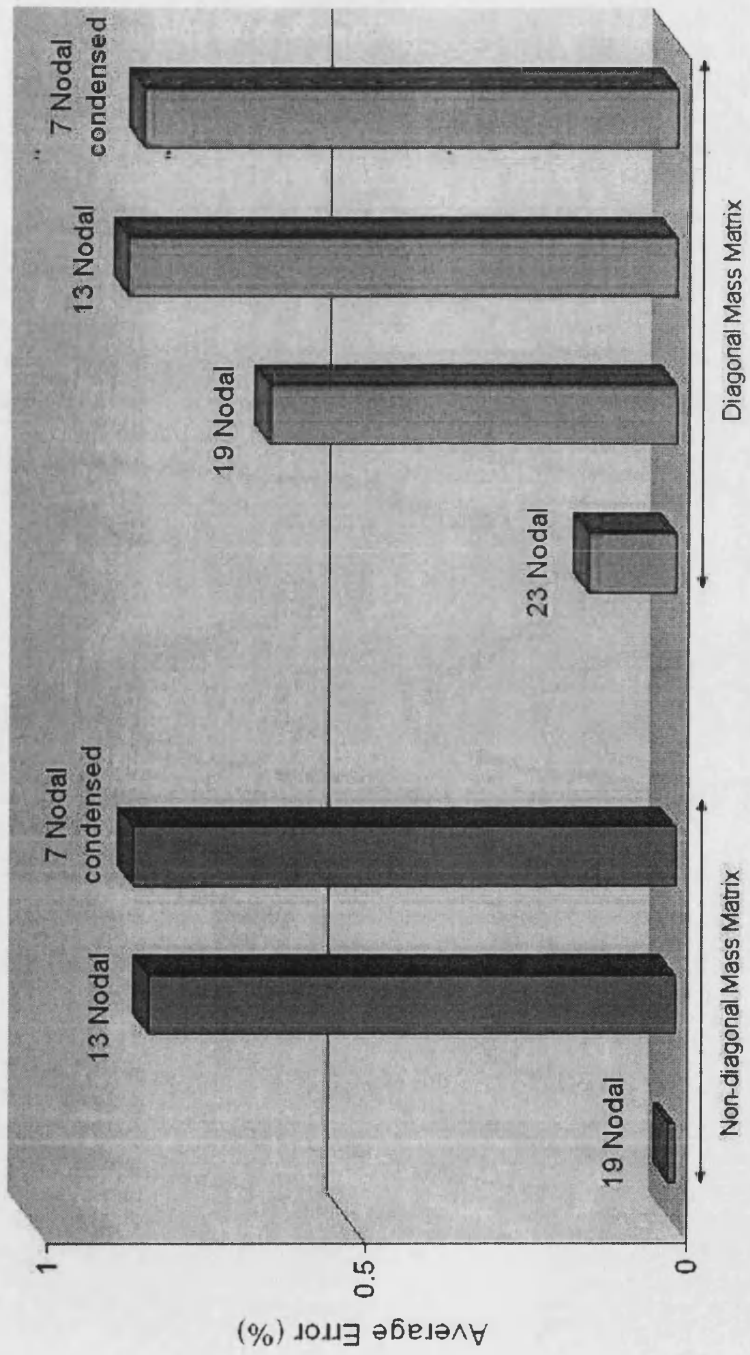

Figure 3.4: Comparison of FEM accuracy with various model mass matrix representations (blue: non-diagonal, pink: diagonal)

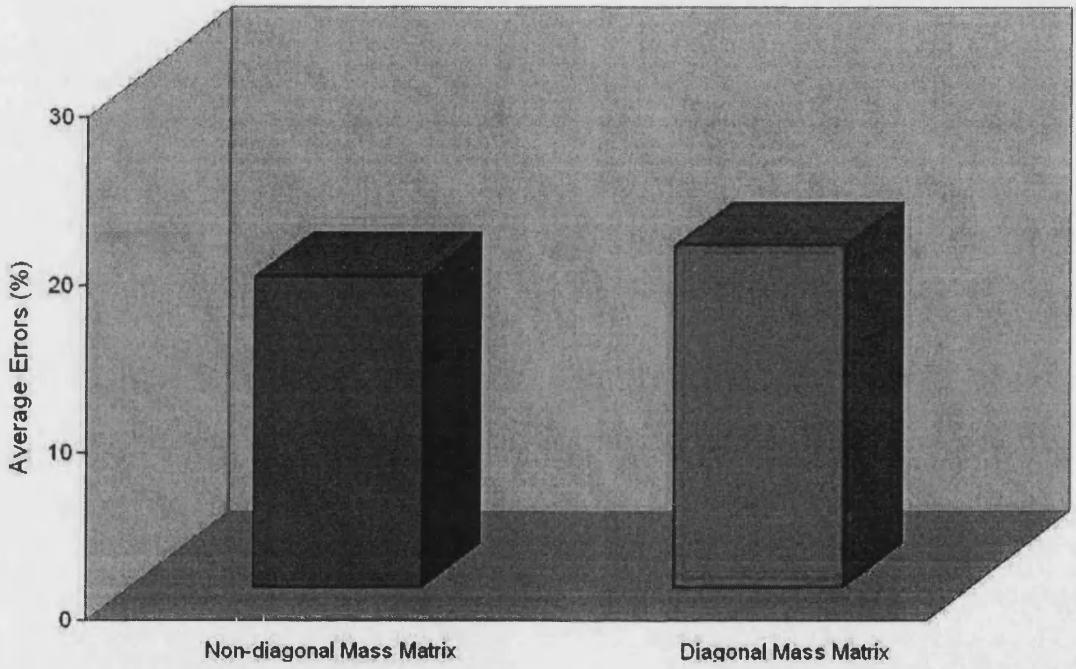

Figure 3.5: FEM Accuracy of 6-nodal physical reduction model with different mass matrix representation (blue: non-diagonal, pink: diagonal)

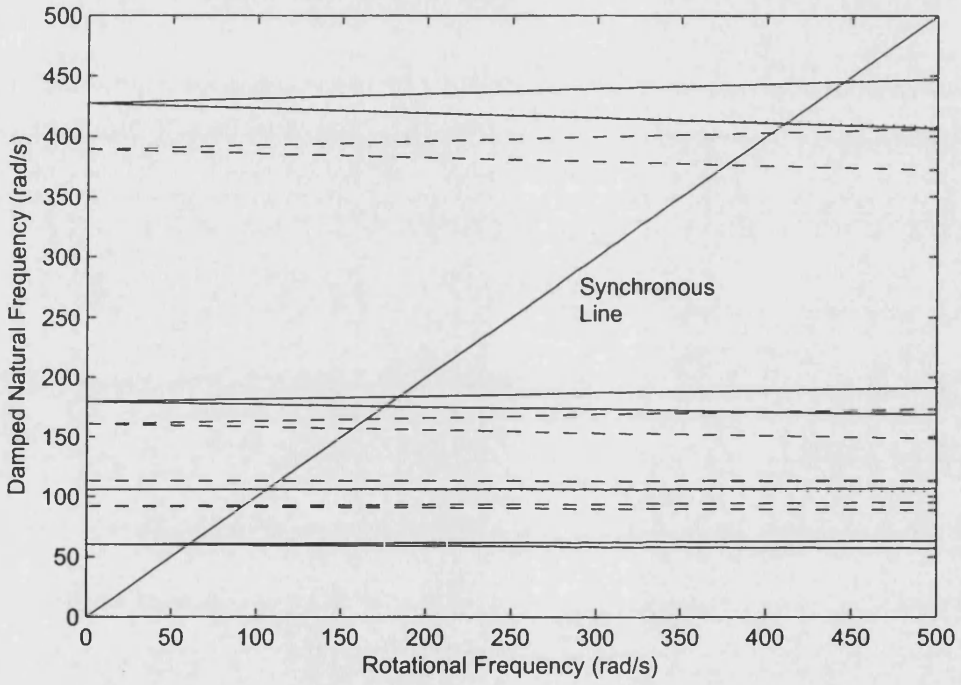

Figure 3.6: Eigenvalue map (line: FEM 13-node model, dotted: condensed, dashed: FEM 6-node model)

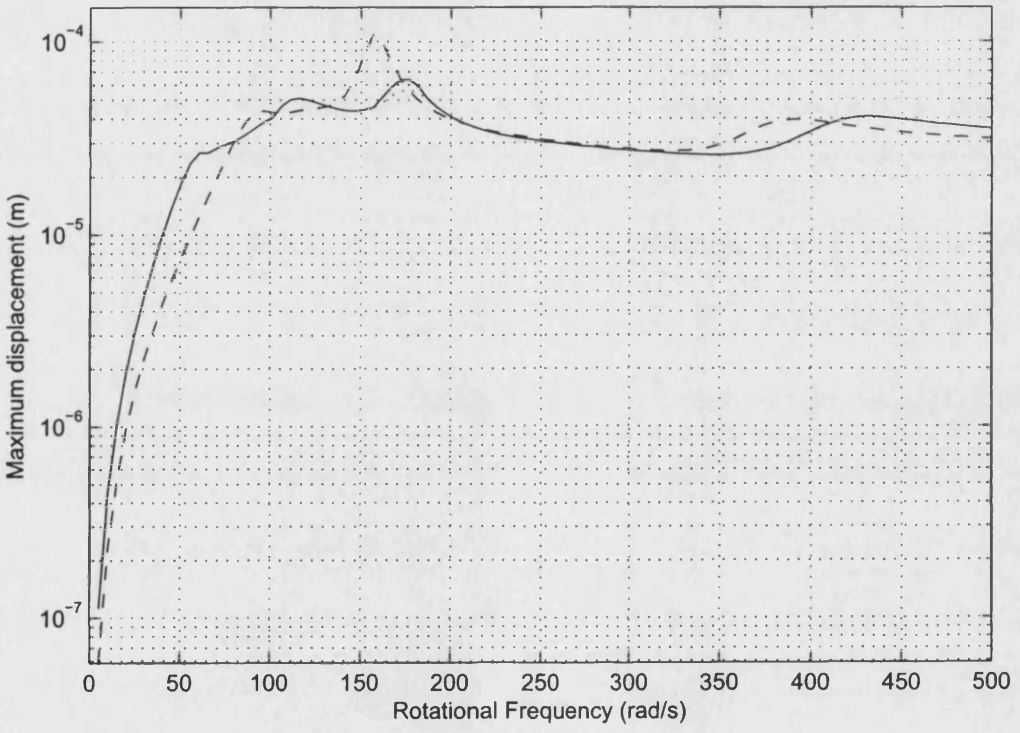

Figure 3.7: Rotor unbalance frequency response (line: FEM 13-node model, dotted: condensed, dashed: FEM 6-node model)

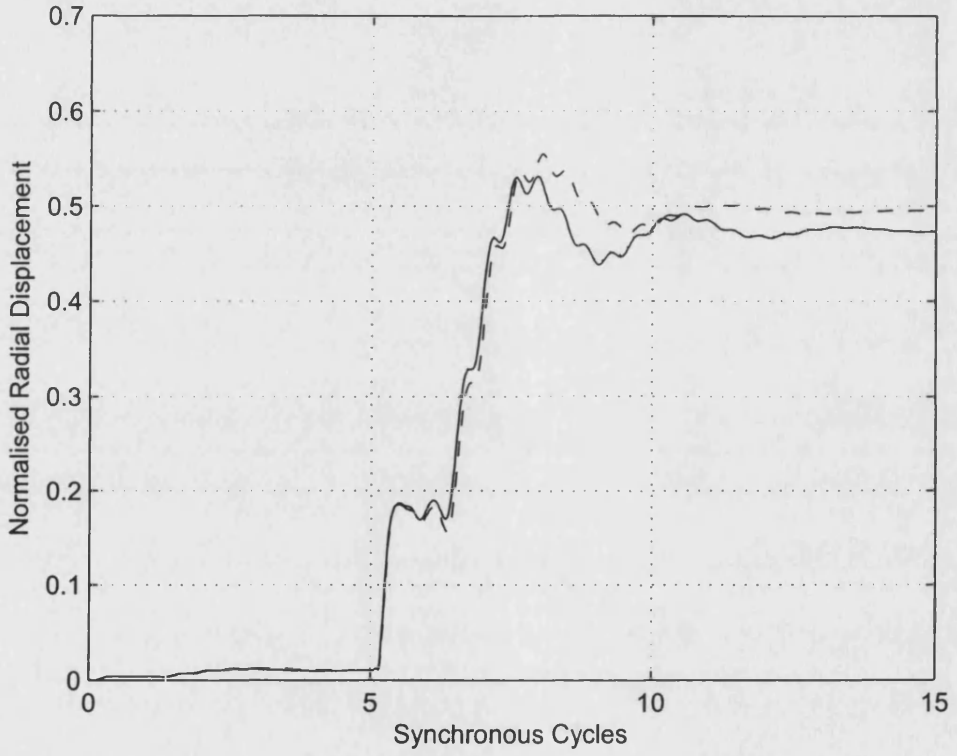

Figure 3.8: Rotor transient response at MB2 with $\Omega = 120$ rad/s (line: FEM 13-node model, dotted: condensed, dashed: FEM 6-node model)

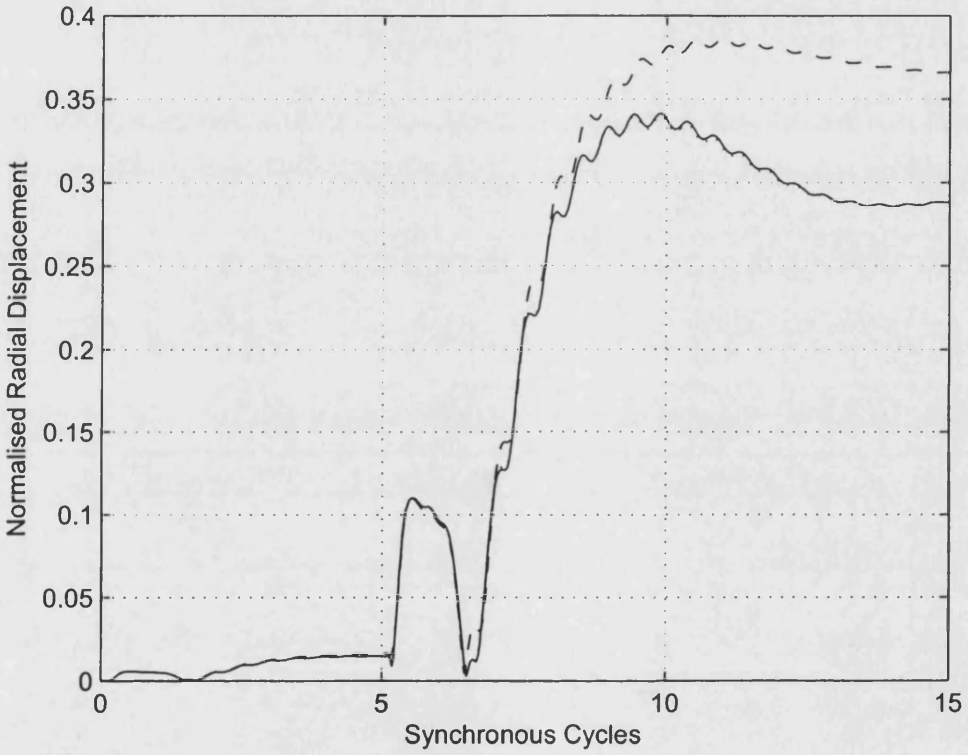

Figure 3.9: Rotor transient response at MB2 with $\Omega = 145$ rad/s (line: FEM 13-node model, dotted: condensed, dashed: FEM 6-node model)

Chapter 4

Contact Dynamic Analysis and Modelling

4.1 Introduction

Magnetic bearing systems incorporate retainer bearings to prevent physical interaction between rotor and stator laminations. The impact or rub problem in rotating machines is caused by various phenomena involving continuous or intermittent dynamical contact between the rotor and the stationary components. Rotor contact is clearly undesirable but tolerated in some cases for short contact periods. The resulting impulsive forces contain components in both radial and axial directions acting directly on the rotor.

The tangential friction force between the rotor and the retainer bearing may be sufficiently high to impose backward whirl motion on the rotor orbit. In such a case, the rotor is in dangerous condition and may result in damage of the system. If the relative velocity between the rotor and retainer bearing approaches zero, the rotor enters into a roll motion on the inner surface of the retainer bearing. The frequency of this mode is much higher than the rotational speed resulting in large forces transmitted through the shaft to other components causing extensive damage the system. Modelling system dynamics under sliding and rolling conditions is described in this chapter.

4.2 Classical Contact Model

The classical modelling of rotor interaction with retainer bearings involves introducing contact forces normal to the retainer bearing surface at the contact point. The basic formula of contact forces induced as a function of contact stiffness at the contact point and the penetration depth δ_i, [50, 66], is defined as follows:

$$F_c = K_c \delta_i^n \tag{4.1}$$

where

$$n = 1 \quad , \qquad \delta_i = \sqrt{x_i^2 + y_i^2} - C_r \tag{4.2}$$

The Hertzian contact model uses the same formula with $n = 3/2$. This model is more suitable for rigid body and low impact speed since it does account for energy dissipation with the coefficient of restitution equal to unity [67]. For a more realistic contact model, it is necessary to have more involved expression. The contact force formulation is often augmented with a damping term $\hat{C}_c$ acting on the penetration δ_i at the contact point to reflect energy dissipation [63, 73, 88]. That allows effective modelling of contact as a spring-damper system as follow:

$$F_c = \begin{cases} K_c\,\delta_i + C_c\,\dot{\delta}_i, & \text{if } \delta_i \geq 0 \\ 0, & \text{if } \delta_i < 0 \end{cases} \tag{4.3}$$

In another study [63], these parameters were made to increase exponentially until a maximum penetration at which contact forces are represented of 95% of the values of K_c and C_c, is reached:

$$F_c = \ell\left(K_c\,\delta_i + C_c\,\dot{\delta}_i\right) \tag{4.4}$$

where

$$\ell = 1 - \exp\left[\frac{-\delta_i}{\delta_{max}/3}\right] \tag{4.5}$$

More complicated alternative formulations are given in the literature in order

to mimic the observed behaviour and to overcome the problems of the spring-damping model (see section 4.2.2). It includes non-linear damping and incorporates an impact coefficient of restitution [65, 66]. The coefficient of restitution can be determined experimentally [89]. The contact forces are modelled as follows [66]:

$$F_c = K_c \delta_i^{3/2} \left(1 + \frac{3}{2} C_c \dot{\delta}_i\right) \tag{4.6}$$

The contact damping is related to the coefficient of restitution, ε, by:

$$\varepsilon = 1 - C_c \dot{\delta}|_{\delta=0} \tag{4.7}$$

Ulbrich *et al.* [75] modelled the force of contact when rotor is in contact with retainer bearing taking into account the energy dissipation and the Hertzian contact stiffness. The force-displacement relationship is defined as follows:

$$f_c = \Theta \left(1 + \frac{3}{2} \alpha_k \dot{\delta}\right) K_c (\delta - \delta_0)^{3/2} \tag{4.8}$$

where

$$\Theta = \begin{cases} 1, & \text{if } \delta \geq \delta_0 \\ 0, & \text{if } \delta < \delta_0 \end{cases} \tag{4.9}$$

and α_k denotes the loss in kinetic energy per cycle of contact.

All classical models allow the the integration of equation of motion during the interval of contact. It is integrated with high values of contact stiffness and damping, which results in stiff differential equations.

4.2.1 Friction Forces

The friction force at the contact point is another key aspect of contact modelling that adds another degree of complication. The friction forces for dry contact (metal to metal) are related to the normal contact forces F_n via a dynamic coefficient of friction μ. The direction of friction force is related to the relative velocity v between the rotor and the retainer bearing. In this application, it is assumed that the bearing housing does not move. Friction forces can be formulated as Coulomb friction, which takes the following form [50, 65]:

$$F_f = sgn(v) \times \mu \times F_n \tag{4.10}$$

where the relative velocity v between the rotor and the retainer bearing is:

$$v = R_s\Omega + C_r\dot{\vartheta}_k \tag{4.11}$$

where $\dot{\vartheta}_k$ is the whirl speed.

Then, the total contact force is determined as the sum of the normal contact force and friction force acting in the direction of the relative velocity, which takes the following complex number form:

$$F_c = (1 + i\mu)\, F_n \tag{4.12}$$

These forces are calculated using global axes and included into the external force vector of the rotor/bearing system using the coordinate system as illustrated in section 4.3.1.

4.2.2 Classical Model Deficiencies

The choice of contact model will have great influence on the convergence of the numerical simulation solution, thus it should be decided with care. The contact model described in equation (4.3) has deficiencies. The function is not differen-

tiable due to discontinuity at $\delta_i = 0$ as indicated by point A in figure 4.1. It provides meaningless negative contact force as indicated by point B in figure 4.1 due to a relative velocity $\dot{\delta}$, [65, 66, 67]. This linear model can be modified by introducing a switching function $\sigma(\delta, \dot{\delta})$ to prevent discontinuities in the contact forces [90]. The modified linear function of stiffness-damping model behaviour is shown in figure 4.2 and can be formulated as follows:

$$F_c = \left(K_c \delta_i + C_c \dot{\delta}_i\right) \sigma(\delta, \dot{\delta}) \tag{4.13}$$

In a more detailed contact model, the contact force relations can be non-linear in stiffness and/or damping, with the implementation of a non-linear relationship as explained in equation (4.6), both elastic and damping forces should be initially at the zero point.

However, whatever method is selected, the estimation of the contact stiffness and damping parameters is extremely difficult because they are functions of the surface temperature, rotor penetration into the retainer bearing, surface damage and material properties. A high stiffness coefficient K_c is required to express the contact force in terms of the penetration depth δ_i. This introduces high frequency oscillations and hence computational difficulties and inefficiencies.

4.3 Lagrangian Approach for Forward Whirl

In this research work the author developed a new approach for modelling contact dynamic, which avoids the need for modelling contact forces and consequently eliminates the classical theory deficiencies. In this approach, the contact case is treated as a constraint on the system, reducing the degrees of freedom by one for each contact location. The Lagrangian formulation dynamics handles constraints on the generalized coordinates through Lagrange multipliers. The constraint forces are calculated automatically during the integration of system equations. This method will be first explained assuming a single contact, and then will be extended to multiple contact cases. In case of a high friction coefficient between the rotor and the bearing inner surface, the rotor may experience a backward whirl. If the relative speed approaches zero, the stiction may cause a rolling motion. The rolling motion may be considered through constrained Lagrangian dynamics in a computationally efficient manner and is also discussed.

4.3.1 Single Contact Dynamics Modelling

The contact will occur when the radial displacement of the rotor at a bearing location reaches a clearance value C_r. During contact, the retainer bearing constraints the radial displacement of the rotor. Assuming the contact occurs at the k^{th} nodal plane, the subsequent motion of the rotor will be constrained by the following holonomic constraint equation:

$$h_k = x_k^2 + y_k^2 - C_r^2 = 0 \tag{4.14}$$

This can be incorporated into the reduced order rotor-bearing equations through a Lagrange multiplier λ_k:

$$\mathbf{M_R}\ddot{\mathbf{q}}_\mathbf{m} + \mathbf{J}^T\lambda_k = \mathbf{f_R} - \mathbf{C_R}\dot{\mathbf{q}}_\mathbf{m} - \mathbf{K_R}\mathbf{q_m} \tag{4.15}$$

where **J** is the Jacobian row vector of the constraint equation, i.e. the partial derivatives of the constraint equation with respect to generalized coordinates. Introduction of the Lagrange multiplier coefficient λ_k increases the number of unknowns by one. An additional equation is needed, which can be brought in by double differentiating equation (4.14):

$$\dot{h}_k = 2x_k\dot{x}_k + 2y_k\dot{y}_k = 0 \tag{4.16}$$

$$\ddot{h}_k = 2x_k\ddot{x}_k + 2y_k\ddot{y}_k + 2\dot{x}_k^2 + 2\dot{y}_k^2 = 0 \tag{4.17}$$

Combining equation (4.15) and equation (4.17) gives the following differential-algebraic equations to be solved for $\ddot{\mathbf{q}}_\mathbf{m}$ and λ_k:

$$\begin{bmatrix} \mathbf{M_R} & \mathbf{J}^T \\ \mathbf{J} & \mathbf{0} \end{bmatrix} \times \begin{bmatrix} \ddot{\mathbf{q}}_\mathbf{m} \\ \lambda_k \end{bmatrix} = \begin{bmatrix} \mathbf{f_R} - \mathbf{C_R}\dot{\mathbf{q}}_\mathbf{m} - \mathbf{K_R}\mathbf{q}_\mathbf{m} \\ \mathbf{D}(\mathbf{q}_\mathbf{m}, \dot{\mathbf{q}}_\mathbf{m}) \end{bmatrix} \tag{4.18}$$

where

$$\mathbf{J} = [\, 0 \;\cdots\; -2x_k \;\; 0 \cdots \;\; -2y_k \;\cdots\; 0 \,] \tag{4.19}$$

$$D = 2\dot{x}_k^2 + 2\dot{y}_k^2$$

The contact force can be obtained from the Lagrange multiplier λ_k as follows:

$$\mathbf{F}_c = -\mathbf{J}^T\lambda_k \tag{4.20}$$

This gives two components in the x and y directions at the k^{th} nodal plane. These can be converted to the r and s axes by using the direction cosine matrix:

$$\beta_k = \begin{bmatrix} \cos\vartheta_k & -\sin\vartheta_k \\ \sin\vartheta_k & \cos\vartheta_k \end{bmatrix} = \frac{1}{C_r}\begin{bmatrix} x_k & -y_k \\ y_k & x_k \end{bmatrix} \tag{4.21}$$

The constraint force $\mathbf{F_c}$ should produce zero component in the s direction. The force component in the r direction is the contact force, and should be negative (i.e. towards the centre of the bearing) during the contact to keep the rotor on the inner surface of the retainer bearing. If the contact force changes direction, then at the zero crossing, the simulation should be switching to the non-contact case. The whole process is summarized in figure 4.4. In the non-contact case the value of the constraint h_k in equation (4.14) should be negative. If a zero crossing is detected, then the simulation switches to the contact case.

The one important point when switching to the contact case is the adjustment of the initial conditions. The constraint equation λ_k is automatically satisfied because of the switching condition, but not the derivative of the constraint in equation (4.16). The following resetting of initial conditions for $\dot{x}_k(0^-)$ and $\dot{y}_k(0^-)$, $\dot{x}_k(0^+)$ and $\dot{y}_k(0^+)$, ensures zero velocity in the r direction, while keeping the velocity in the s direction the same as at the time of the contact:

$$\begin{aligned} \dot{x}_k(0^+) &= (1/C_r^2)(\dot{x}y^2 - \dot{y}xy) \\ \dot{y}_k(0^+) &= (1/C_r^2)(\dot{y}x^2 - \dot{x}xy) \end{aligned} \tag{4.22}$$

where $(\dot{x}_k(0^-)\ ,\ \dot{y}_k(0^-))$ and $(\dot{x}_k(0^+)\ ,\ \dot{y}_k(0^+))$ are the velocity values just before and after the contact at zero crossing point, respectively.

Calculating the initial condition using equation (4.22) may produce some numerical errors in the derivative of the constraint equation (4.16). To avoid this prob-

lem, the initial conditions will be calculated using equations (4.22) and (4.16). Equation (4.22) can be rewritten as follows:

$$\begin{bmatrix} \dot{x}_k(0^+) \\ \dot{y}_k(0^+) \end{bmatrix} = \begin{cases} \begin{bmatrix} (1/C_r^2)(\dot{x}y^2 - \dot{y}xy) \\ -(x_k/y_k)\,\dot{x}_k(0^+) \end{bmatrix}, & \text{if} \quad |y_k| \geq |x_k| \\ \begin{bmatrix} -(y_k/x_k)\,\dot{y}_k(0^+) \\ (1/C_r^2)(\dot{y}x^2 - \dot{x}xy) \end{bmatrix}, & \text{otherwise} \end{cases} \tag{4.23}$$

This will ensure that equation (4.16) is accurately satisfied, and also problems with dividing by small numbers or zeros are avoided in equation (4.22).

When switching from the contact to the non-contact case, there is no need to make any adjustment to the states, as the initial conditions are the same as the values of states just before coming out of contact.

It is straightforward to incorporate the friction force into the system, which acts along the tangential s direction with a magnitude proportional to the normal constraint (contact) force as explained in section 4.2.1.

It is possible to use the contact case model in equation (4.24) for the non-contact case by simply replacing the last row (i.e. the second derivative of the constraint) with $\lambda_k = 0$ as follows:

$$\begin{bmatrix} \mathbf{M_R} & \mathbf{J}^T \\ \mathbf{0} & \mathbf{I} \end{bmatrix} \times \begin{bmatrix} \ddot{\mathbf{q}}_\mathbf{m} \\ \lambda_k \end{bmatrix} = \begin{bmatrix} \mathbf{f_R} - \mathbf{C_R}\dot{\mathbf{q}}_\mathbf{m} - \mathbf{K_R}\mathbf{q}_\mathbf{m} \\ \mathbf{0} \end{bmatrix} \tag{4.24}$$

This has significant benefits in the multiple contact case as discussed in section 4.3.3.

4.3.2 Single Contact Simulation Results

A number of cases were simulated by using the constrained Lagrangian formulation of single plane contact. The initial steady-state orbit was obtained by introducing an unbalance of 50 gm applied to the disk at the non-driven end of the rotor. Both magnetic bearings were controlled by local PID controllers with a proportional gain to give an effective bearing stiffness of 10^6 N/m after overcoming the inherent negative stiffness of the magnetic bearing. The derivative gain was set to give an equivalent damping of 5000 Ns/m.

In order to initiate a contact, a sudden increase of out-of-balance disturbance of 44 gm was introduced at the start of 5^{th} cycle to the disk at the non-driven end of the rotor at a constant rotational speed of 90 rad/s. This causes a contact at the first magnetic bearing (MB1) as shown in figures 4.5 and 4.6. The added unbalance is removed after a pre-defined number of synchronous periods following the contact to check if recovery takes place. This is an important indication to assess whether it is possible to recover the rotor if appropriate control action was implemented and if the magnetic bearings were operational when contact occurred.

Figure 4.5 shows the resulting orbits at both magnetic bearing locations. Figure 4.6 shows the radial displacement at the first magnetic bearing (MB1), and clearly indicates contact. The contact forces are below 1 kN. The displacements are normalized by the clearance of the retainer bearings C_r = 0.75 mm, and time is normalized by the synchronous period $2\pi/\Omega$. The results predict con-

tinuous sliding motion except during a short period of non-contact (bouncing) behaviour. When the additional out-of-balance is removed at the 10^{th} cycle, the rotor position recovers to its original orbit.

Another simulation was run to demonstrate a single contact case at a higher rotational speed of 120 rad/s, which is above the second critical speed. The initial steady-state was obtained with unbalance of 50 gm applied at the middle disk next to second magnetic bearing (MB2). An additional out-of-balance disturbance of 12 gm is introduced at 5^{th} cycle to the same disk location. Continuous rubbing contact motion at the MB2 retainer bearing can clearly be observed in figures 4.7 and 4.8. The normalized orbits at both bearings are shown in figure 4.7. The corresponding normalized radial displacements are shown in figure 4.8 with contact forces up to 1.35 kN. The constrained Lagrangian technique considers the retainer bearings as represented by a rigid surface without any penetration. This is demonstrated in figure 4.8 where the normalized radial displacement has a value of unity when contact occurs.

4.3.3 Multiple Contact Dynamics Modelling

The simulated experimental system has two active magnetic bearings. The contact between the rotor and the retainer bearings may happen at either retainer bearing or both simultaneously. There are four possible cases at any given time; no contact, contact at the first retainer bearing (node $k1$) only, contact at second retainer bearing (node $k2$) only, and contact at both retainer bearings (nodes $k1$ and $k2$). The first three cases can be simulated by the single contact method described in section 4.3.1. The case with contact at both retainer bearings can be handled by introducing two constraint equations:

$$\begin{aligned} h_1 &= x_{k1}^2 + y_{k1}^2 - C_r^2 = 0 \\ h_2 &= x_{k2}^2 + y_{k2}^2 - C_r^2 = 0 \end{aligned} \tag{4.25}$$

The constrained dynamic equation of the motion will have the same general form as equation (4.24). The constrained Jacobian matrix $\mathbf{J}$ contains the partial derivatives of both constraint equations with respect to generalized coordinates. The Lagrange multiplier vector λ contains two Lagrange multipliers, λ_1 and λ_2, corresponding to each constraint equation:

$$\mathbf{J} = \begin{bmatrix} 0 & -2x_{k1} & 0 & \dots & -2y_{k1} & 0 & \dots & 0 \\ 0 & \dots & -2x_{k2} & 0 & \dots & -2y_{k2} & \dots & 0 \end{bmatrix}$$

$$\mathbf{D} = \begin{bmatrix} 2\dot{x}_{k1}^2 + 2\dot{y}_{k1}^2 \\ 2\dot{x}_{k2}^2 + 2\dot{y}_{k2}^2 \end{bmatrix} \quad ; \quad \lambda = \begin{bmatrix} \lambda_1 \\ \lambda_2 \end{bmatrix} \tag{4.26}$$

The switching between different cases are decided for each retainer bearing individually as in the single contact case. The model will automatically produce the contact forces. The adjustment of initial conditions when changing from non-contact to contact case is handled in a similar manner as in the single contact case.

Instead of using four different models to cover all possible cases, a single model, based on the double contacts, can be adopted and modified according to the mode of operation. If either retainer bearing operates in the non-contact case, the corresponding row (i.e. one of the last two rows) can be replaced by $\lambda_1 = 0$ or $\lambda_2 = 0$ accordingly. For example for the case of the contact at the second retainer bearing only. The last two rows on the left hand side of equation (4.24) would be as follows:

$$\left[\begin{array}{cccccc|cc} 0 & \cdots & 0 & 0 & \cdots & 0 & \cdots & 1 & 0 \\ 0 & \cdots & -2x_{k2} & 0 & \cdots & -2y_{k2} & \cdots & 0 & 0 \end{array}\right] \tag{4.27}$$

The **D** matrix on the right hand side is given by:

$$\mathbf{D} = \begin{bmatrix} 0 \\ 2\dot{x}_{k2}^2 + 2\dot{y}_{k2}^2 \end{bmatrix} \tag{4.28}$$

This would ensure that λ_1 is set to zero. For the non-contact case, both λ_1 and λ_2 are set to zero, by replacing the last two rows on the left hand side with zeros except the unity diagonal elements as follows:

$$\left[\begin{array}{cccccc|cc} 0 & \cdots & 0 & 0 & \cdots & 0 & \cdots & 1 & 0 \\ 0 & \cdots & 0 & 0 & \cdots & 0 & \cdots & 0 & 1 \end{array}\right] \tag{4.29}$$

The **D** matrix in equation (4.28) should also be set to zero. Moreover, this general modelling technique can easily be extended to any number of possible contact sites. This eliminates the need to develop separate models for increasingly large number of possible combinations of contact locations.

4.3.4 Multiple Contact Simulation Results

The multiple contact approach simulates simultaneous contacts occurring at both retainer bearings. The initial steady state orbits were obtained by introducing a small unbalance of 0.5 gm applied to the disk at the non driven end of the rotor. There are four possible operational modes; 0: non-contact, 1: only the first magnetic bearing (MB1) is in contact, 2: only the second magnetic bearing (MB2) is in contact, 3: both magnetic bearings are in contact.

The first simulation was undertaken at a rotational speed of 260 rad/s, which is well above the first flexural mode frequency. Then the contact was initiated with the introduction of a sudden out of balance of 25 gm at the non-driven end disk of the rotor. Figures 4.9 and 4.10 show the normalized orbits and radial displacements at both magnetic bearings. Initially, the first retainer bearing experiences contact for a short period of 0.2 cycles before it changes to a non-contact condition and then contact occurs again within approximately less than a half a cycle when the second retainer bearing comes into contact. The multiple contact state lasts approximately for about 3.0 cycles followed by various combinations of contact phases for about 2.5 cycles. The out of balance was removed at the 10^{th} synchronous cycle. The contact forces and system state in figure 4.11 shows multiple contact and single contacts at the first and the second bearing before rotor recovery. The contact force levels predicted by using constraint Lagrangian equations were between 6 kN and 2 kN at the first and second retainer bearings locations, respectively. These contact forces are tolerable and the system recovers after removing the added out of balance.

In the second simulation case, the contact was initiated with the introduction of a higher sudden out of balance of 40 gm at the inner disk near the magnetic bearing (MB2) at a rotational speed of 250 rad/s, which is above the first flexural critical speed. Figure 4.12 shows the orbits at both magnetic bearing locations. They clearly display the multiple contact mode of operation. Figure 4.13 shows the operational mode as a function of normalized time. After the introduction of the sudden unbalance disturbance, the first magnetic bearing experiences contact followed by a multiple contacts for about 2 cycles. The second magnetic bearing then comes out of contact for about a half a cycle, and then multiple contact operation resumes. After the removal of the unbalance at the 10^{th} cycle, the rotor stays in multiple contacts about a cycle, and then goes through phases of non-contact and second magnetic bearing only contact before returning to a non-contact case. Figure 4.13 also shows the contact forces at both retainer bearings. The maximum contact force is predicted to be between 5 kN and 4 kN at the first and second magnetic bearing locations, respectively. Again, these forces should be tolerable to the rolling element bearings. In general, the orbits, contact forces and system motion obtained using the constrained Lagrangian approach are in agreement with the observations of other researchers [61, 66].

In the third simulation case, the initial steady state was achieved with a 20 gm unbalance mass applied at both inner disks. The contact occurred at a rotational speed of 90 rad/s with a sudden introduction of large out of balance of 100 gm at both inner disks. Figure 4.14(a) shows the normalized orbits at both retainer bearings. The contact force level predicted by using constrained Lagrangian equations is initially less than 8 kN and 4 kN at MB1 and MB2 retainer bearings

locations, respectively. They settle to a value less than 4 kN and 6 kN at MB1 and MB2 retainer bearings locations, respectively as shown in figure 4.14(b). The contact forces oscillate highly during the contact periods, this may cause rotor deformation and high frequency stress in real-time applications. The repeated occurrence of these forces on the rotor may initiate breakage or result in fatigue. It is imperative then to design a controller to reduce the contact forces before fully recovering the rotor position to normal operation. The rotor radial displacements at both magnetic bearings are shown in figure 4.14(c). Figure 4.14(d) shows the system state such that the rotor exhibits all possible contact cases during the first synchronous cycle after the initial contact before settling to the multiple contact case.

4.4 Experimental Verification of the Constrained Lagrangian Modelling Technique

An experimental study was carried out to investigate the rotor orbits when in contact with retainer bearings. The rotor considered in this research is flexible and was run within the speed range 0-30 Hz. Under PID control, critical speeds were measured experimentally at 10 Hz, 17 Hz, and 28 Hz. The rotor displacements were measured relative to the base frame with four pairs of eddy current displacement transducers. At each transducer location, a precision stainless steel collar is mounted on the shaft to minimise the measurement errors due to material imperfection.

A sudden synchronous force was applied through the magnetic bearings. Figure 4.15(a) shows the orbits at both magnetic bearing locations at the running speed of 14.3 Hz (90 rad/s) when 700 N (equivalent to 86.42 gm of unbalance) is applied through the non-driven end magnetic bearing. The shaft is in contact with the retainer bearing at the non-driven end magnetic bearing (MB1). The initial response before the contact is due to unknown unbalance inherent in the flexible rotor. The radial displacement of the magnetic bearing location under contact, as shown in figure 4.15(b), reaches the clearance limit and then recovers after the removal of the additional synchronous force introduced through MB1. The experimental results are comparable with the simulation results obtained by the constrained Lagrangian dynamic modelling in figures 4.5 and 4.6. The contact forces are not measured with the current experimental setup.

Figures 4.16 and 4.17 show the rotor orbit and radial rotor displacements at the running speed of 14.3 Hz (90 rad/s), when sudden synchronous forces were applied through both magnetic bearings; 650 N (equivalent to 80.25 gm unbalance) from the first magnetic bearing (MB1) and 801.9 N (equivalent to 99 gm unbalance) from the other (MB2). The results show multiple contacts after the initial contact occurring at the first magnetic bearing (MB1). The rotor can be recovered from the contact mode by the removal of the synchronous forces. The orbit and redial displacements results are in agreement with the simulation results obtained at rotational speed of 90 rad/s as shown in figure 4.14.

The slight offset between the recorded orbit and the clearance limit is mainly due to the transducers non-collocation and rotor flexibility. Thus, sensors measurements do not represent the exact magnetic bearing location. Other sources of errors in measurements are due to noise and rotor misalignment.

4.5 Lagrangian Approach for Backward Whirl

4.5.1 Backward Whirl and Rolling Motion Modelling

The friction force acts along the s axis at the point of contact, and is in opposite direction to the relative velocity of the shaft v as given in equation (4.11). If the friction coefficient between the spinning rotor and the retainer bearing is high, this may cause a backward whirl, i.e. $\dot{\vartheta} < 0$. If the relative velocity reduces to zero, then stiction will cause the rotor to experience a rolling motion inside the retainer bearing. In the rolling mode, the whirling speed is

$$\dot{\vartheta} = -\left(\frac{R_s}{C_r}\right)\Omega \tag{4.30}$$

In the experimental system considered here, the rotor radius at the magnetic bearing locations is 0.025 m and the clearance is 0.75 mm. This means that the backward whirl speed for the rolling motion will be 33.33 times the rotational speed Ω. It is known that if rotor enters a backward whirl rolling motion, it is destructive, and causes heavy damage. The rotor dynamics and the contact forces under rolling motion can be simulated using the constrained Lagrangian approach, where the rolling motion introduces additional constraint equation for

a contact at the k^{th} nodal plane as follows:

$$v_k = \dot{\vartheta} + \frac{R_s}{C_r}\Omega = 0 \tag{4.31}$$

This can be written in terms of the generalized coordinates.

$$v_k = \frac{R_s}{C_r}\Omega - \frac{y_k}{C_r^2}\dot{x}_k + \frac{x_k}{C_r^2}\dot{y}_k = 0 \tag{4.32}$$

This is a non-holonomic constraint equation, and can be incorporated into system equations through another Lagrange multiplier λ_v. For a single contact case, the new Jacobian matrix and Lagrange multiplier vector in equation (4.14) are as follows:

$$\begin{aligned} \mathbf{J} &= \begin{bmatrix} 0 \cdots & -2x_k & 0 \cdots & -2y_k & \cdots 0 \\ 0 \cdots & -y_k/C_r^2 & 0 \cdots & x_k/C_r^2 & \cdots 0 \end{bmatrix} \\ \lambda &= \begin{bmatrix} \lambda_k \\ \lambda_v \end{bmatrix} \end{aligned} \tag{4.33}$$

Differentiating υ_k with respect to time gives:

$$\dot{\upsilon}_k = -\frac{y_k}{C_r^2}\ddot{x}_k + \frac{x_k}{C_r^2}\ddot{y}_k + \frac{2\,x_k\,y_k}{C_r^4}\dot{x}_k^2 - \frac{2\,x_k\,y_k}{C_r^4}\dot{y}_k^2 = 0 \tag{4.34}$$

thus

$$\mathbf{D} = \begin{bmatrix} 2\,\dot{x}_k^2 + 2\,\dot{y}_k^2 \\ (-2\,x_k\,y_k/C_r^4)\;\dot{x}_k^2 + (2\,x_k\,y_k/C_r^4)\;\dot{y}_k^2 \end{bmatrix}$$

The re-setting of initial conditions when entering the backward whirl rolling motion is required. The initial conditions should satisfy equation (4.16) and equation (4.32). Solving these two equations gives the following initial condition for the rolling motion:

$$\dot{x}_k(0^+) = \frac{R_s}{C_r}\Omega\,y_k(0^-) \quad , \quad \dot{y}_k(0^+) = -\frac{R_s}{C_r}\Omega\,x_k(0^-) \tag{4.35}$$

where $x_k(0^-)$ and $y_k(0^-)$ are the displacement at the point of entering the rolling motion. The contact forces can be calculated from the two Lagrange multipliers. In this case there will be two constraint forces; one from λ_k in the r (normal) direction F_n, and the other from λ_υ in the s (tangential) direction F_t at the point of contact. As before the direction of F_n will determine whether the rotor comes out of contact. The tangential constraint force can be used to decide whether the rotor returns to sliding mode. If F_t becomes greater than the static stiction

force, then the constraint corresponding to the rolling mode can be released (i.e. $\lambda_v = 0$). However, as it will be shown in the simulation results in the next section, entering the rolling mode would generate such high contact forces, that it would be unrealistic to expect the retainer bearing to survive the experience, and the system must be shut down immediately.

4.5.2 Backward Whirl and Rolling Simulation Results

The friction coefficient for a given material could vary significantly during operation [91], and with other factors such as heat and surface damage. Ashby and Johns [92] have reported that the coefficient of friction for clean metal in air could be as high as 2.

Simulations were carried out at Ω = 90 rad/s with a friction coefficient of μ = 2 for demonstration purposes. Figure 4.18(a) shows the whirl speed $\dot{\vartheta}$ after the introduction of a sudden unbalance of 44 gm at the disk at the non-driven end at the 5^{th} cycle. After a brief initial recovery from the backward whirl (negative $\dot{\vartheta}$) at 5.1 synchronous cycle as shown in figure 4.18(b), the rotor enters into unrecoverable backward whirl motion at 5.257 cycles (figures 4.18(c) and 4.18(d)) where the whirl speed reaches the value of -3,000 rad/s (i.e. zero relative velocity in accordance with equation (4.30) at 5.264 cycles in figure 4.18(c). The time between the initial contact and entering the backward rolling mode is too small for any controller to act.

The previous simulation shows that high friction coefficient can initiate a backward whirl and zero relative velocity, i.e. the rolling motion, can be obtained in a very short time period. Figure 4.19(a) shows the orbits at both magnetic bearing locations when the rotor enters a rolling motion at the location of first magnetic bearing. The resulting normal contact forces, shown in figure 4.19(b), reach an extremely high level of 100 kN.

The extremely high contact forces demonstrate the most destructive motion to

a rotor/bearing system. Under this condition, the rotor is in continuous contact with the retainer bearing slipping on its inner surface. During backward whirl, the contact and friction forces at the contact point may damage the contact surface and impose demands for excessive input power and control force. The rotor is under large deformation and stress, which will easily initiate the fatigue damage of the shaft and/or cause system failure.

In the second simulation case of rolling motion, the initial steady state response was achieved with 5 gm unbalance mass. The contact occurred at rotational speed of $\Omega = 220$ rad/s with 30 gm of out of balance was introduced at the non-driven end disk at the start of the 5^{th} cycle to initiate a contact. Figure 4.20(a) shows the whirl speed $\dot{\vartheta}$. The rotor enters into unrecoverable backward whirl motion at about 5.327 cycles as shown in figure 4.20(b), where the whirl speed reaches the value of -7350 rad/s (i.e. zero relative velocity) at about 5.329 cycles. The time between the initial contact and entering the backward whirl mode is approximately 3 ms, which is too short for any controller to recover rotor position from a destructive contact mode. Figure 4.21(a) shows the orbits at both retainer bearing locations when the rotor enters a rolling motion at the first retainer bearing. The resulting normal contact forces are shown in figure 4.21(b), which reach extremely high levels of 1300 kN and 650 kN at the first and second magnetic bearings, respectively. The rotor does not return to a non-contact state even after removing the additional out-of-balance at the start of the 10^{th} cycle.

This force level confirms that backward whirl roll motion under contact would be destructive with no possibility to recover the rotor position. Although the

additional out-of-balance is removed at the 10^{th} cycle as in previous cases, the rotor is trapped in this destructive state and does not return to the initial non-contact state. The only action is to shut down the system, but damage to the retainer bearing and perhaps to the rotor would be inevitable. Numerous simulation runs at various speeds and sudden unbalance changes showed that the destructive backward whirl rolling motion could occur at high friction coefficient cases. Therefore, backward whirl is unlikely to occur when rolling element bearings are used as retainer bearings. However, with bush bearings, the friction coefficient may increase due to heat and impact damage and cause the backward rolling motion.

In the current experimental setup, the backward scenario can not be demonstrated and hence this destructive mode was not considered in the subsequent control work.

4.6 Summary

A computationally efficient computer model of a flexible rotor/magnetic bearing system when the rotor is in contact with the retainer bearings has been developed. The method does not require detailed modelling of the contact forces. Hence it eliminates the problem with conventional methods of modelling contact forces as non-linear functions of rotor penetration into the bearing inner surface at the contact point. It was also shown that it is also possible to predict destructive backward whirl motion. The suggested modelling technique can detect the rolling mode by the introduction of another constraint and simulates it through an additional Lagrange multiplier. Simulation and experimental work shows good agreement.

Computational efficiency of the model was enhanced by implementing a model reduction technique when modelling the flexible rotor. It has been shown that it is best to use as many nodal planes as necessary in the finite element modelling for a required accuracy, and then apply the suggested model reduction technique (MSDC).

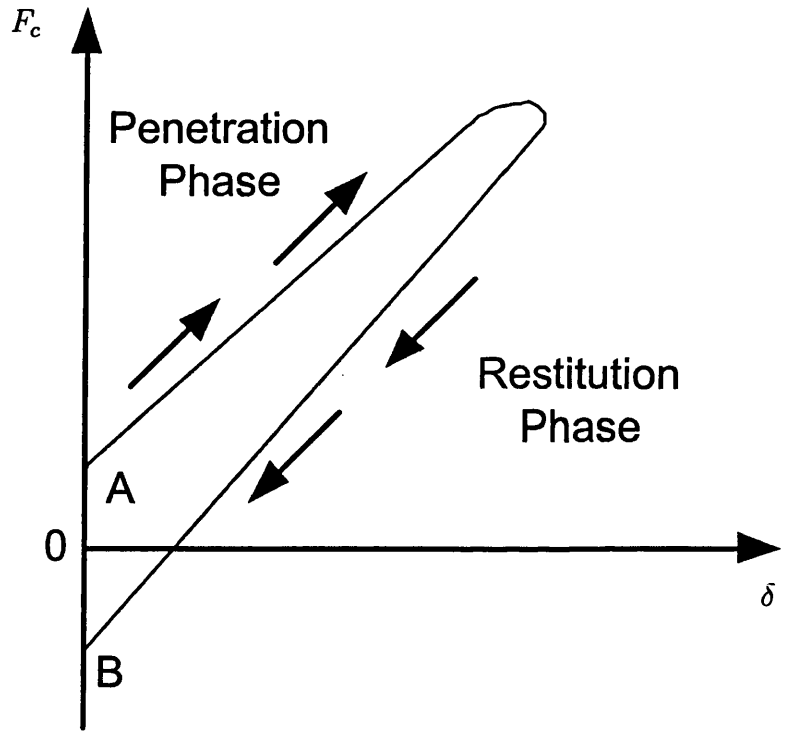

Figure 4.1: Force - displacement characteristics of stiffness-damping model

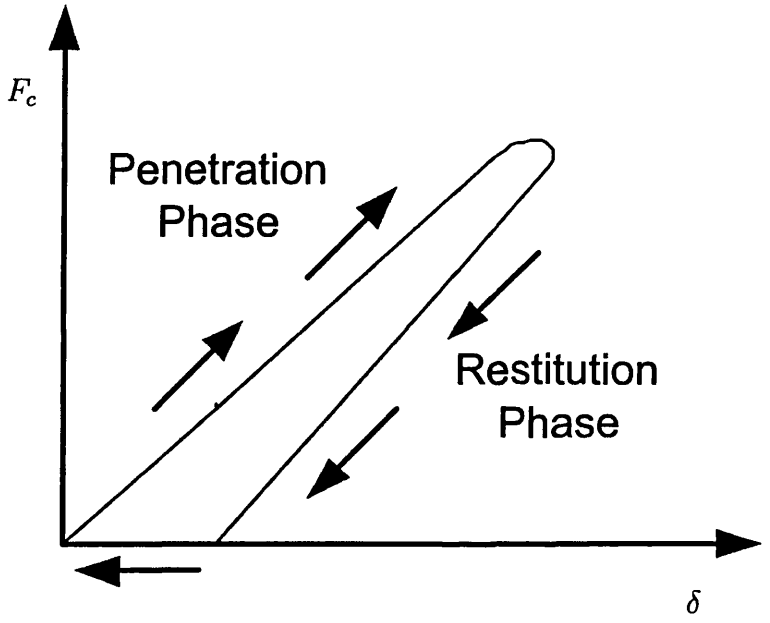

Figure 4.2: Force - displacement characteristics of stiffness-damping model with switching function

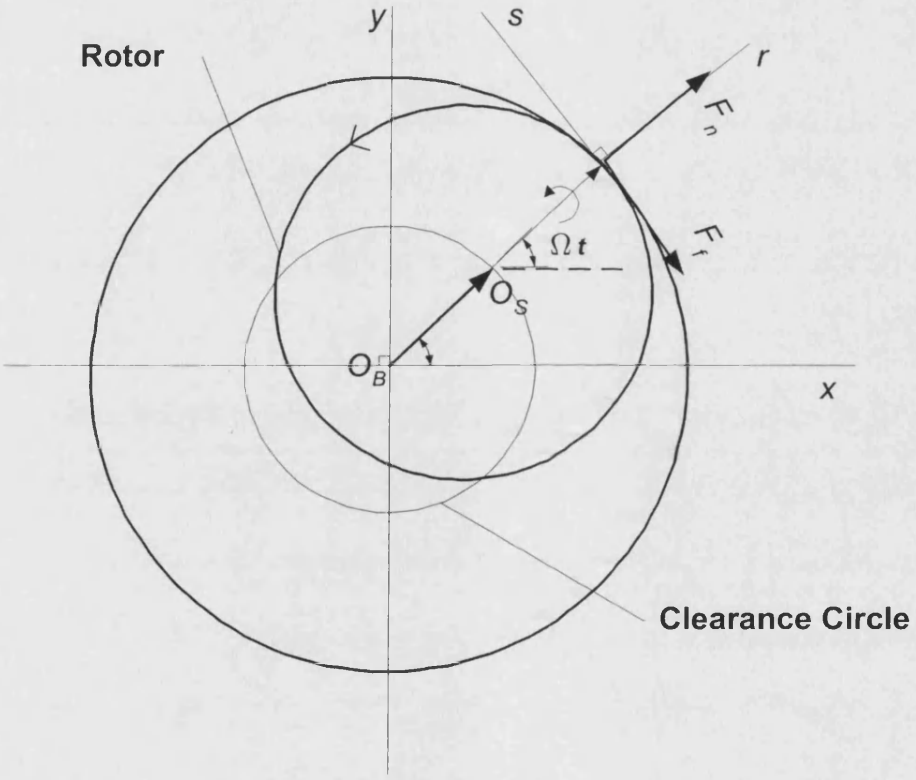

Figure 4.3: Axes system at a contact node location

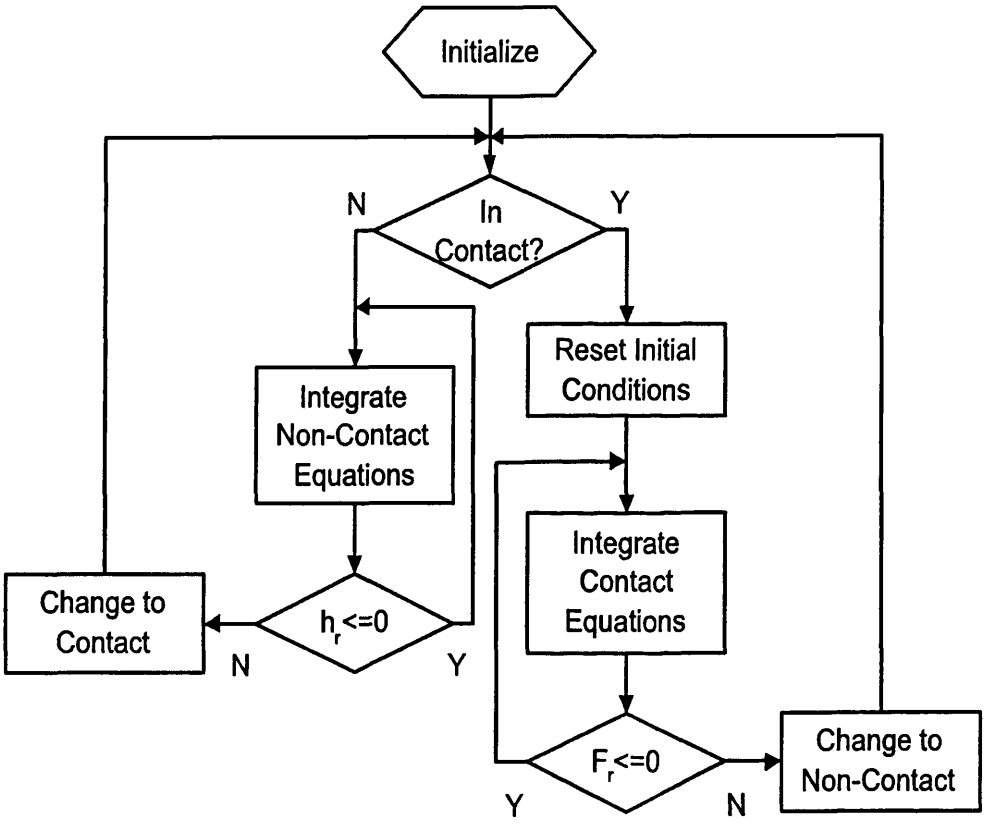

Figure 4.4: Flowchart of the Lagrangian model switching algorithm when simulating single contact

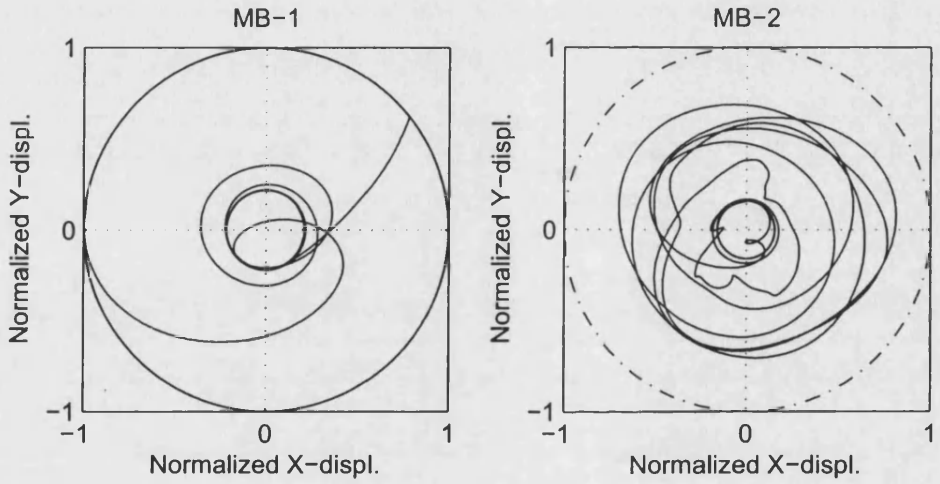

Figure 4.5: Simulations orbits at both magnetic bearings at $\Omega = 90$ rad/s demonstrating a single contact at MB1, sold line: orbit trajectory and dash-dot line: retainer bearing clearance

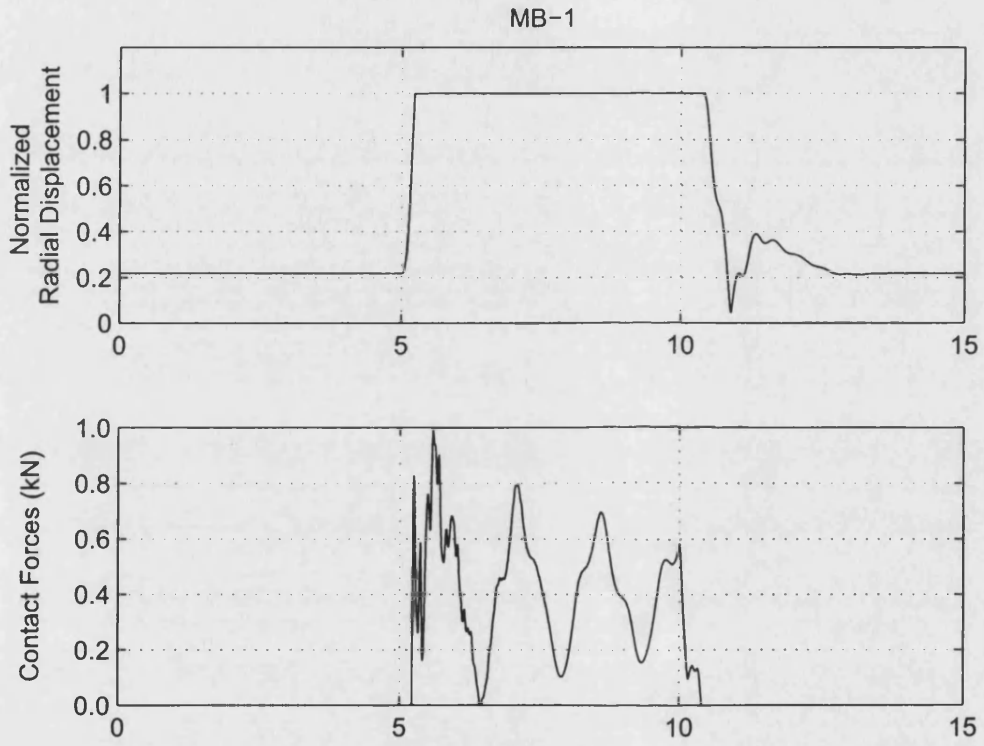

Figure 4.6: Simulations of radial displacement and contact force at MB1 at $\Omega =$ 90 rad/s following a sudden increase in out-of-balance of 44 gm at the non-driven end disk

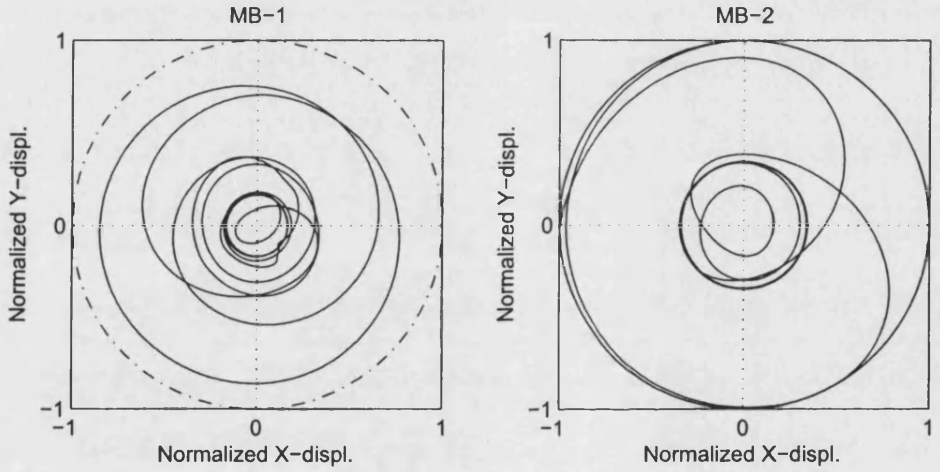

Figure 4.7: Simulations orbits at both magnetic bearings at $\Omega = 120$ rad/s demonstrating a single contact at MB2, sold line: orbit trajectory and dash-dot line: retainer bearing clearance

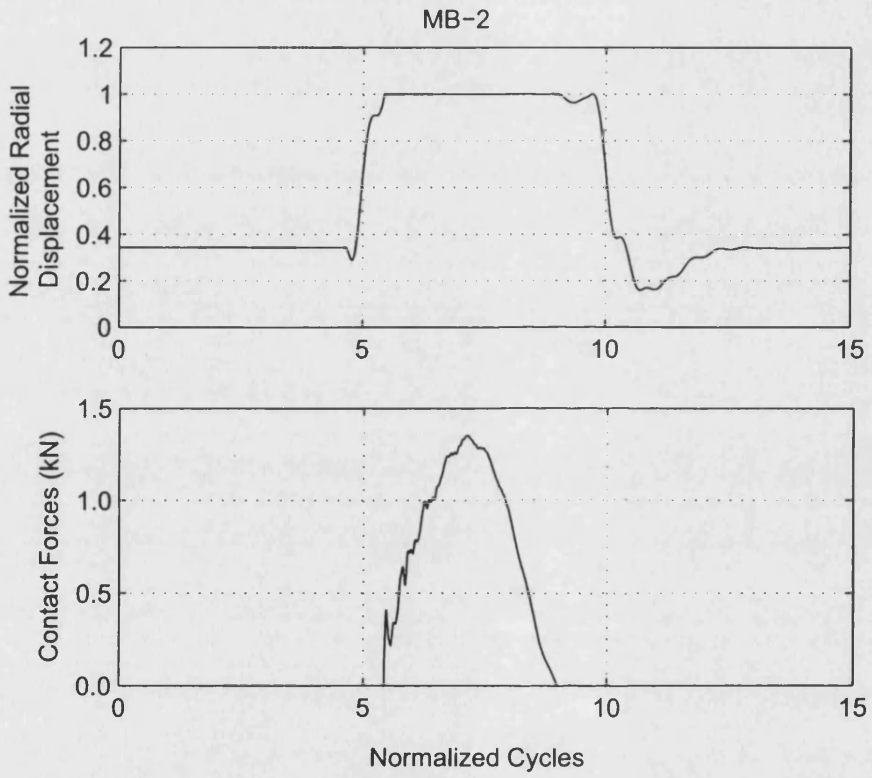

Figure 4.8: Simulations radial displacement and contact force at $\Omega = 120$ rad/s demonstrating a single contact at MB2 following a sudden increase in out-of-balance of 12 gm at middle disk next to the MB2

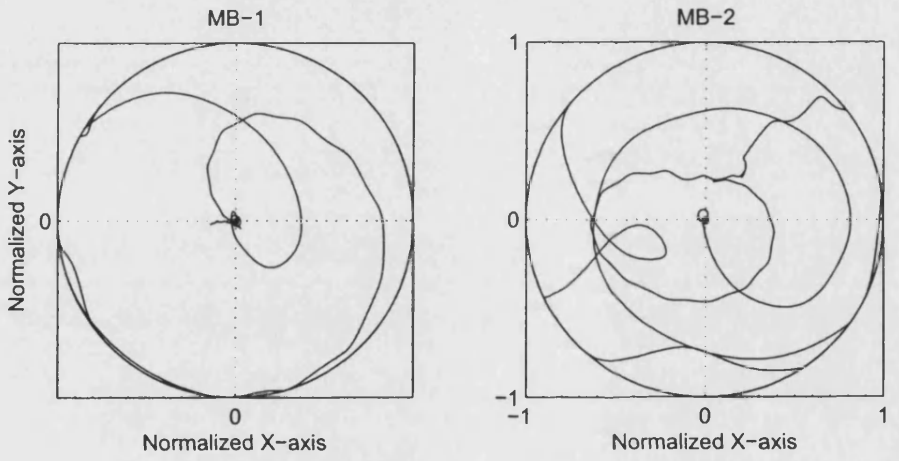

Figure 4.9: Rotor orbits simulation at 260 rad/s for multiple contacts

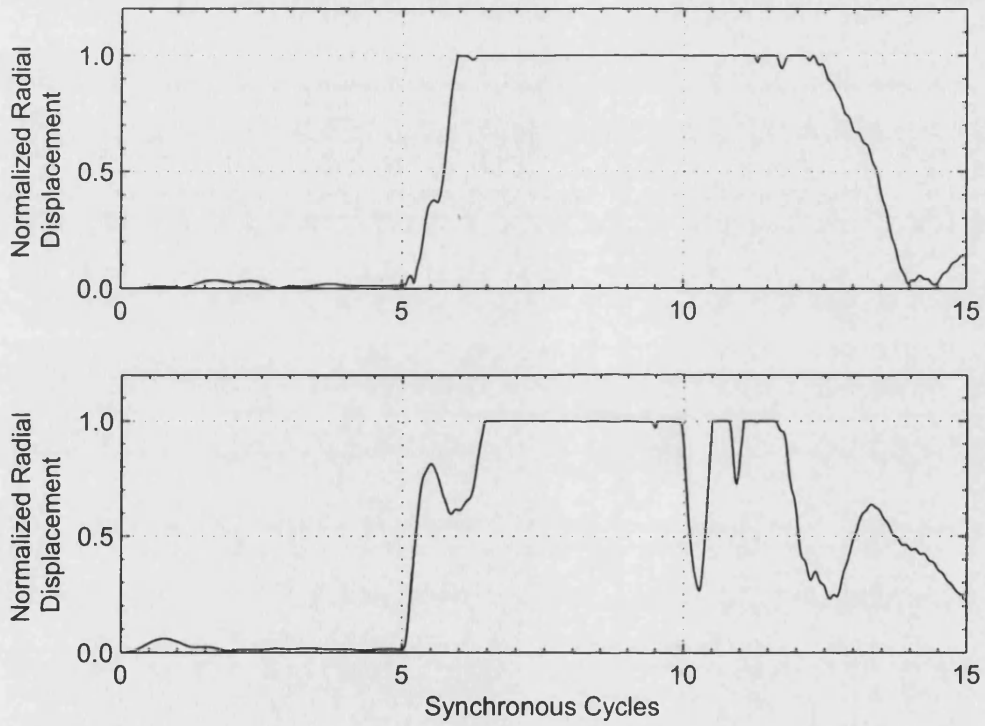

Figure 4.10: Rotor radial displacements simulation at 260 rad/s for multiple contacts initiated by a sudden unbalance of 25 gm

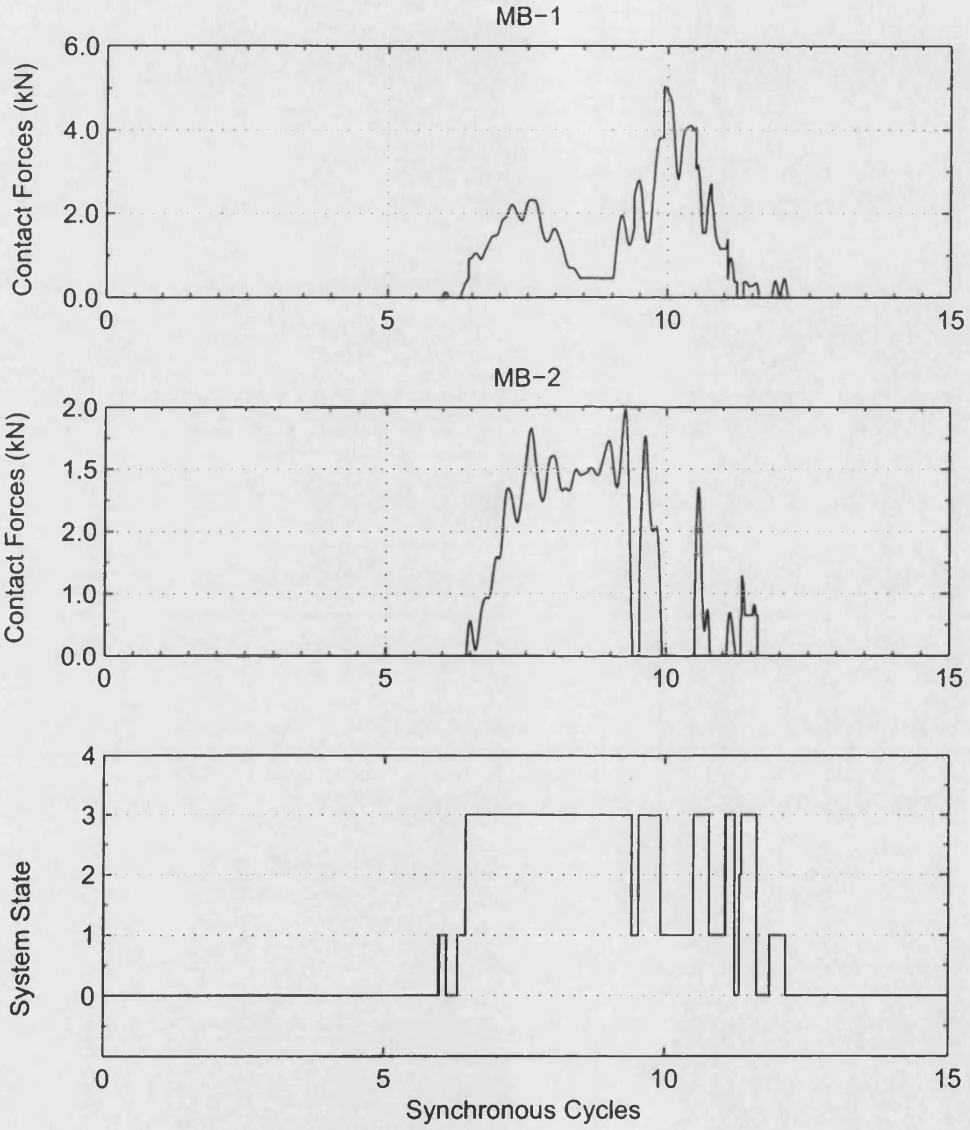

Figure 4.11: Contact forces and system state simulation results at 260 rad/s for multiple contacts initiated by a sudden unbalance of 25 gm

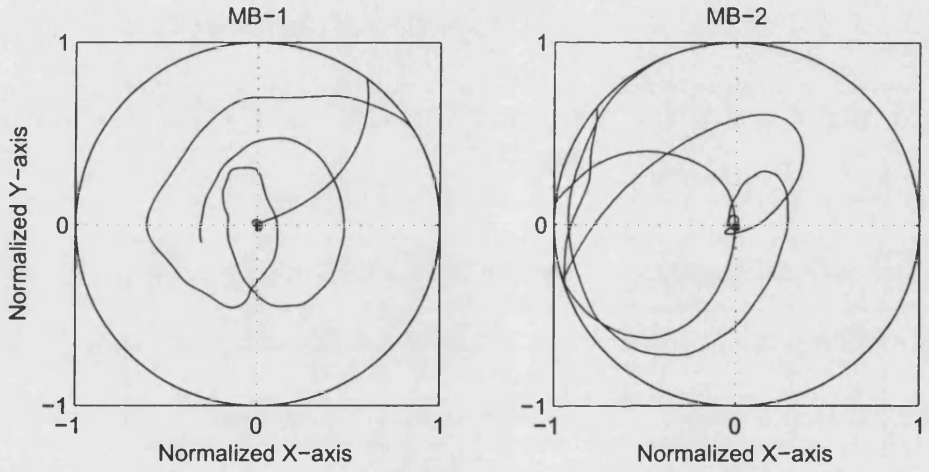

Figure 4.12: Orbits at $\Omega = 250$ rad/s for a multiple contact case initiated by a sudden unbalance of 40 gm at the inner non-driven end disk

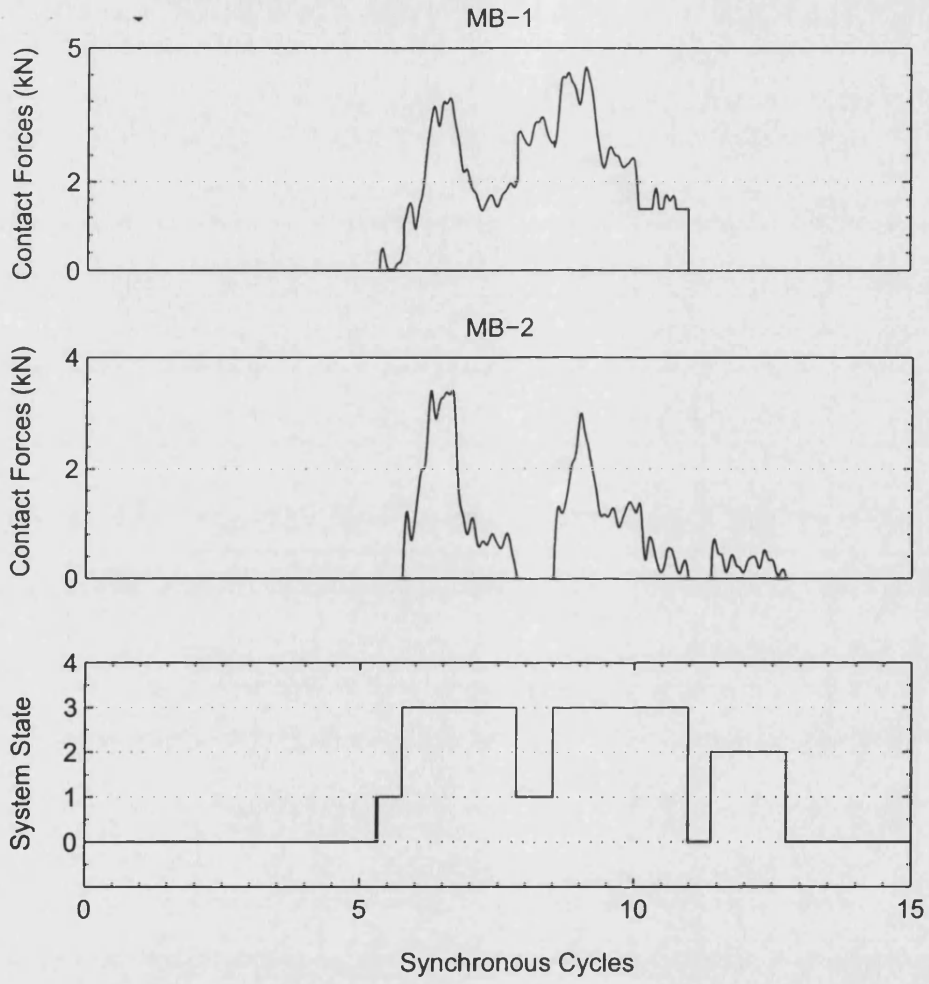

Figure 4.13: Contact forces and system states at $\Omega = 250$ rad/s for a multiple contact case

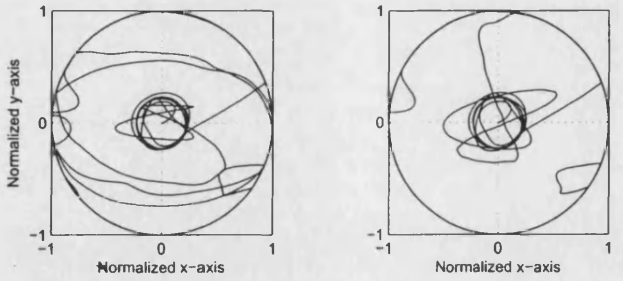

(a) Normalized rotor orbits

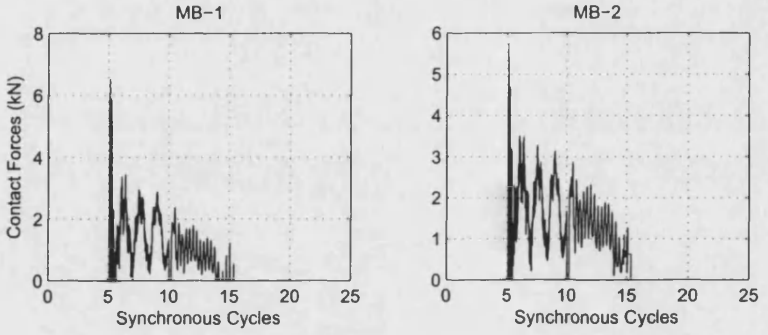

(b) Contact forces

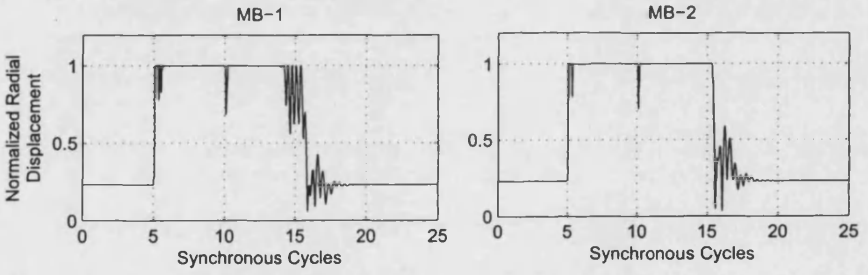

(c) Normalized radial displacements

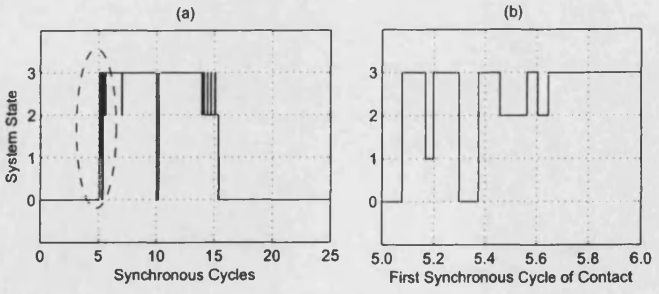

(d) System states

Figure 4.14: Simulation at 90 rad/s for multiple contacts initiated by a sudden unbalance of 100 gm at both inner disks

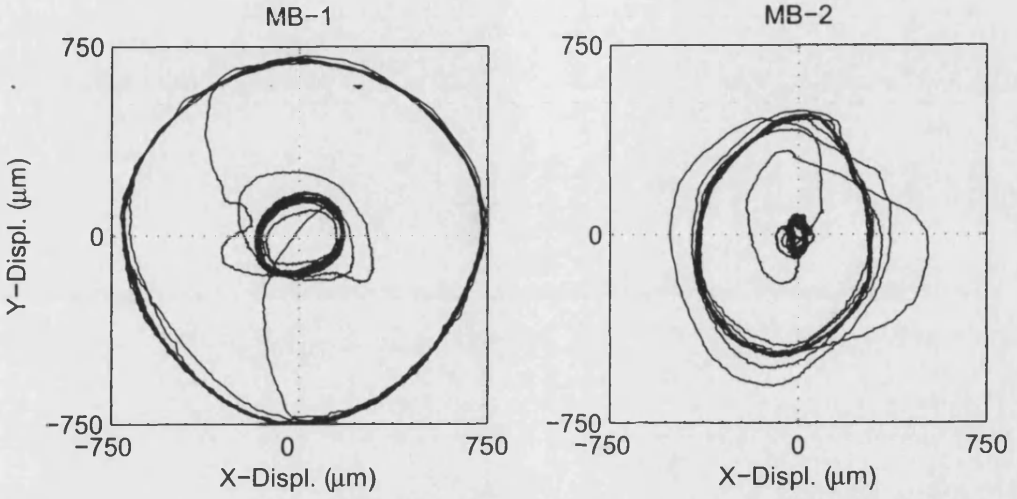

(a) Orbits

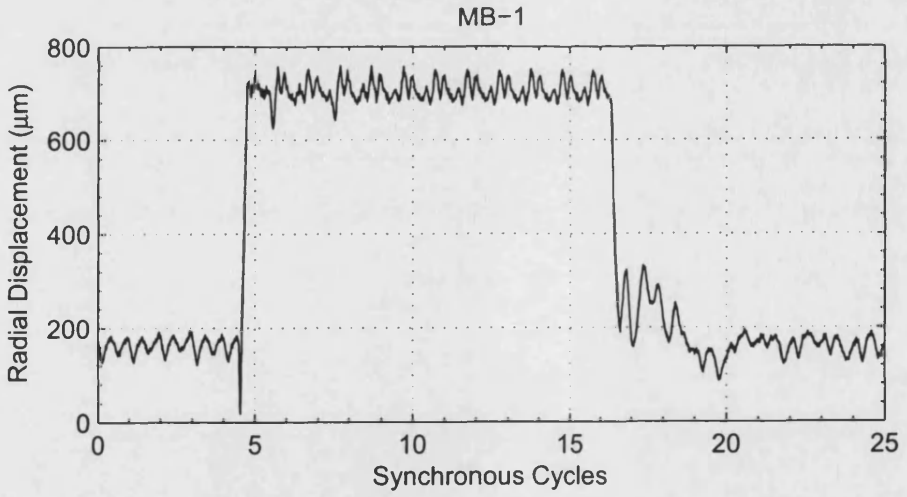

(b) Radial displacement

Figure 4.15: Experimental results showing a single contact at the MB1 at $\Omega = 90$ rad/s

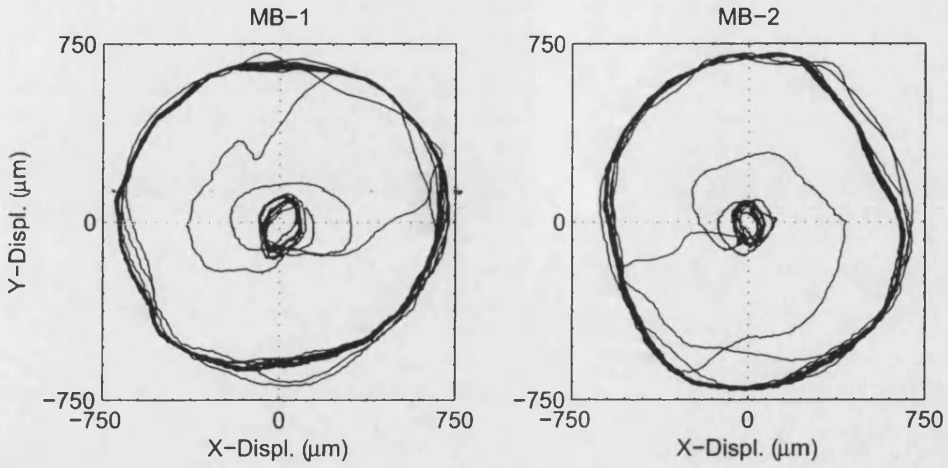

Figure 4.16: Experimental Orbits showing multiple contacts at $\Omega = 90$ rad/s

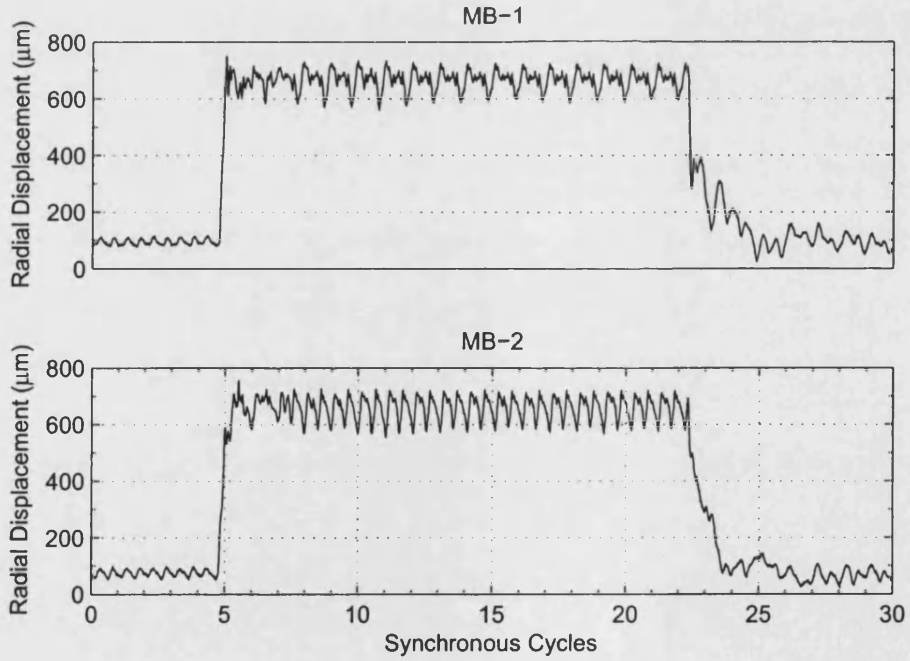

Figure 4.17: Experimental radial displacements showing multiple contacts at $\Omega = 90$ rad/s

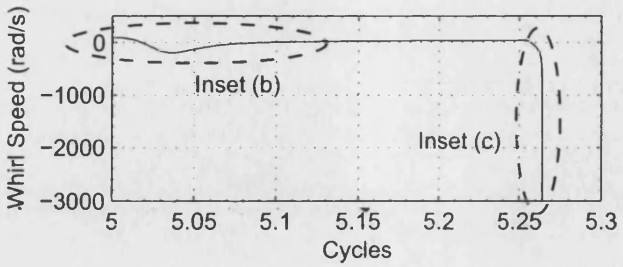

(a) Whirl speed after contact

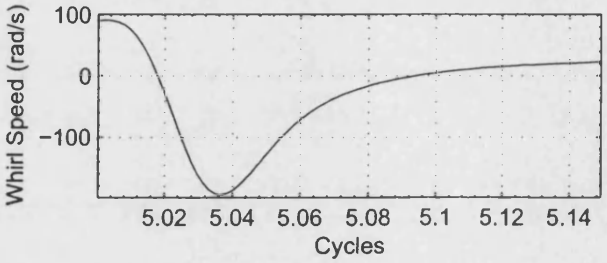

(b) Initial backward whirl

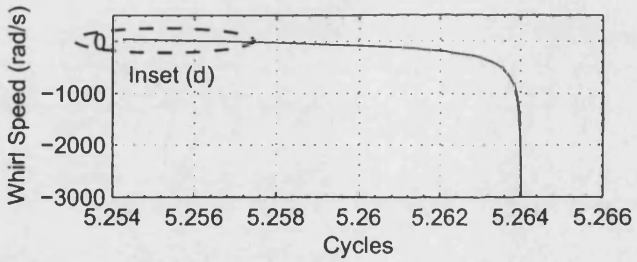

(c) Approaching to zero relative speed (i.e. whirl speed=-3000 rad/s)

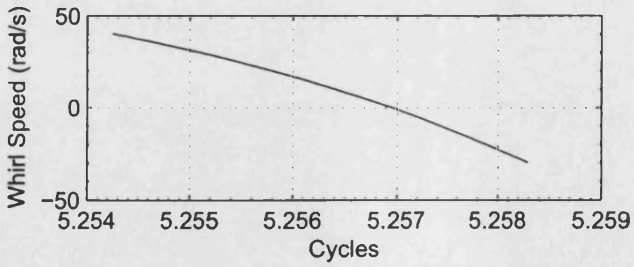

(d) Entering unrecoverable backward whirl

Figure 4.18: Whirl speed at $\Omega = 90$ rad/s showing backward whirl with a friction coefficient of $\mu = 2$

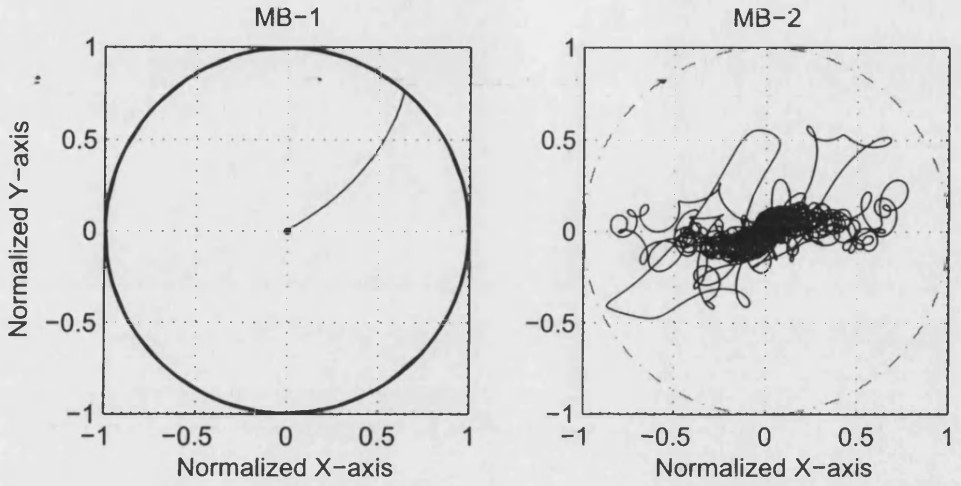

(a) Orbits

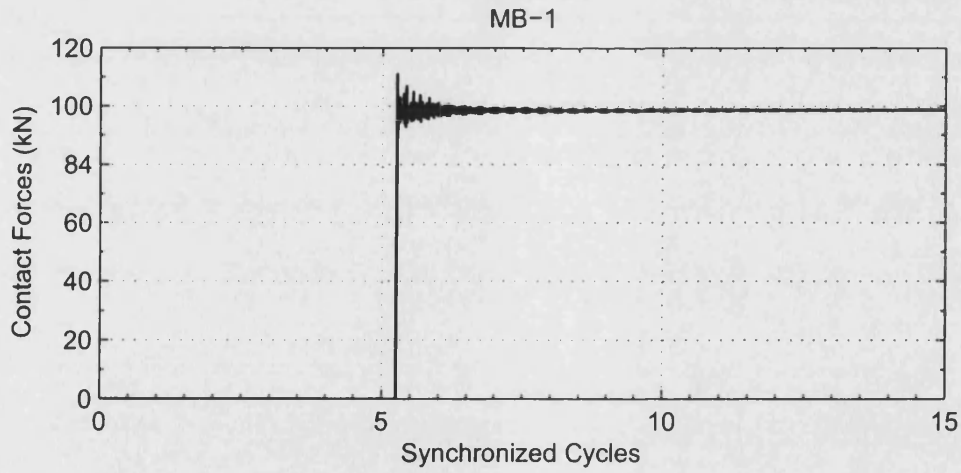

(b) Contact force

Figure 4.19: Simulation results for a backward whirl rolling motion at $\Omega = 90$ rad/s

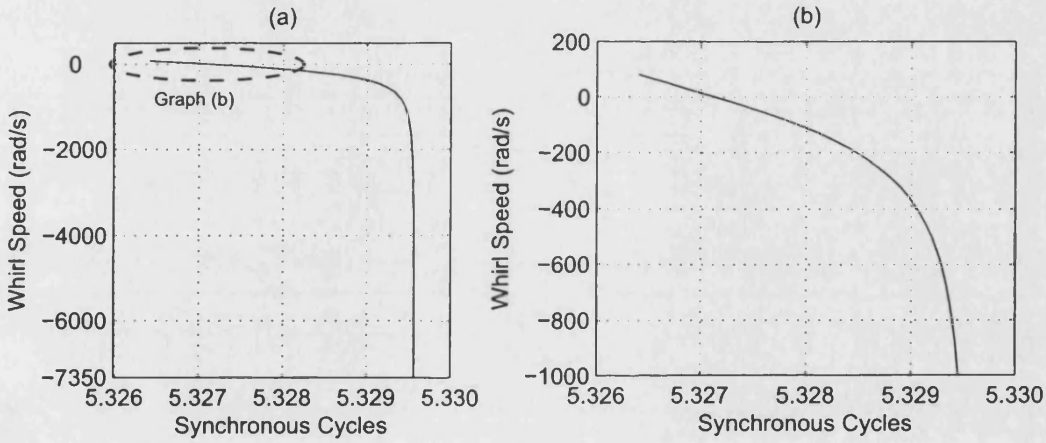

Figure 4.20: Whirl speed at $\Omega = 220$rad/s showing backward whirl leading to a rolling motion

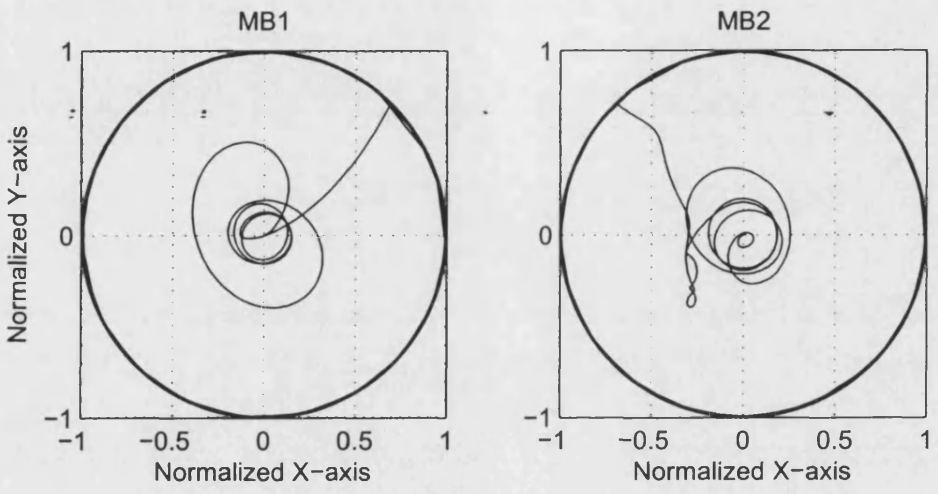

(a) Orbits

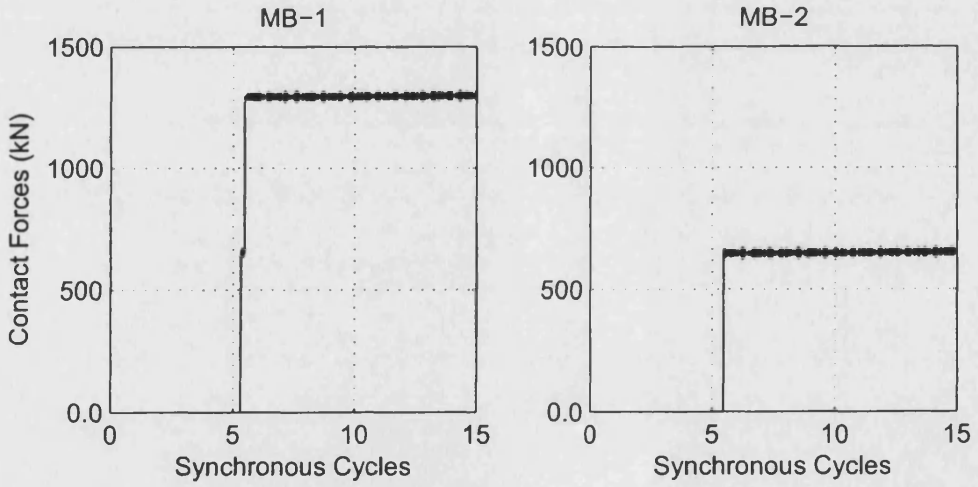

(b) Contact force

Figure 4.21: Normalized orbits and contact forces for backward whirl rolling motion

Chapter 5

ROLAC Control Algorithm Design

5.1 Passive Local Closed Loop Control

The main objective of any control design is to ensure stability and keep the rotor at the bearing central position. The magnetic bearing forces are attractive only and decrease dramatically with increasing airgap. Therefore, they are unstable with an inherit negative stiffness. It is common practice, as shown in previous chapter, to incorporate local decentralized Proportional-Integral-Derivative (PID) control law to achieve stability and dynamic performance, whereby a con-

trol current is expressed as:

$$I_c = -\left[(k_p\, x + k_d\, \dot{x} + k_i \int x\, dt\right] \tag{5.1}$$

The proportional component includes compensation for the negative stiffness K_s to achieve a net positive bearing stiffness K_b. The differential component provides damping. An additional integral term is to ensure zero static position of the rotor. The integration gain K_i is kept small and can be neglected in the dynamic analysis. The bearing stiffness K_p and the damping K_d are the effective parameters for the controller. Substituting equation (5.1) into equation (2.7) gives the following dynamic force applied along one of the axis of an active magnetic bearing:

$$F = -(k_p k_i - K_s)x - k_d K_i \dot{x} \tag{5.2}$$

$$F = -K_b x - C_b \dot{x} \tag{5.3}$$

K_b and C_b are the effective stiffness and damping coefficients of the magnetic bearing. The PID parameters for a desired K_b and C_b can be obtained as follows:

$$k_p = \frac{K_b + K_s}{K_i}, \qquad k_d = \frac{C_b}{K_i} \tag{5.4}$$

5.2 Open Loop Adaptive Control

An open-loop adaptive control algorithm was developed in [37] to minimise the sum of squares of measured vibration components along the rotor. The rotor response measurements can be given different weights to signify the importance of particular planes. This is a frequency domain method providing a single (synchronous) or multi-frequency control force. Statistical data can be used to build fault detection and monitoring capabilities [39]. The frequency response of the rotor with linear magnetic bearing characteristics can be written as

$$\left[-\mathbf{M}\omega^2 + \mathbf{K} + j\omega(\mathbf{C} + \Omega\mathbf{G})\right] \mathbf{Q}(j\omega) = \left[\mathbf{B_d}\mathbf{F_d}(j\omega) + \mathbf{B_u}\mathbf{U}(j\omega)\right] \tag{5.5}$$

or

$$\begin{aligned} \mathbf{Q}(j\omega) &= \left[-\mathbf{M}\omega^2 + \mathbf{K} + j\omega(\mathbf{C} + \Omega\mathbf{G})\right]^{-1} \left[\mathbf{B_d}\mathbf{F_d}(j\omega) + \mathbf{B_u}\mathbf{U}(j\omega)\right] \\ &= \mathbf{\Delta}(j\omega) \times \left[\mathbf{B_d}\mathbf{F_d}(j\omega) + \mathbf{B_u}\mathbf{U}(j\omega)\right] \end{aligned} \tag{5.6}$$

$\mathbf{\Delta}(j\omega)$ is the receptance matrix of order $2k \times 2k$ and $\mathbf{F_d}(j\omega)$ and $\mathbf{U}(j\omega)$ are of order $2k$ and consist of components due to out of balance and control forces applied through the magnetic bearings, respectively. If measured response vector

is of the form:

$$\mathbf{Q}_m(j\omega) = \mathbf{C_m}\mathbf{Q}(j\omega) \tag{5.7}$$

where $\mathbf{C_m}$ is the measurement coefficient matrix of size $n \times 2k$, then the predicted measured rotor response with respect to changes in control input $\delta\mathbf{U}(j\omega)$ can be written as follows:

$$\hat{\mathbf{Q}}_m(j\omega) = \mathbf{Q}_m(j\omega) - \mathbf{R}(j\omega)\delta\mathbf{U}(j\omega) \tag{5.8}$$

With a control force vector of dimension l, the complex partial receptance matrix $\mathbf{R}(j\omega)$ is of dimension $n \times l$ containing the columns of $\mathbf{\Delta}(j\omega)$ corresponding to l control force variables, and rows corresponding to n measurement axes. The aim is to determine the optimum change in the control force to minimise the sum of the squares of the predicted response as follows:

$$\delta\hat{\mathbf{U}}(j\omega) = \mathbf{H}(j\omega)\mathbf{Q}_m(j\omega) \tag{5.9}$$

where $\mathbf{H}(j\omega)$ can be achieved by a least-square estimator as:

$$\mathbf{H}(j\omega) = \left[\mathbf{R}^T(j\omega)\mathbf{R}(j\omega)\right]^{-1}\mathbf{R}^T(j\omega) \tag{5.10}$$

The matrix $\mathbf{H}(j\omega)$ is a function of the system dynamics and does not depend on external excitation. The open loop control matrix $\mathbf{H}(j\omega)$ can be determined either from the system model, or measured experimentally. The ability to estimate the complex partial receptance matrix $\mathbf{R}(j\omega)$ and hence calculate the $\mathbf{H}(j\omega)$ matrix experimentally makes the OLAC controller possible to use in systems where there are no reliable mathematical models.

For controlling the synchronous vibrations, the optimum force is an open-loop sine wave, of which the amplitude and phase is adjusted in accordance with equation (5.8). There is no need to recalculate the optimum force unless there is a change in the system response. If there are multiple frequency excitations, then parallel controllers can be designed for each frequency component.

5.3 The Estimation of the Partial Receptance Matrix

Although the estimation of the complex partial receptance matrix can be achieved by a time-domain method, measurement, noise and the errors due to transformation from continuous to discrete time in the numerical process can cause significant errors in the estimated coefficients. These problems can be avoided if the estimation is undertaken in the frequency domain and the Fourier transform is used.

Stanway and Burrows [93], proposed a series of experiments to establish the

practicality of injecting a signal that contains sufficient harmonics to excite rotor modes. Further research work was conducted to compare two multi-frequency test signals, namely, Pseudo Random Binary Sequence (PRBS) and Schroeder Phased Harmonic Signal (SPHS) [94]. It is possible to synthesise a SPHS signal $u(t)$ with any desired spectrum by combing a series of harmonic waves as follows:

$$u(t) = \sum_{i=1}^{N_b} a_i \cos\left(\frac{2\pi i t}{T} + \gamma_i\right) \tag{5.11}$$

where the a_i is the amplitude of the i^{th} harmonic, that can be selected freely to obtained a balanced response, is related to power as follows:

$$a_i = \sqrt{\frac{P_i}{2}} \tag{5.12}$$

and the phase of each frequency component is as follow [95]:

$$\gamma_i = \gamma_{i-1} - 2\pi \sum_{m=1}^{i-1} P_m \quad , \qquad i = 1, 2, \ldots, N \tag{5.13}$$

It is possible to generate a low-peak factor periodic signal having any user specified power spectrum P_i , $i = 1, \ldots, N$ where P_i is the ratio of the power at

$w = iw_o$ to the total power:

$$\sum_{i=1}^{N} P_i = 1 \tag{5.14}$$

The key attraction of a SPHS is that it is synthesised from harmonic components, thus any arbitrary signal spectrum can be generated with any desired frequency resolution [96]. It is also a low-peak-factor signal which avoids system saturation and non-linear regimes. This flexible feature of the SPHS in selecting its characteristics is significant when it is desired to attenuate the excitation of certain frequencies in a complex system. In addition, a SPHS can be easily implemented using a digital computer for on-line applications.

The need to apply appropriate external test signals is a fundamental requirement for any estimation process [97]. The out-of-balance excitation in a magnetic bearing system is a synchronous sinusoidal signal, but the measured response may include multiple or sub-harmonic components of the running speed. A single frequency test control force at synchronous frequency ω_o can be set as follows:

$$\delta u(j\omega_o) = A(\omega_o)\cos(\omega_o t + \psi) \tag{5.15}$$

where ω_o is the fundamental synchronous frequency.

The estimation of the $\mathbf{H}(j\omega_o)$ matrix involves the estimation of the partial receptance matrix $\mathbf{R}(j\omega_o)$. A synchronous test control force as in equation (5.15)

can be added at each control force channel one at a time, and the changes in the frequency response of measurements with respect to a unit test force can be calculated to determine the corresponding columns in the $\mathbf{R}(j\omega_o)$ matrix:

$$\mathbf{R}_i(j\omega_o) = \frac{\delta \mathbf{Q}_m(j\omega_o)}{\delta u_i(j\omega_o)} \quad , \qquad i = 1, 2, 3, 4 \tag{5.16}$$

The partial receptance matrix $\mathbf{R}(j\omega_o)$ is 8×4 and can be written as:

$$\mathbf{R}(j\omega_o) = \left[\begin{array}{cccc} \mathbf{R}_1(j\omega_o) & \mathbf{R}_2(j\omega_o) & \mathbf{R}_3(j\omega_o) & \mathbf{R}_4(j\omega_o) \end{array} \right] \tag{5.17}$$

For a multi-frequency vibration control this procedure has to be repeated by exciting the system at 2Ω, 3Ω etc. Selection of an appropriate test force amplitude $A(j\omega_o)$ is important for the accuracy of the estimation. A large value will violate the linearity assumption and a small value will not cause enough change in the response to be measured with confidence. Also, since the $\mathbf{R}(j\omega_o)$ matrix is frequency dependent, a suitable value of $A(j\omega_o)$ is expected to be frequency dependent. An analysis is carried out to determine suitable values of the test signal amplitude.

Figure 5.1(a) represents the sensitivity of the system response to small changes in control forces in the first magnetic bearing x-axis over the range of the system running speeds. Other axes will have the same trend due to the system symmetry.

The sensitivity function is calculated as follows:

$$S_i(j\omega) = |\mathbf{R}_i(j\omega)| = \sqrt{\mathbf{R}_i^T(j\omega)\mathbf{R}_i(j\omega)} \quad , \qquad i = 1, 2, 3, 4 \tag{5.18}$$

Figure 5.1(a) is piecewise linearized as shown in figure 5.1(b) as follows:

$$S(j\omega) = \begin{cases} 0.25\omega + 2 & 0 \leq \omega \leq 10 \\ -0.2\omega + 6.5 & 10 \leq \omega \leq 30 \\ 0.4 & \omega \geq 30 \end{cases} \tag{5.19}$$

The test control force amplitude is determined using the reciprocal of the linearized determinant of the partial receptance matrix $\mathbf{R}(j\omega)$. This force has to be scaled and limited to a maximum value such that the vibration level caused by the test control force is within acceptable levels. The force amplitude level is a function of the running frequency which was scaled with gain = 220 as shown in figure 5.2. The gain value is selected to achieve approximately 0.1 mm change in the vibration amplitudes at the corresponding local axis.

The partial complex matrix $\mathbf{R}(j\omega)$ does not need to be identified at each run unless there is a structural change in the system, or a structural fault develops. The $\mathbf{H}(j\omega)$ matrix is calculated and stored at certain running speeds at which the $\mathbf{R}(j\omega)$ matrix is estimated. Between the stored speed values the $\mathbf{H}(j\omega)$ are determined using linear interpolation. Experimentally, the performance of the

controller with $\mathbf{H}(j\omega)$, which is calculated between the stored speed values is tested to attenuate the rotor vibration due to inherent out of balance. In the case of experiencing poor performance, more speed values can be considered. This was the case at speeds between 15 Hz and 20 Hz as well as around 30 Hz, which agrees with the simulation results as shown in figure 5.1(a). The trend of the modulus of the matrix $\mathbf{H}(j\omega)$, $|\mathbf{H}(j\omega)|$, as a function of the running frequency is also shown in figure 5.3.

5.4 Recursive Open Loop Adaptive Control

The main disadvantage of the OLAC is that it requires at least one period of steady state response before calculating the optimum synchronous control force after any change in the system frequency response is detected. This may not be fast enough if there is a sudden change of the operating conditions. Therefore, a recursive formulation is introduced here, which updates the control force amplitude and phase at each sampling period. This is achieved by using a recursive Fourier transform. A Fourier transform of measurements $\mathbf{q}_m(t)$ at time t can be written as:

$$\mathbf{Q}_m(j\omega, t) = \mathbf{I}(j\omega, t) - \mathbf{I}(j\omega, t - 2\pi/\omega) \tag{5.20}$$

where the integral $\mathbf{I}(j\omega, t)$ is defined as:

$$\mathbf{I}(j\omega, t) = \frac{\omega}{2\pi} \int_{\tau=0}^{t} \mathbf{q}(\tau)\, e^{-j\omega} d\tau \tag{5.21}$$

A discrete version of equations (5.20) and (5.21) can be used in conjunction with equation (5.9) to update the amplitude and phase of the control force at each sampling instant. Equation (5.9) gives the required change in the control force and therefore an integral action with a gain α is included in the controller. The integral gain must be determined experimentally because it depends on the system dynamics, sampling rate and desired speed of the controller. Thus, ROLAC in the frequency domain is formulated as follows:

$$\hat{\mathbf{U}}(j\omega, t) = \alpha \int \mathbf{H}(j\omega)\mathbf{Q}_m(j\omega, t) dt \tag{5.22}$$

This gives a control force

$$\begin{aligned} \mathbf{u}(t) &= \mathrm{Re}[\mathbf{U}(j\omega, t)e^{j\omega}] \\ &= \mathrm{Re}[\mathbf{U}(j\omega, t)]\cos(\omega t) - \mathrm{Im}[\mathbf{U}(j\omega, t)]\sin(\omega t) \end{aligned} \tag{5.23}$$

The implementation of ROLAC for a synchronous (single frequency) vibration control is shown in figure 5.4. Fourier coefficients, and hence control forces are

updated at each sampling period. For steady state operation, Fourier coefficients and hence the frequency response of control forces should not change. It is still effectively an open-loop control strategy as the control signals are constructed by a sine-wave generator, which is considered to be acting as an external force. Since ROLAC does not affect the system dynamic matrix (**A**) as in equation (3.5), it does not change the system natural frequencies. However, PID control can be incorporated into matrix (**A**) and changing its parameters will alter the system natural frequencies.

5.5 Simulation Results

A simulation model of the system including the contact dynamics was used to assess the feasibility of the suggested controller before applying it to the experimental system. The simulation was run at 16 Hz. Local PID controllers were incorporated into each force axis of the AMBs to achieve stability and to provide an effective bearing stiffness of 10^6 N/m and damping of 5000 Ns/m. The retainer bearing clearance is 0.75 mm. An initial steady state response was achieved by introducing a 5 gm unbalance to the disk at the non-driven end. The ROLAC controller was incorporated to minimise the sum of the squares of all 8 displacement amplitudes. The simulation was initially run with a PID controller, and then run with the ROLAC to demonstrate the effect on the rotor vibration. A sudden increase of 13.5 gm unbalance was introduced at the non-driven end disk. Figure 5.5(a) shows the radial displacements at both magnetic bearing locations. The time is normalised by the synchronous period in this and in all subsequent figures. The introduction of ROLAC decreases the vibration amplitude from 0.220 mm to to 0.035 mm at MB1, and from 0.250 mm to 0.060 mm at MB2. When the sudden unbalance force was introduced, ROLAC reacts quickly to reduce the vibration and prevents a contact with retainer bearings, whereas under the PID only controller, the rotor enters a contact mode and stays there. The corresponding orbits are shown in figure 5.5(b). The retainer bearing close to MB2 experiences bouncing type contact when PID only control is applied.

To assess the performance of the ROLAC controller under contact conditions, a second simulation was run with a sudden increase of unbalance of 20 gm at

the non-driven end disk at 16 Hz running speed. Figure 5.6(a) shows the radial displacements at both magnetic bearings. The recursive controller was not able to prevent contact, but was able to recover the rotor position in a very short time. This is a multi-contact case where the rotor comes into contact with the retainer bearing at MB1 first and then at MB2. The recovery was possible for both contact cases. The corresponding orbits are shown in figure 5.6(b). The contact was not recoverable under a PID only controller.

The integration gain parameter was set to $\alpha = 7$, which was determined in simulation by trial and error. This α value gives reasonably quick controller action without too much oscillation. Simulation run at various speeds are carried out and found that $\alpha = 7$ gives good results at all speeds within the operational running speed range. A high value of α causes oscillations before radial displacements settle on their steady-state value. However, this may be favourable in case of more severe contact cases where the oscillations occur in the non-contact region of the response.

5.6 Summary

The author has extended the existing open loop adaptive controller (OLAC) to allow an optimum control force to be updated at every sampling interval utilising a recursive Fourier transform algorithm. The performance of this recursive open loop adaptive controller (ROLAC) was examined in simulation. The Simulation results show the ability of ROLAC to prevent contact as well as vibration control of the flexible rotor.

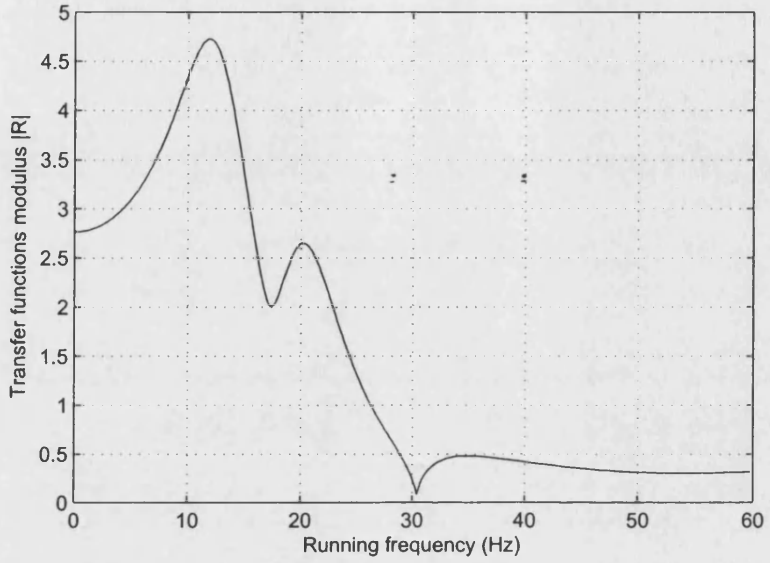

(a) Determinant of the complex partial receptance matrix

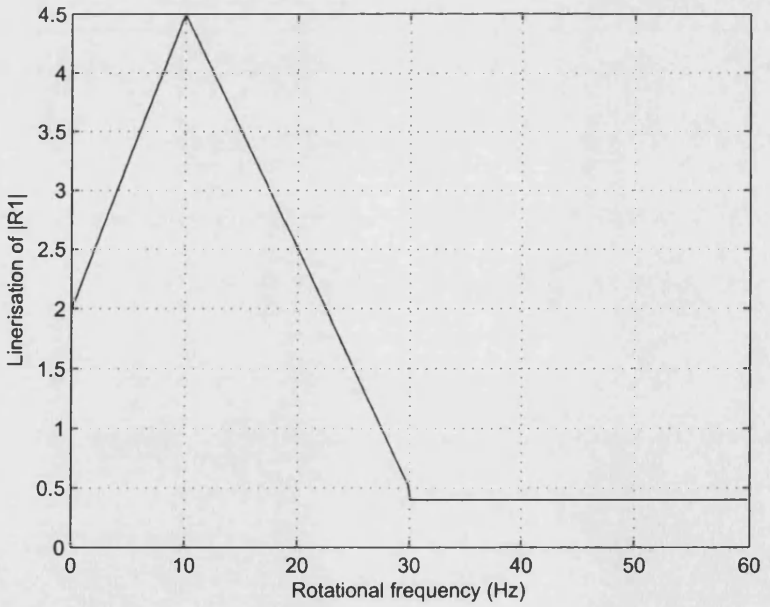

(b) Linearization of the determinant of the complex partial receptance matrix

Figure 5.1: $\mathbf{R}(j\omega)$ matrix characteristics

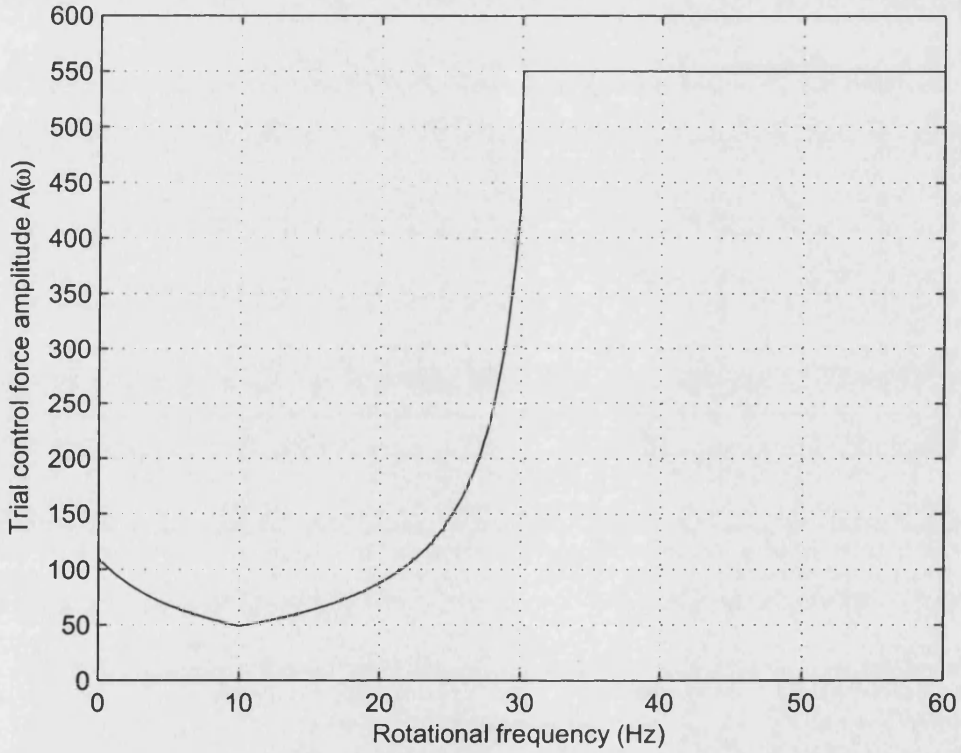

Figure 5.2: Test control force amplitude

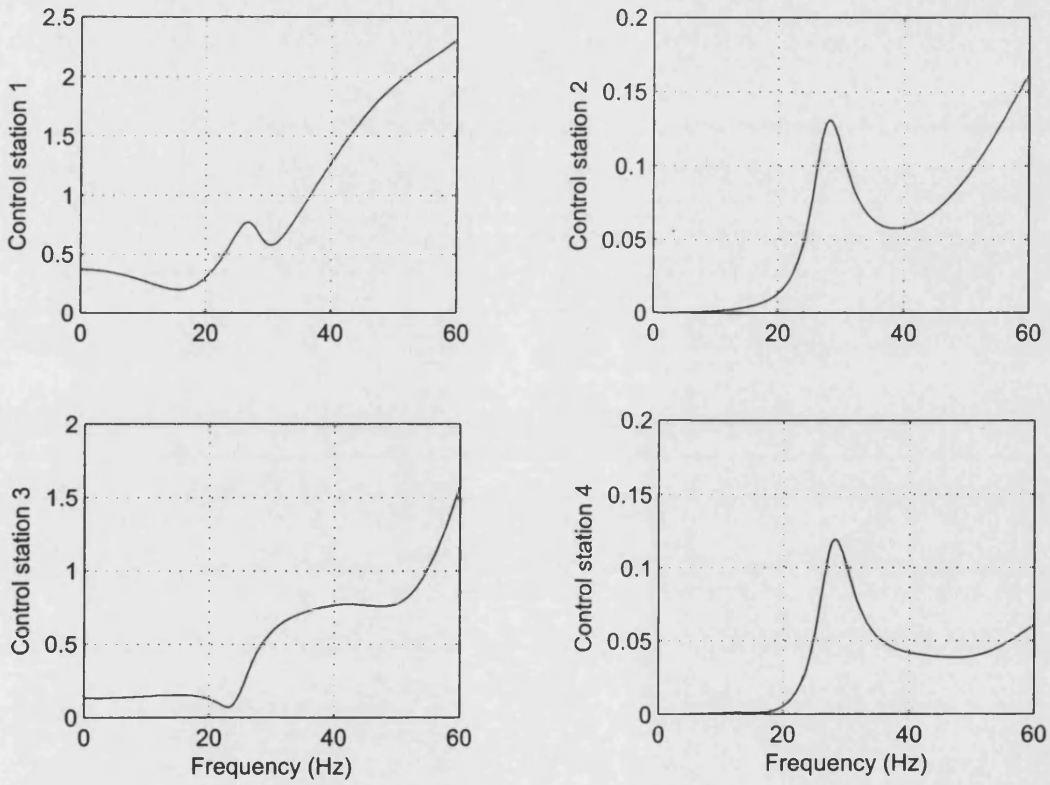

Figure 5.3: The trend of the modulus of $\mathbf{H}(j\omega)$ matrix, $|\mathbf{H}(j\omega)|$, as a function of the rotational frequency

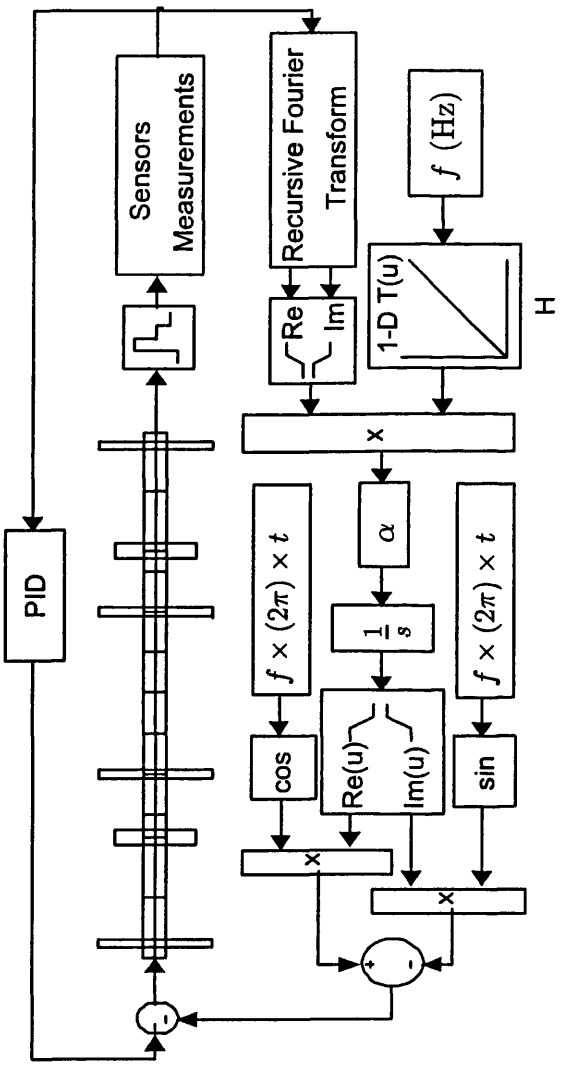

Figure 5.4: The structure of recursive open-loop adaptive control (ROLAC) for the flexible rotor/bearing system

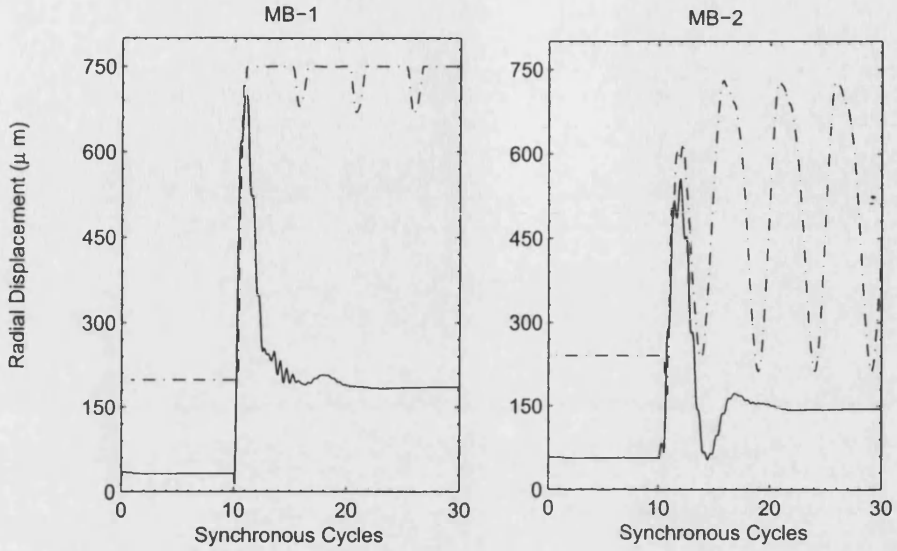

(a) Radial displacements at both AMB locations

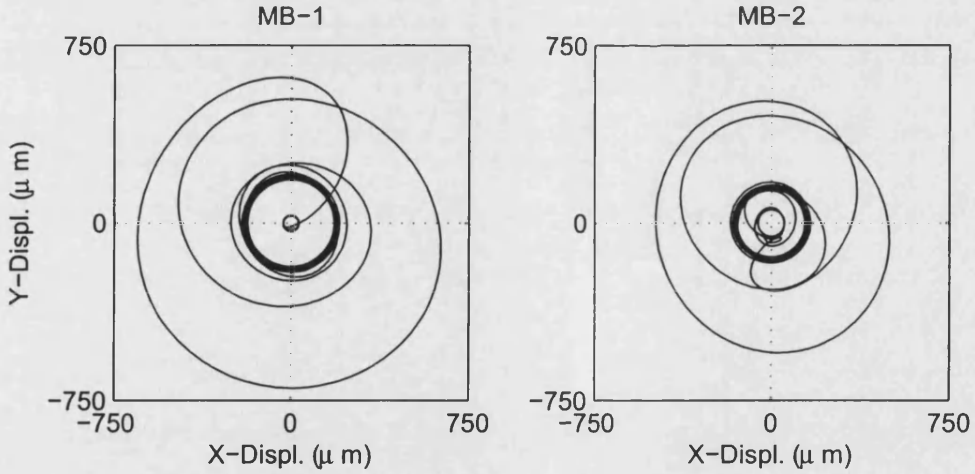

(b) Orbits under ROLAC + PID controller

Figure 5.5: Simulation results when a sudden unbalance of 13.5 gm is introduced at 16 Hz showing the performance of ROLAC compared with PID controller when contact occurs with retainer bearings at MB1 (— ROLAC & PID, -·-·-· PID only)

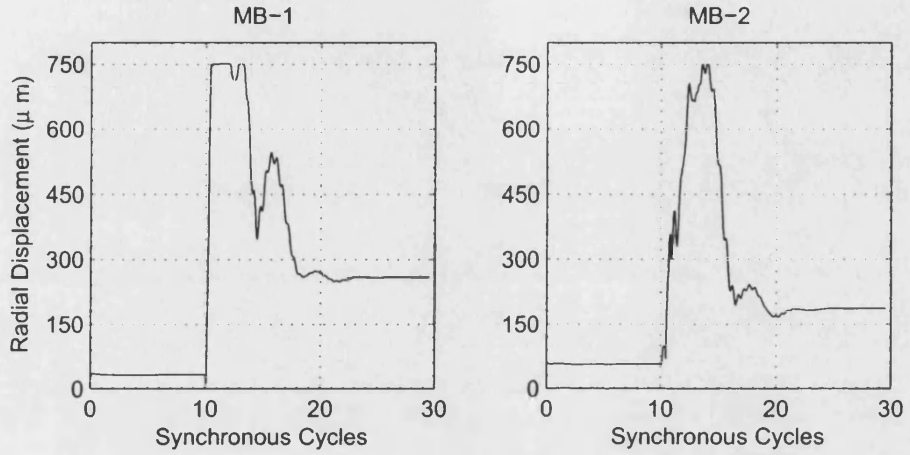

(a) Radial displacements at both AMBs

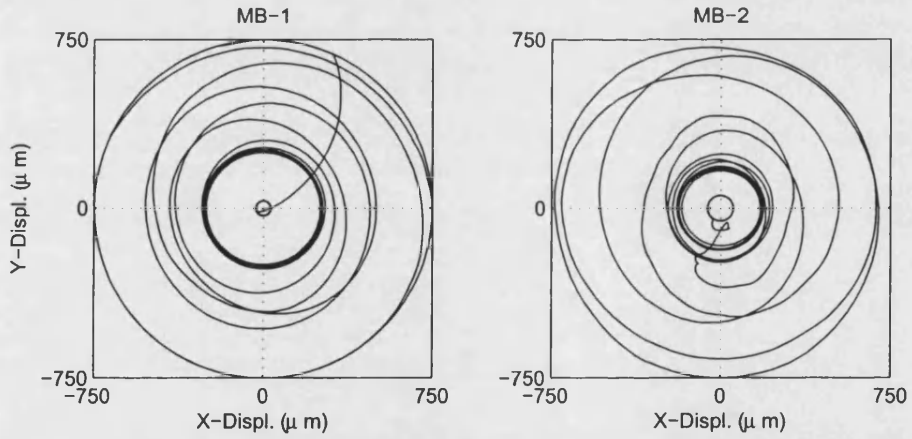

(b) Orbits at both AMBs

Figure 5.6: Simulation results showing the performance of ROLAC under contact conditions when a sudden unbalance of 20 gm is introduced at 16 Hz

Chapter 6

Real-Time Implementation of ROLAC

The control currents of the magnetic coils were supplied through eight amplifiers with a bias current of 4.3 A for the lower poles and 5.7 A for the upper poles, giving a negative stiffness of 2×10^6 N/m. The differences in bias current settings were set to generate an upwards static force to lift the shaft. As explained in the simulation section, system stability is ensured through local PID controllers, which were digitally implemented with a sampling frequency of 4 kHz.

The practical implementation of the theoretical procedure was undertaken using the Matlab/Simulink environment with the support of a dSPACE system.

6.1 On-Line Recursive Fourier Transform

The Fourier transform block is designed as an enabled system to perform recursive Fourier analysis of the sensor signals $\mathbf{q}(t)$ at the operational speed (fundamental frequency f_o) as explained in section 5.4. This block is executed at each time step above the running frequency threshold value of 5 Hz. As the Fourier transform model uses a running average window, one cycle of running operation has to be completed before the outputs give the correct components. However, this affects only the first 0.2 s of operation at 5 Hz. The Fourier block can be set to calculate the sine component $\mathbf{a}_n$ and cosine component $\mathbf{b}_n$ of the complex output of the fundamental, or any harmonic component of the sensors signals as follows:

$$\begin{aligned} \mathbf{a}_n &= \mathbf{Ic}(t) - \mathbf{Ic}(t-T) \\ \mathbf{b}_n &= \mathbf{Is}(t) - \mathbf{Is}(t-T) \end{aligned} \tag{6.1}$$

where

$$\begin{aligned} \mathbf{Ic}(t) &= \frac{2}{T}\int_0^t \mathbf{q}(t)\cos(n\omega t)\,dt \\ \mathbf{Is}(t) &= \frac{2}{T}\int_0^t \mathbf{q}(t)\sin(n\omega t)\,dt \\ T &= \frac{1}{f_o} \end{aligned} \tag{6.2}$$

On-line implementation of equation (6.1) is represented in figure 6.1. In the calculation of $sin\omega t$ and $cos\omega t$, using the running time t to calculate the Fourier transform will lead to errors in the complex components since it can have very large values. This error accumulates with increasing time. For this reason, the time was set to be zero at the start of each synchronous cycle. This cyclic time was called 'base time' and is shown in figure 6.2. This base time will have values between 0 and T.

6.2 On-Line Identification of the Partial Receptance Matrix

The procedure for the estimation of the receptance matrix was explained in section 5.3. The partial receptance matrix $\mathbf{R}(j\omega)$ estimation is an enabled block initiated by the operator through the graphical user interface using the ControlDesk software of dSPACE. Initiating the estimation block will set the block internal time to zero, which will be referred to as absolute time t_{abs}. This procedure is automatically halted when, for example the estimation block is disabled, or the absolute time reaches a predefined time t_{halt} as follows:

$$t_{halt} = \frac{1}{f_o} \times N_{per} \times 6 \tag{6.3}$$

where

$$N_{per} = max\,(3f_o\,,\ 45) \tag{6.4}$$

In equation (6.3) the number of periods N_{per} represents the number of synchronous cycles needed for the rotor to reach steady-state response after applying the test control force in any axis of the magnetic bearings. The number of test control forces is four, but additional time was considered for safety before applying the first test control force and after last test control. That ensured the collected results were performed during the steady state dynamic response of the rotor. Equation (6.4) defines the minimum requirement of synchronous cycles before the rotor reaches steady state and any data collection can be performed. It is difficult to analytically find this value, thus it was experimentally obtained as minimum of 45 synchronous cycles until the running speed reached 15 Hz at which N_{per} was calculated as expressed in equation (6.4).

The estimation block receives the Fourier transform of all sensors signals and the test control forces. The test control force was calculated as follows:

$$\delta u(j\omega_o) = A(\omega_o)\cos\left(\omega_o t + \psi\right) \tag{6.5}$$

with the following amplitude settings, as explained in section 5.3:

$$A(\omega_o) = \begin{cases} \dfrac{220}{0.25\omega_o + 2} & 0 \leq \omega_o \leq 10 \\ \dfrac{220}{-0.2\omega_o + 6.5} & 10 \leq \omega_o \leq 30 \\ \dfrac{220}{0.4} & \omega_o \geq 30 \end{cases} \tag{6.6}$$

The test control force was applied through each individual axis in sequence according to a control signal as shown in figure 6.3 and designed as follows:

$$floor\left(\frac{\left|(t_{abs} - \frac{1}{f_o})\right|}{(N_{per} * \frac{1}{f_o})}\right) \tag{6.7}$$

where *floor* for a number, say A, that rounds towards minus infinity, that is the nearest integer less than or equal to (A).

The test control force was applied at each axis of both magnetic bearings for N_{per} number of periods. The sensor signal information was continuously fed through the recursive Fourier transform. The Fourier analysis results were collected at the end of each sequence, and used to calculate the relevant column of the $\mathbf{R}(j\omega)$ matrix. Figure 6.4 shows the trigger signal used to execute the enabled block to estimate $\mathbf{R}_i(j\omega)$ as explained in equation (5.17). The control matrix $\mathbf{H}(j\omega)$ was calculated from equation (5.10).

The $\mathbf{H}(j\omega)$ matrix was estimated experimentally at twelve carefully selected rotational speeds and stored in a file to be used in subsequent runs. The twelve discrete running speeds were [5, 10, 15, 20, 22, 24, 25, 26, 27, 28, 29, 35] Hz. These values were chosen according to the linearized determinant of the complex partial receptance matrix shown in figure 5.1(b). The $\mathbf{H}(j\omega)$ matrix was stored in steps of 5 Hz up to a running speed of 20 Hz. The experimental tests showed that between 20 Hz and 29 Hz the system is very sensitive to changes, thus the $\mathbf{H}(j\omega)$ matrix was stored with smaller steps. This agrees with the variation of the determinant of the complex partial receptance matrix as shown in figure 5.1(a).

For each new estimate of $\mathbf{H}(j\omega)$, the program examined the existing data at that running speed and updated the data file accordingly. A linear interpolation was used to determine the $\mathbf{H}(j\omega)$ matrix at rotational speeds between the stored values during the run-up. As an example of the estimated $\mathbf{H}(j\omega)$ matrix, with units of $\left(\frac{N}{\mu m}\right)$, at $\Omega = 10$ Hz is as follows:

$$\mathbf{H}(j\omega) = \begin{pmatrix} 0.162+0.031i & -0.074+0.158i & 0.150+0.013i & -0.003+0.131i \\ 0.141+0.015i & -0.046+0.148i & 0.147+0.007i & -0.007+0.131i \\ 0.141+0.009i & -0.023+0.131i & 0.181+0.016i & -0.031+0.138i \\ 0.146+0.012i & -0.012+0.148i & 0.209+0.029i & -0.045+0.165i \end{pmatrix}$$

$$\begin{pmatrix} 0.127+0.011i & -0.007+0.114i & -0.006+0.001i & 0.001+0.027i \\ 0.095+0.007i & 0.001+0.080i & 0.018+0.005i & 0.004+0.048i \\ 0.045+0.003i & 0.002+0.037i & 0.060+0.003i & 0.003+0.101i \\ 0.032+0.001i & 0.0004+0.016i & 0.096+0.003i & 0.004+0.132i \end{pmatrix}$$

It is essential to halt the ROLAC update by setting the integration parameter α to zero so that the estimation procedure is not interrupted. The estimation and the ROLAC control is designed so that when the operator starts the estimation procedure, a command signal will automatically be sent to the ROLAC to halt it. The integration parameter is set back to its original value when the estimated $\mathbf{H}(j\omega)$ is completed.

For multi-frequency controllers, this procedure is repeated for other harmonics 2ω, 3ω, 4ω etc. Alternatively, the test control force can be designed as a multi-frequency signal. A Schroeder Phased Harmonic Sequence (SPHS) [96] is well suited for this purposes as it is a low peak factor signal and the frequency component can be controlled with ease. The SPHS control force will excite the system frequencies. The sensor information can be analyzed with the Fourier transform

for the fundamental frequency and its subsequent harmonics. That will provide estimation of $\mathbf{H}(j\omega)$, $\mathbf{H}(j2\omega)$, $\mathbf{H}(j3\omega)$, $\mathbf{H}(j4\omega)$ in a single test.

6.3 Implementation of ROLAC

ROLAC is designed as an enabled system, which is enhanced by the operator. It receives the coefficients of the Fourier transform, integration parameter α, base time, the control matrix $\mathbf{H}(j\omega_o)$ and the running frequency. The control matrix $\mathbf{H}(j\omega_o)$ is multiplied by $\mathbf{Q}(j\omega_o)$ from all sensors to calculate the optimum change in the ROLAC control force required to minimise the sum of the squares of the rotor response at the running frequency as explained in equation (5.9). The complex optimum control is rearranged as real and imaginary parts and multiplied by the integrator parameter as in equation (5.22) and passed through a triggered integrator as shown in figure 6.5. The triggered integrator resets its state to a pre-defined initial condition (zero) based on an external signal that triggers the start of the ROLAC controller. This will prevent any windup problem.

6.4 Experimental Verification of ROLAC

6.4.1 Vibration Attenuation using ROLAC

The initial experimental tests were performed at 10 Hz. Figure 6.6 shows the displacements measured by four transducers at the two magnetic bearing locations. The initial response was due to the unknown inherent unbalance distribution along the rotor and with PID only control. A significant reduction in vibration levels was observed at all measurement sites when the ROLAC was switched on at the point shown in figure 6.6. The corresponding orbits at four measurement sites are shown in figure 6.7, clearly demonstrating the benefit and speed of the ROLAC. Due to low vibration levels and transducers noise the response does not appear to be elliptic as shown in figure 6.7 which are magnified as can be seen from the axis scales.

The effect of ROLAC to attenuate vibration due to unknown unbalance shows its distinguished performance at high rotational speeds. An additional two experiments were conducted at running speeds of 16 Hz and 35 Hz. The measured displacements at the selected sensors which correspond to MB1 and the non driven end of the rotor at running speed of 16 Hz are shown in figure 6.8. The reduction in vibration level is more significant at the outer end, 7^{th} and 8^{th} sensor locations, reading about 0.05 mm from approximately 0.35 mm while it reads at 5^{th} and 6^{th} sensor locations about 0.10 mm from 0.20 mm. The effect of ROLAC can be noticed immediately. The experimental orbits at the measured locations are shown in figure 6.9.

Figures 6.10 and 6.11 compare the measured displacements under PID only controller with PID and ROLAC controller. Significant reduction in the vibration levels can clearly be seen. The reduction in vibration level is significant at MB1 and MB2 sensors, 3^{rd} and 4^{th} sensor locations, reading about 0.05 mm and 0.065 mm from approximately 0.4 mm and 0.3 mm, respectively, while it reads at 5^{th} and 6^{th} sensor locations about 0.05 mm at both sensors from 0.4 mm and 0.35 mm, respectively. The corresponding orbits at MB1 and MB2 are shown in figures 6.12(a) and 6.12(b), respectively.

6.4.2 Preventing Contact using ROLAC

A sudden additional synchronous force 544 N (equivalent to 54.4 gm unbalance) was experimentally applied through both magnetic bearings at a constant rotational speed of 16 Hz. Figure 6.13 shows the orbits at both magnetic bearing locations. Figure 6.13(a) shows the case where only PID controller is used. The shaft is trapped into a contact mode soon after the introduction of the sudden unbalance force. However, with ROLAC, the rotor position is recovered as shown in figure 6.13(b). Not only the rotor position is recovered, but also the vibration levels are reduced to a very low level. The measured radial displacements at both magnetic bearing locations are shown in figure 6.14. The sudden unbalance disturbance was applied at about the 5^{th} synchronous cycle.

The speed of the ROLAC to recover the rotor position, and its ability to reduce the vibration levels to a very low level can be clearly seen. The rotor oscillates

within the retainer bearing clearance before it settles to a low vibration level. This is dependent on the integration gain (α). Decreasing it will decrease the oscillations, but at the cost of the controller speed reaching its optimal value. The integrator gain must be tuned experimentally to suit different applications. In this work, the estimated gain value is 7 which is in agreement with the simulation work, thus it is shown to be the best value in this application.

6.4.3 Recovering Rotor Position using ROLAC

Preventing the rotor from contacting the retainer bearings under all conditions is not possible. However, it is possible to recover rotor position after few cycles in contact using ROLAC control where PID only controller fails under the same conditions. The first experiment was run at a constant running speed of 10 Hz. A sudden additional synchronous force 800.6 N (equivalent to 203 gm unbalance) was experimentally applied through both magnetic bearings. Figure 6.15 shows the measurements at the magnetic bearings with PID control and the rotor is trapped in a contact condition. Figure 6.16 shows the measured radial displacements where the rotor were in contact for approximately two cycles at when ROLAC recovers the rotor position form contact and brings it to a low level of vibration. Figure 6.17 shows the orbits at both magnetic bearings with PID only control as shown in figure 6.17(a) compared to the orbits with PID and ROLAC as shown in figure 6.17(b).

An additional experimental test was run at 12.5 Hz with a sudden additional

synchronous force 650 N (equivalent of 105.4 gm of unbalance) applied through the out of balance end magnetic bearing. The radial displacements of both magnetic bearings are shown in figures 6.18 and 6.19 for PID and ROLAC & PID, respectively. The second magnetic bearing has more oscillation under the effect of ROLAC than with PID only control, but clearly contact at the first magnetic bearings has been prevented. The radial displacements at the magnetic bearing settle to a low level of vibration after several cycles. The corresponding orbits are compared in figure 6.20.

Figures 6.19 and 6.20 clearly indicate that the rotor position is recovered from contact with the retainer bearings at both magnetic bearing locations. However, in this case, the recovery seems to be in two stages. In the first step, the orbits settles to an intermediate level before being reduced to the eventual optimal position. This is probably due to the inaccuracies in recursive Fourier transform during the transient period. In addition, when under contact condition, the integral parameter α causes oscillations. This is not a concern in the present application as the rotor benefits from recovered position at MB1 while MB2 oscillates within the clearance with a short period of light contact. However, both bearing reach steady state orbit size within the clearance.

6.5 Summary

Experimental work was undertaken using a flexible rotor/magnetic bearing system to validate the modelling technique developed by the author. Experiments included single and multiple contact cases. Contacts were initiated by a sudden synchronous force introduced through the magnetic bearings. In all cases, the measured rotor responses were consistent with the simulation results, including the behaviour of the rotor after the removal of the synchronous forces.

The experimental results show the ability of ROLAC to attenuate vibration due to unknown out of balance forces and also to act quickly in case of sudden change of synchronous force. The controller is able to prevent contact in some cases and to recover rotor position, in others, if contact occurs.

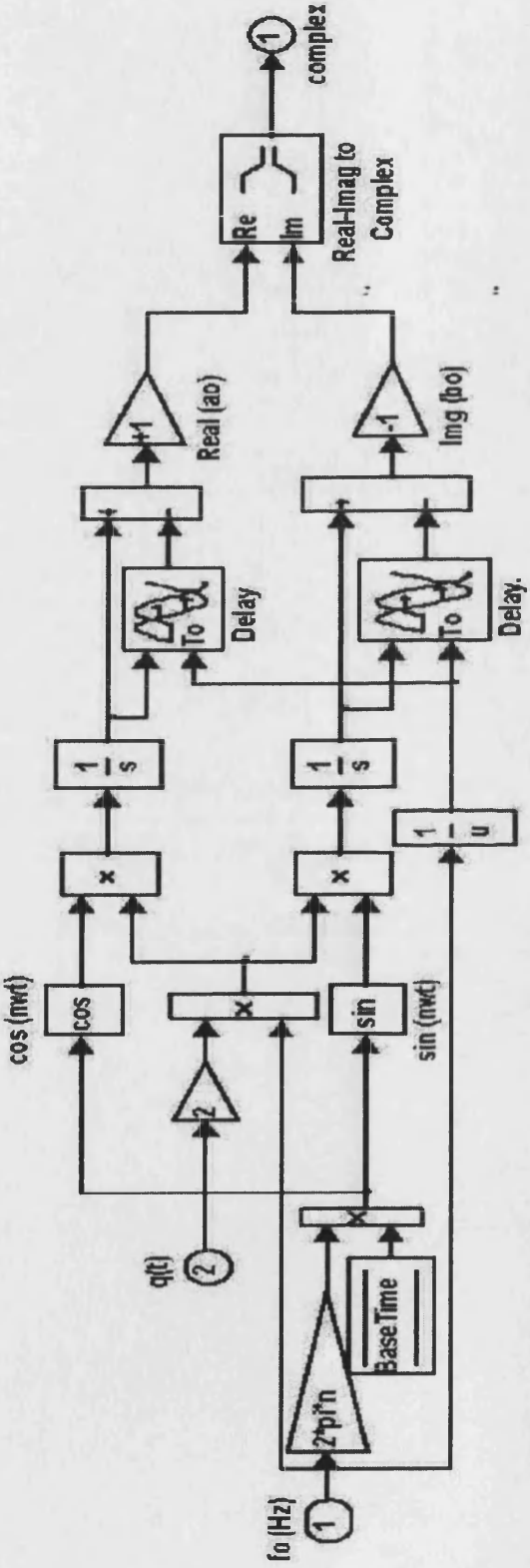

Figure 6.1: Recursive Fourier transform in Simulink block diagram

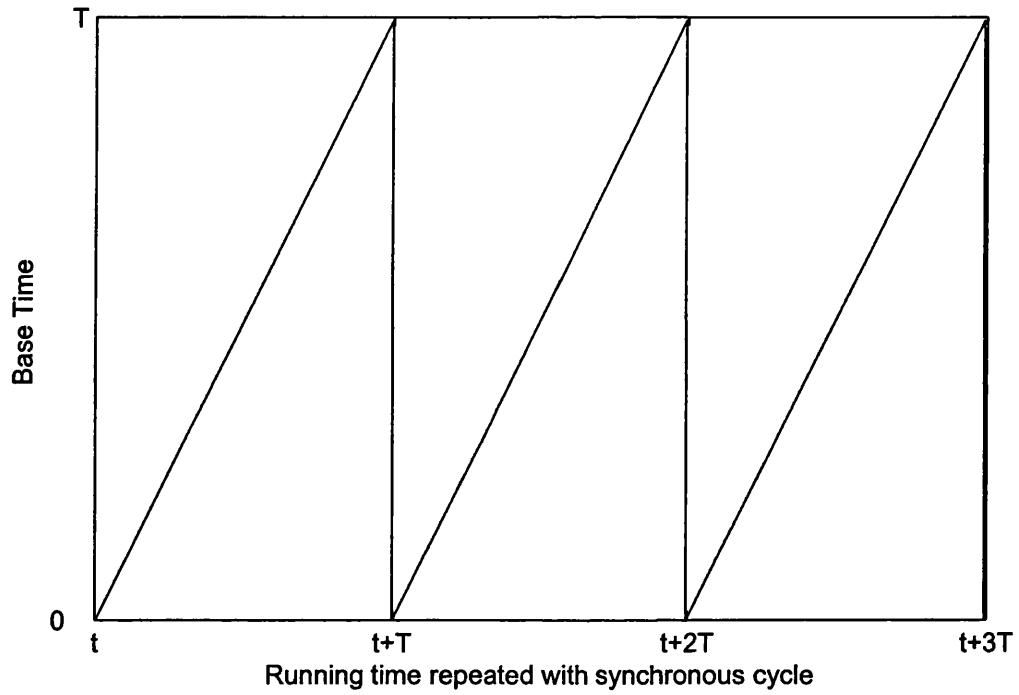

Figure 6.2: Base time used in Fourier transform calculation

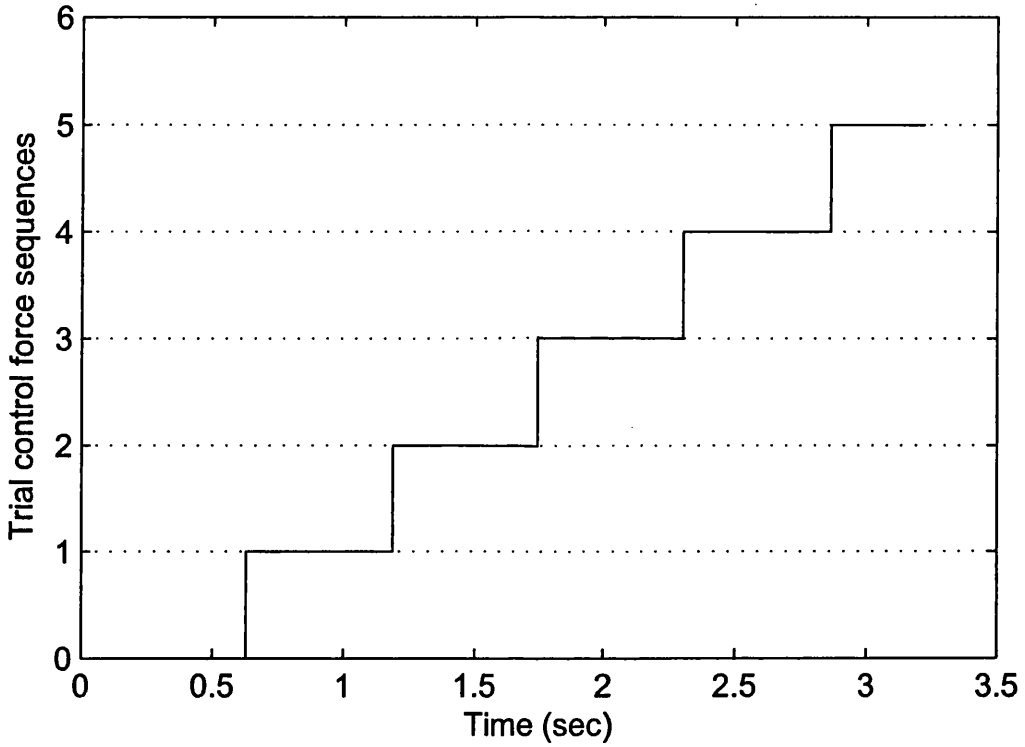

Figure 6.3: Test control force sequence at f_o Hz where 0: no force, 1: x-axis MB1, 2: y-axis MB1, 3: x-axis MB2, 4: y-axis MB2, 5: no force

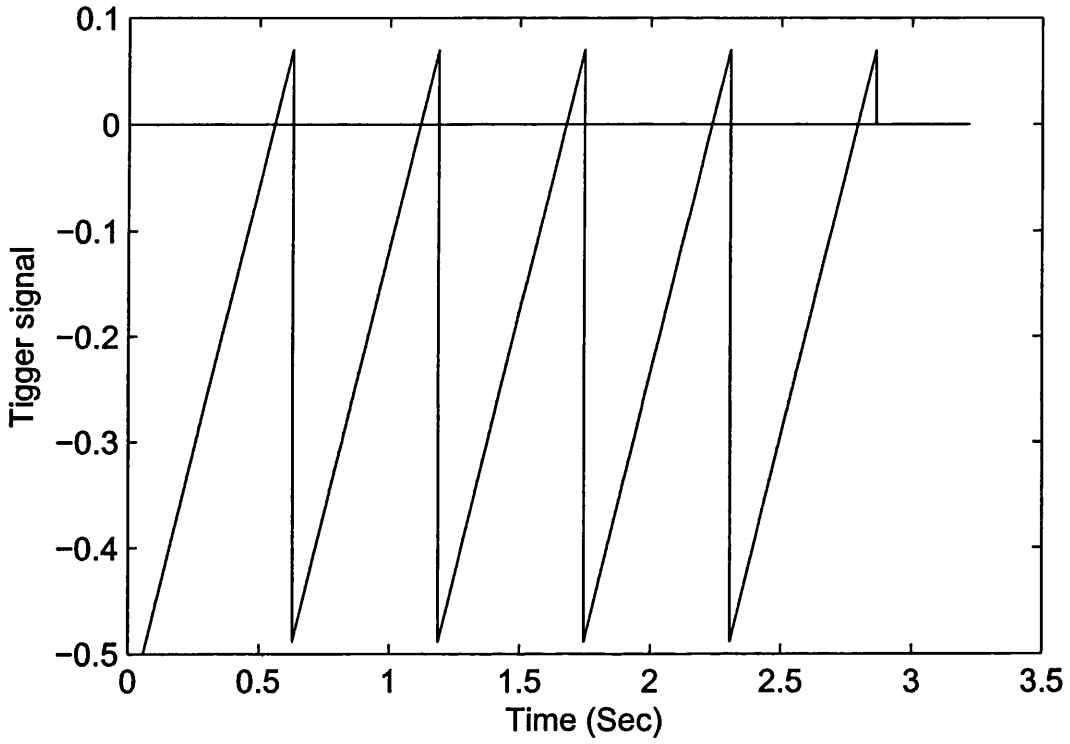

Figure 6.4: Data storage trigger signal

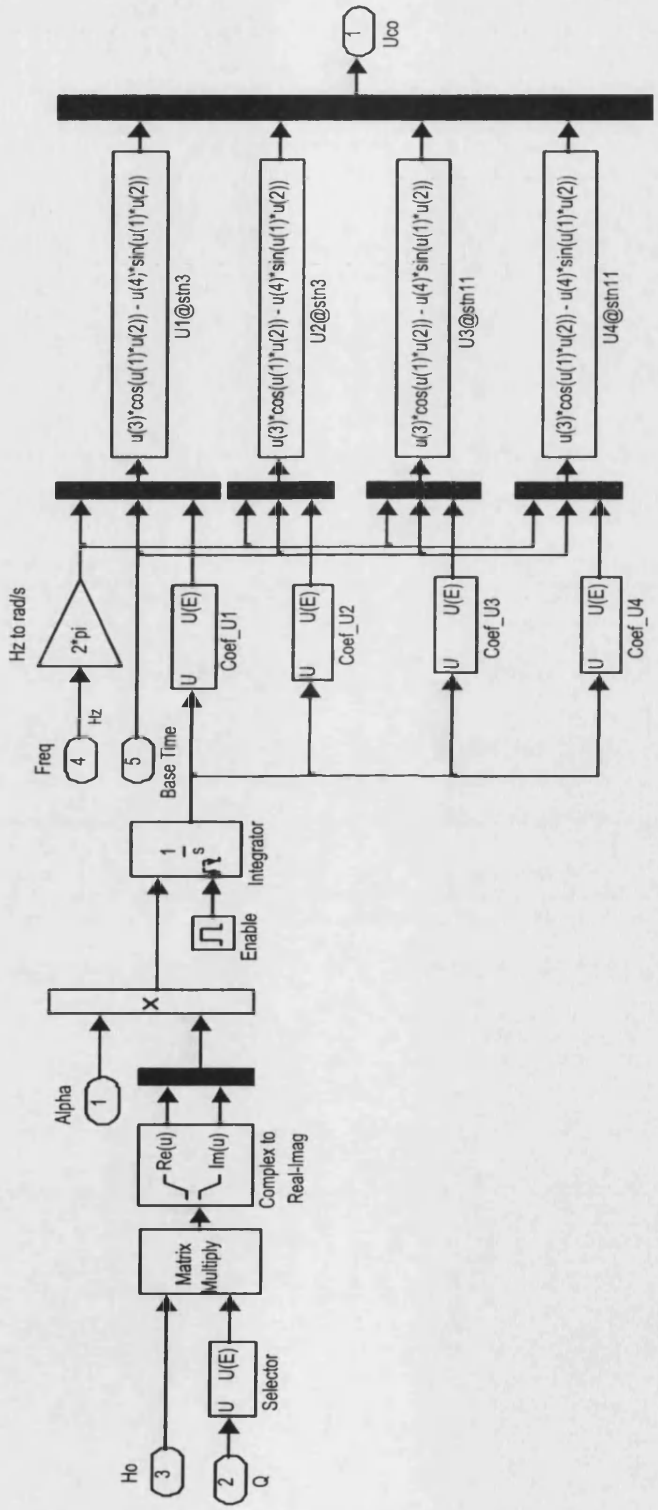

Figure 6.5: ROLAC system configuration as a Simulink block diagram

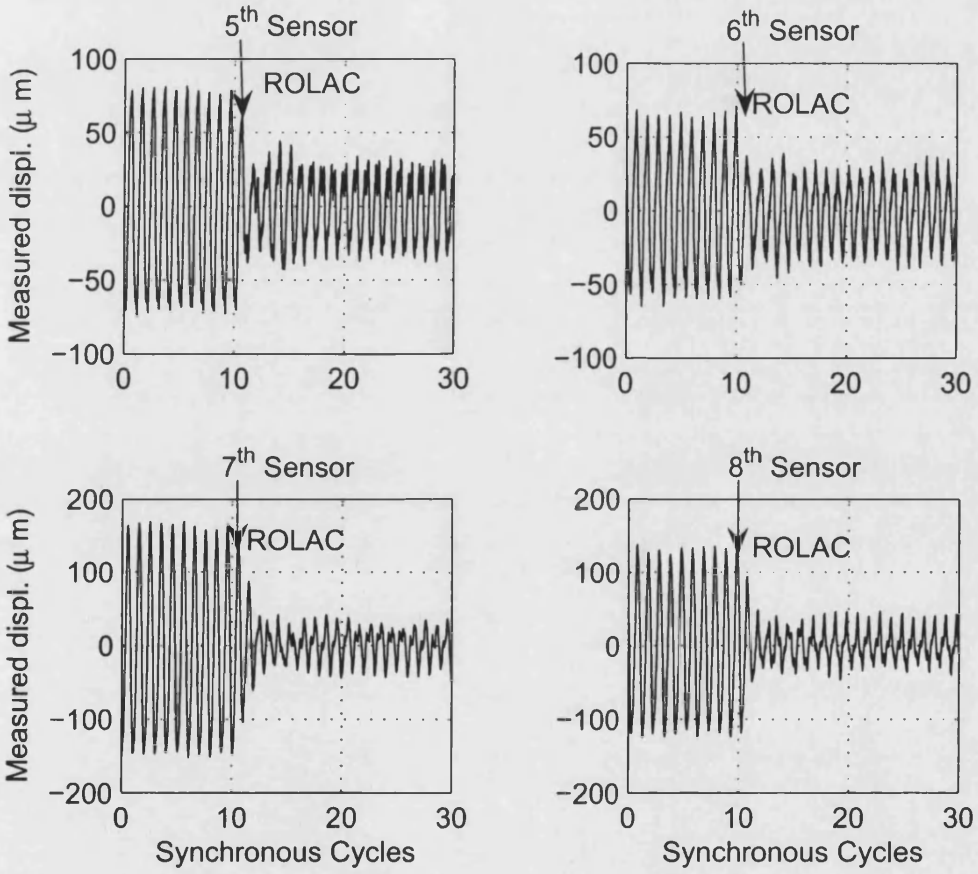

Figure 6.6: Measured displacements at selected sensors showing the effect of ROLAC compared to PID control at 10 Hz

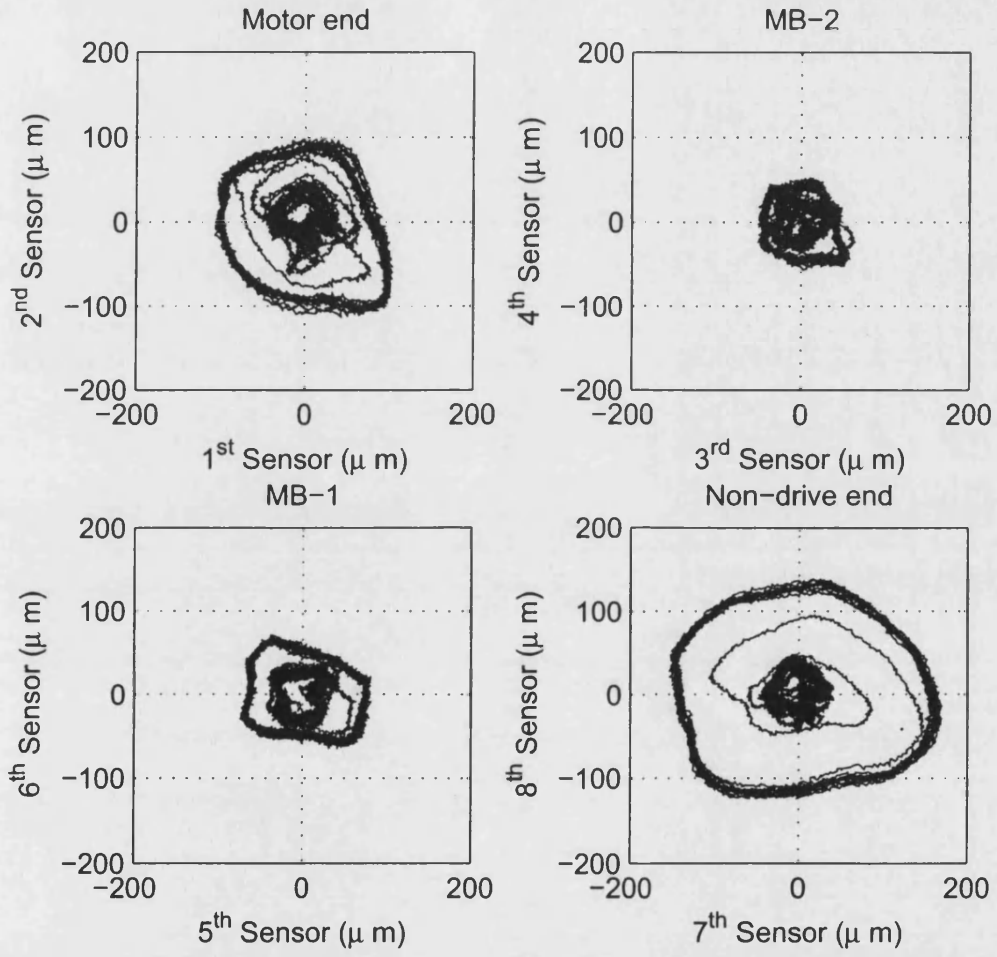

Figure 6.7: Rotor orbits at all measurements planes before (PID) and after (PID & ROLAC) the application of control forces at 10 Hz

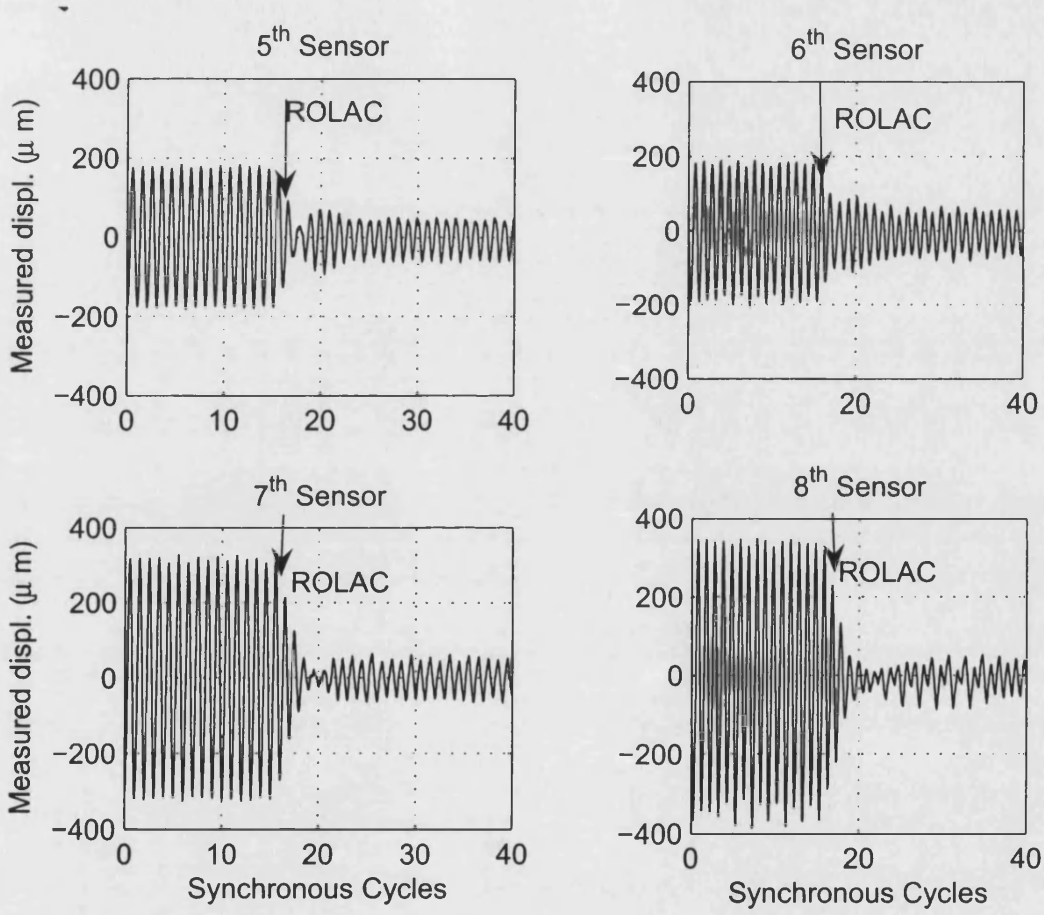

Figure 6.8: Measured displacements at selected sensors showing the effect of ROLAC compared to PID control at 16 Hz

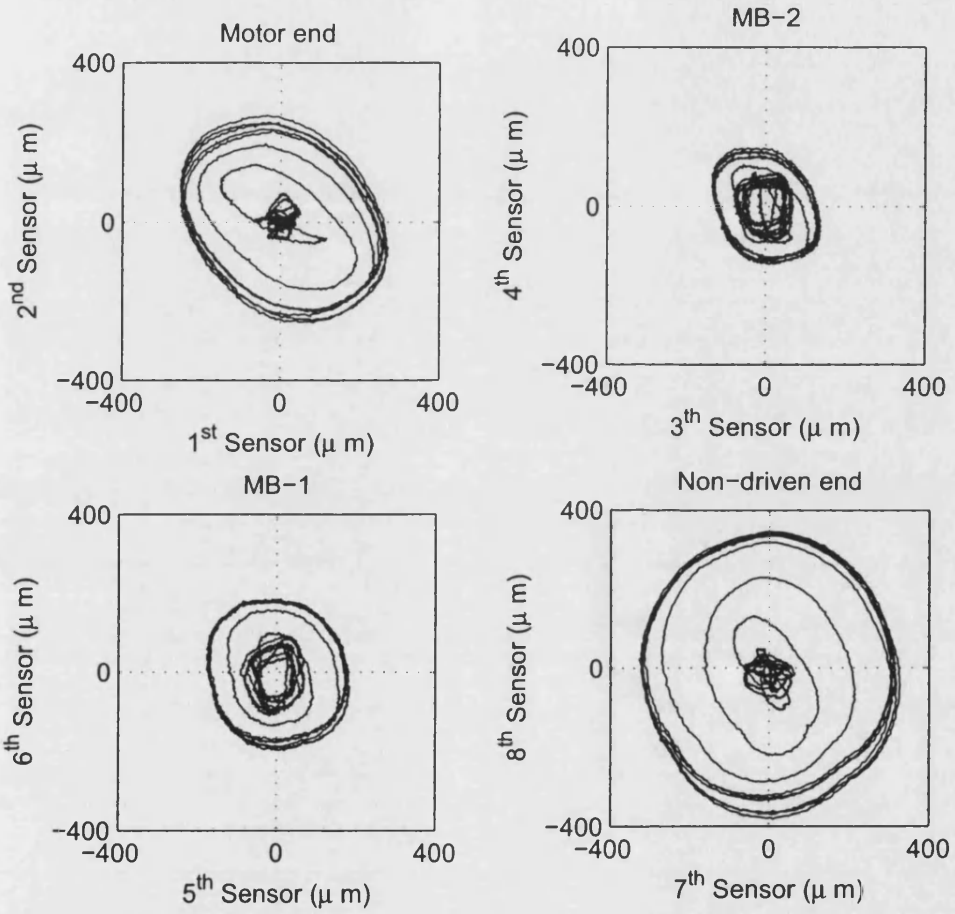

Figure 6.9: Rotor orbits at all measurements planes before (PID) and after (PID & ROLAC) the application of control forces at 16 Hz

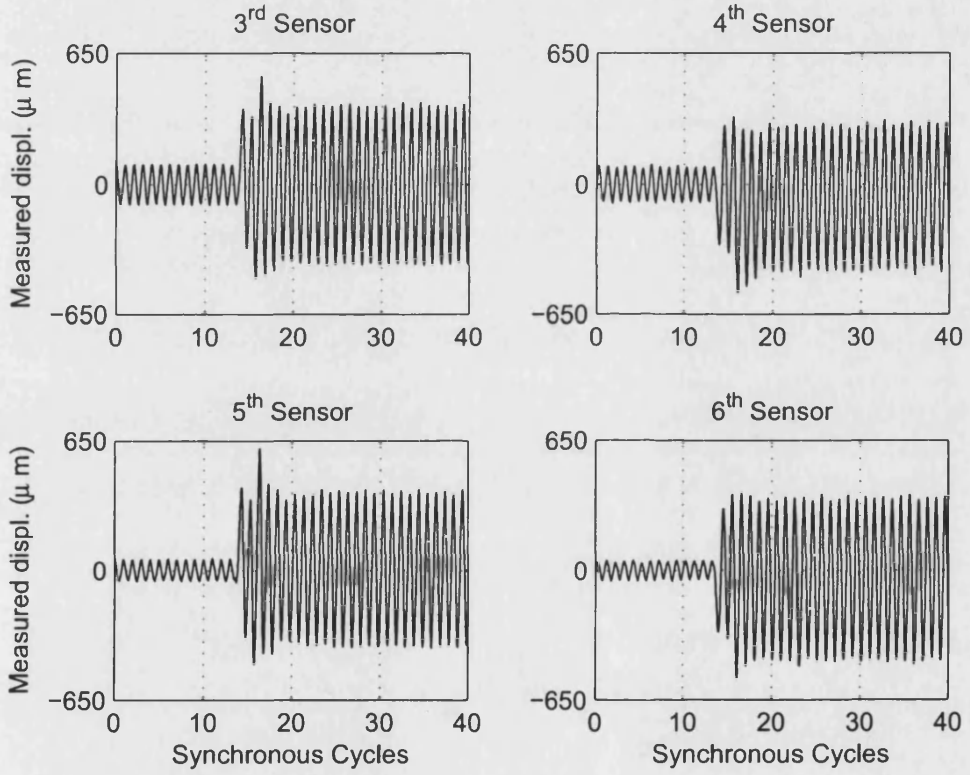

Figure 6.10: Measured displacements at both bearing sensors showing the effect of PID control at 35 Hz

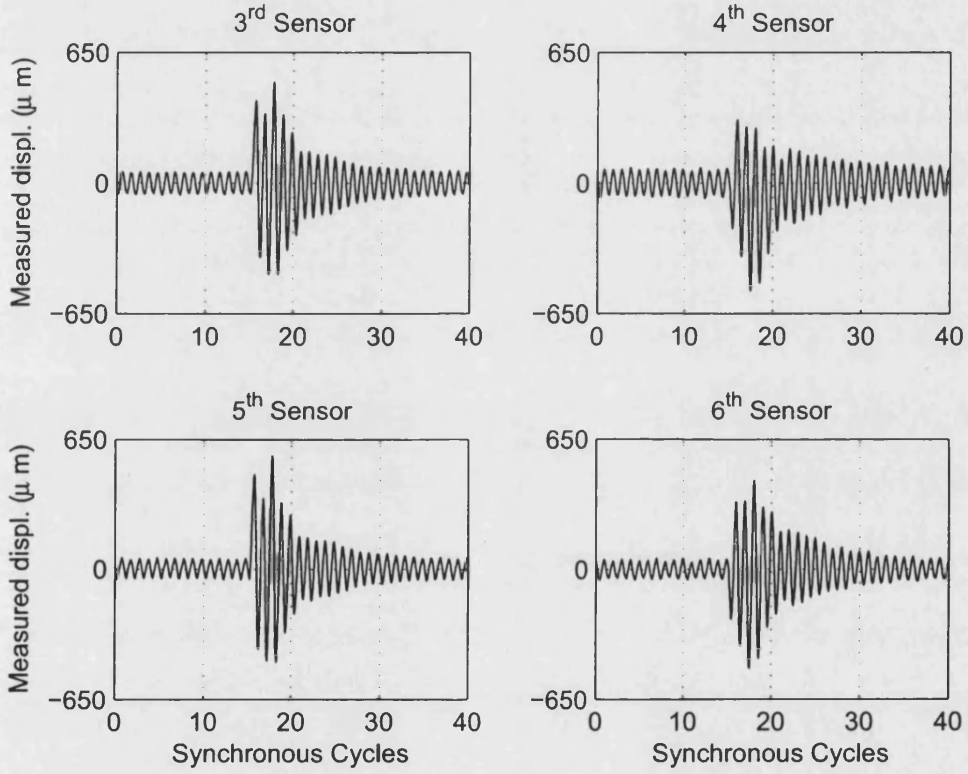

Figure 6.11: Measured displacements at both bearing sensors showing the effect of PID control & ROLAC at 35 Hz

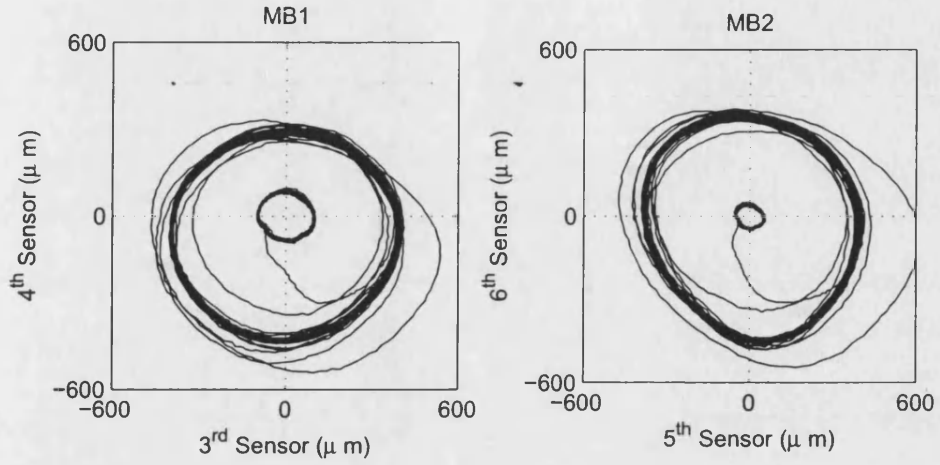

(a) PID only controller.

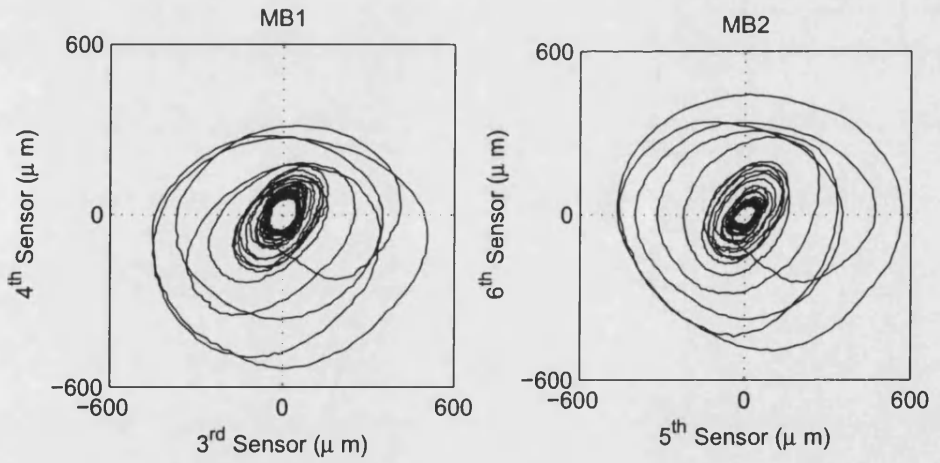

(b) PID+ROLAC

Figure 6.12: Experimental orbits at both magnetic bearing locations when a sudden synchronous force was applied through the magnetic bearings at 35Hz

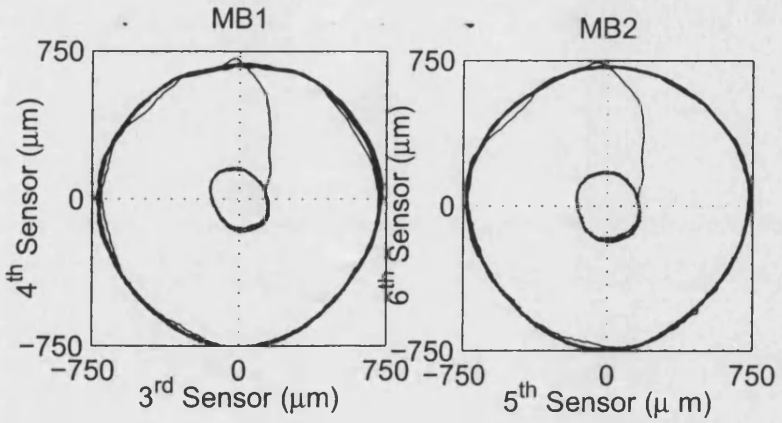

(a) PID only controller.

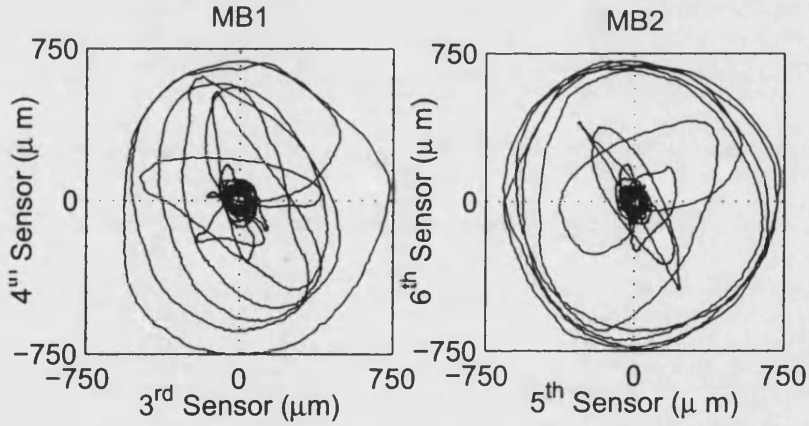

(b) PID+ROLAC

Figure 6.13: Experimental orbits at both magnetic bearing locations when a sudden synchronous force was applied through the magnetic bearings

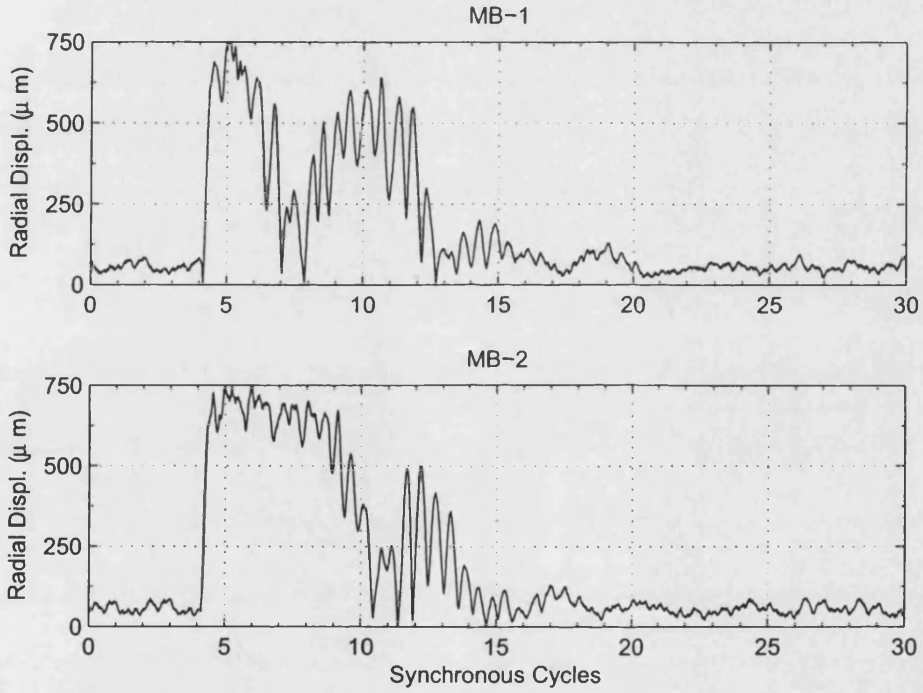

Figure 6.14: Measured radial displacements of the rotor with the application of the ROLAC forces

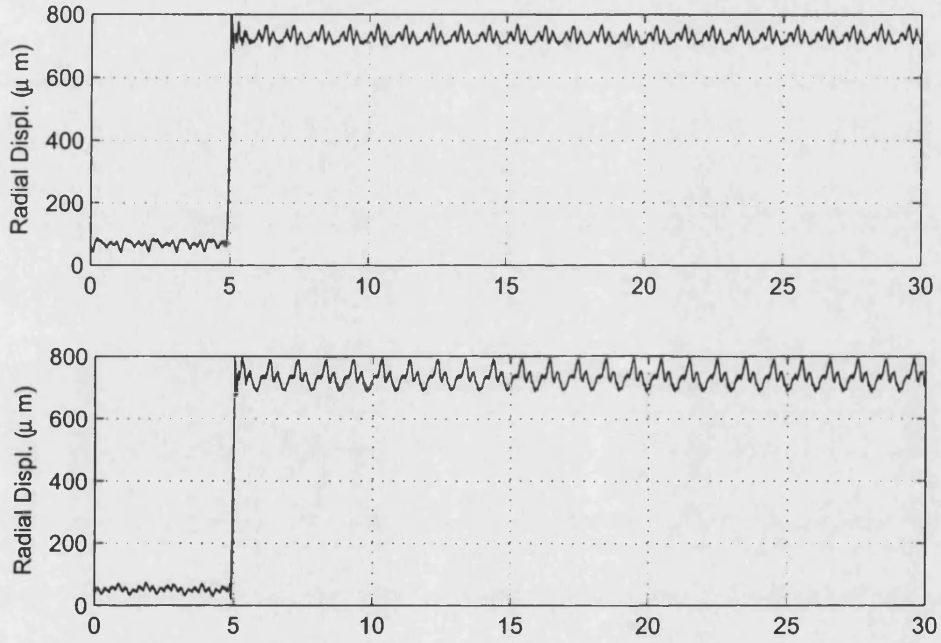

Figure 6.15: Measured radial displacements of the rotor with the application of the PID control forces at 10 Hz

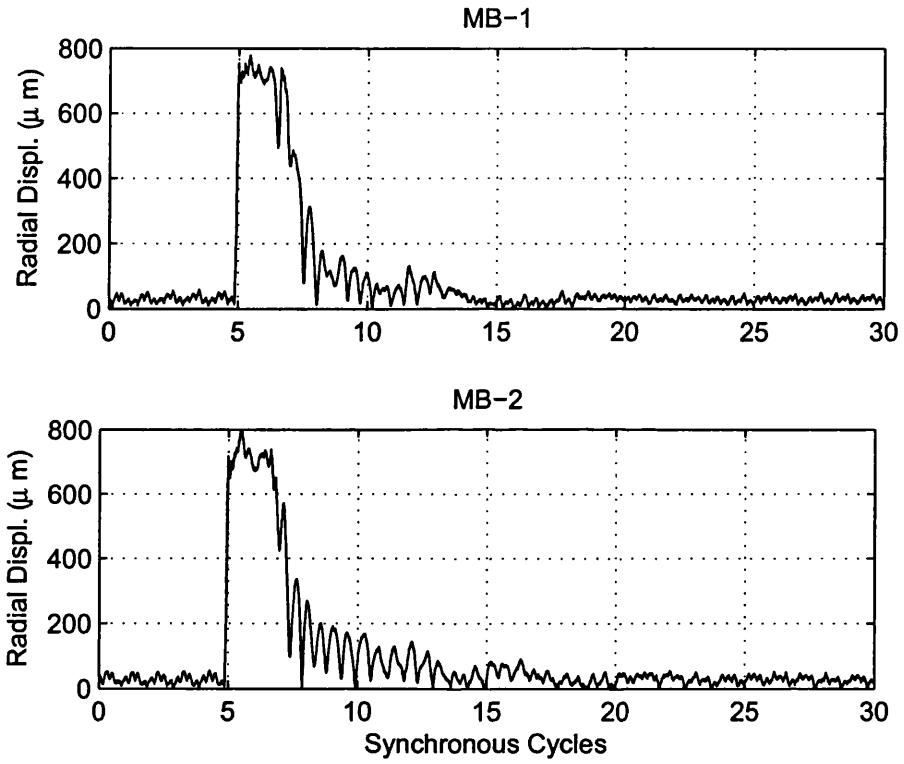

Figure 6.16: Measured radial displacements of the rotor with the application of the ROLAC forces at 10 Hz

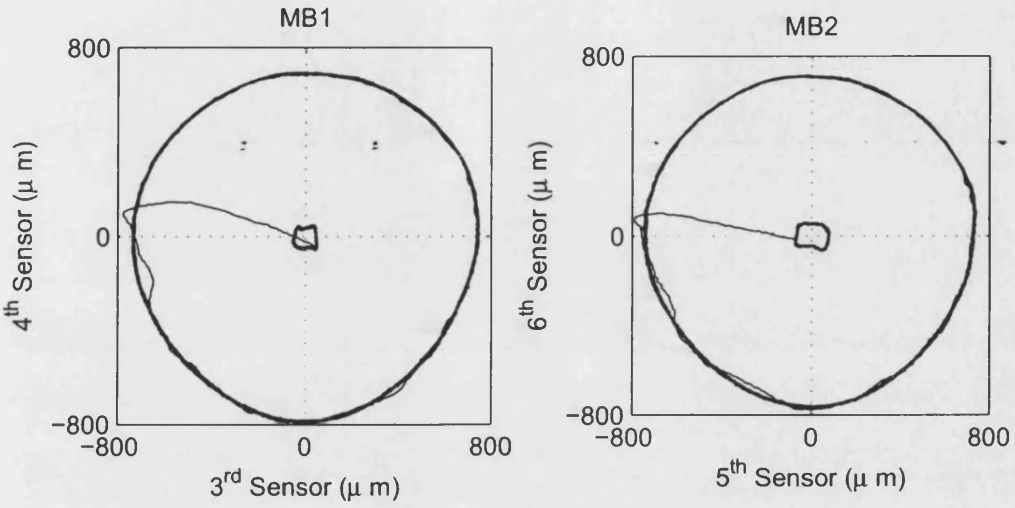

(a) PID only controller.

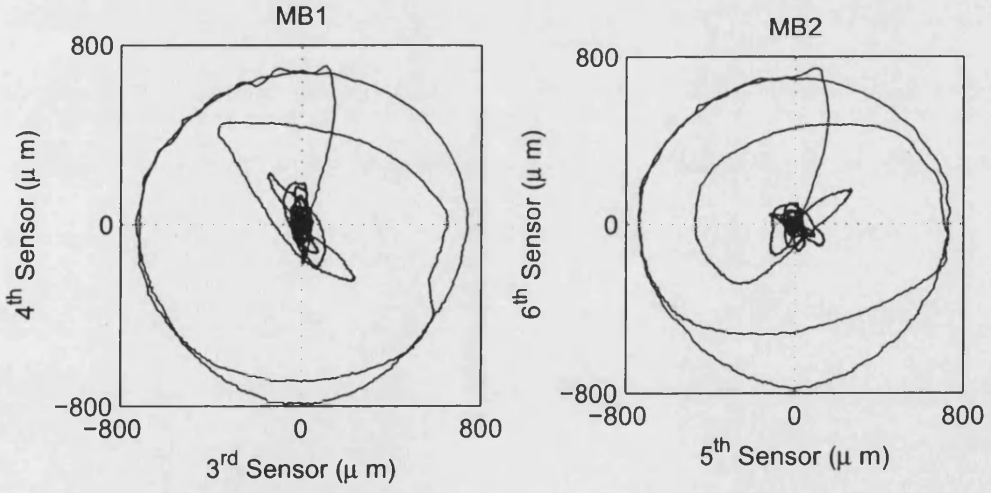

(b) PID+ROLAC

Figure 6.17: Experimental orbits at both magnetic bearing locations when a synchronous force was applied through the magnetic bearings at 10 Hz

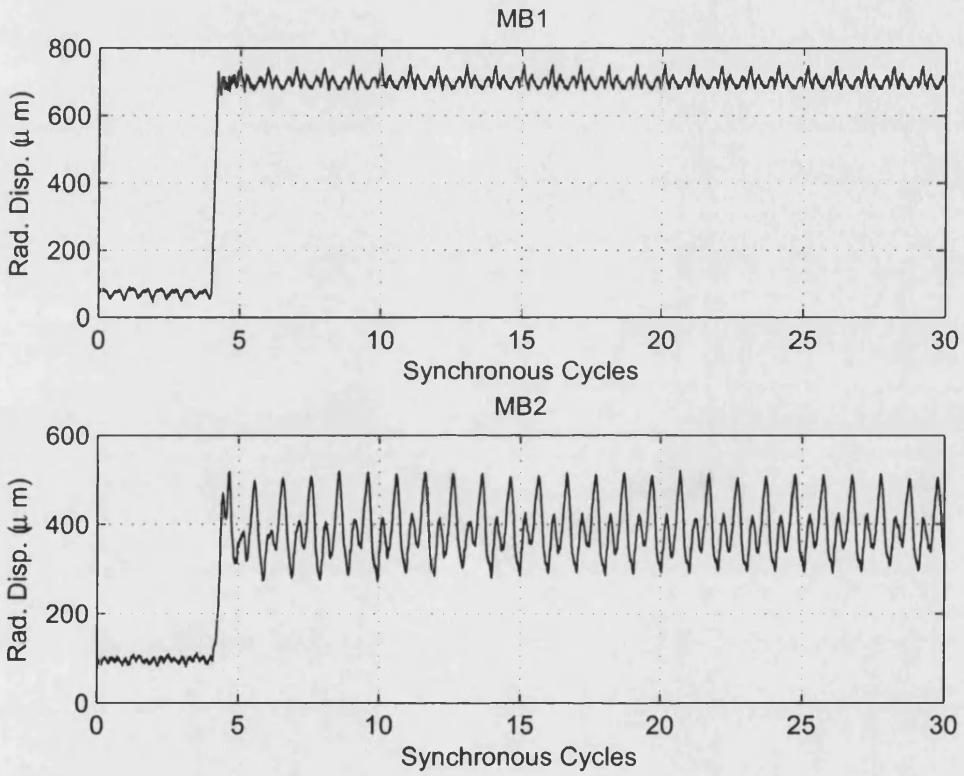

Figure 6.18: Measured radial displacements of the rotor with the application of the PID control forces at 12.5 Hz

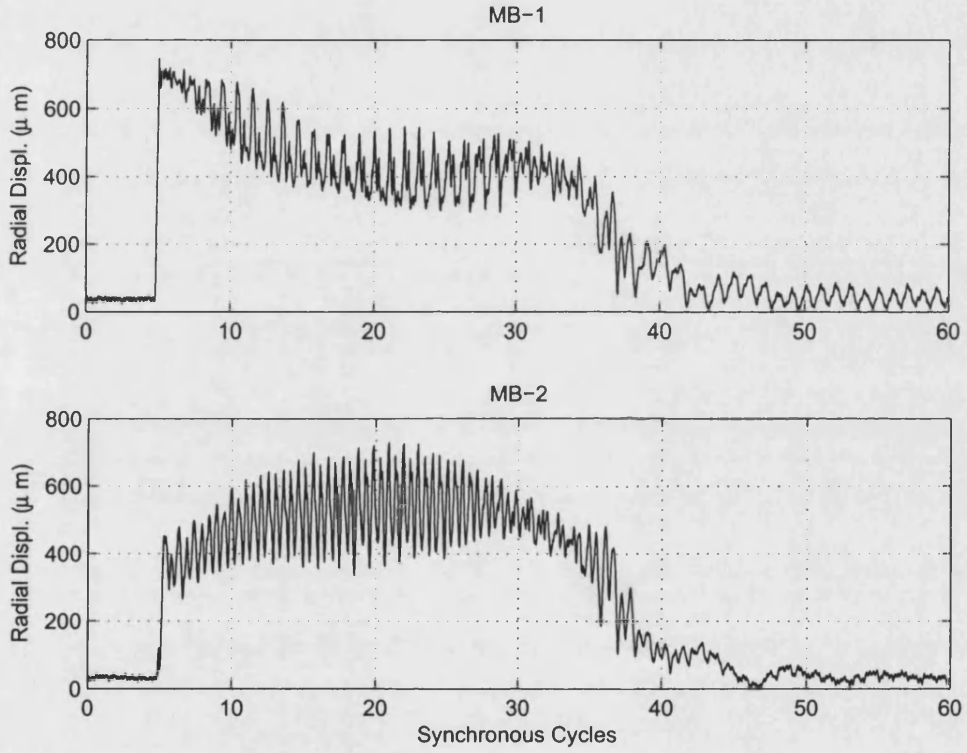

Figure 6.19: Measured radial displacements of the rotor with the application of the ROLAC forces at 12.5 Hz

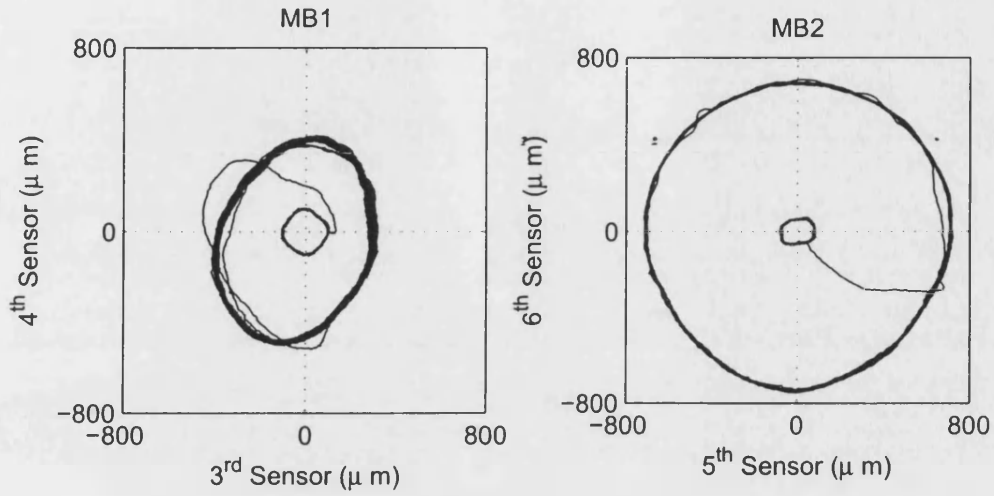

(a) PID only controller.

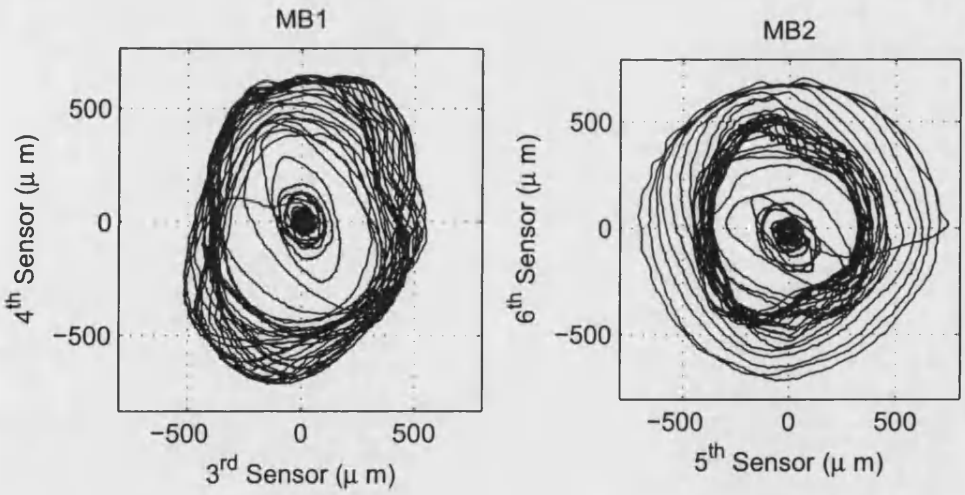

(b) PID+ROLAC

Figure 6.20: Experimental orbits at both magnetic bearing locations when a sudden synchronous force was applied through the magnetic bearings at 12.5 Hz

Chapter 7

Conclusions and Future Work

7.1 Conclusions

A computationally efficient computer model of a flexible rotor/magnetic bearing system when the rotor is in contact with the retainer bearings has been developed. The method does not require detailed modelling of the contact forces. Hence it eliminates the problem with conventional methods of modelling contact forces as non-linear functions of rotor penetration into the bearing inner surface at the contact point. The conventional techniques introduce numerical inefficiencies during the integration of the high order flexible rotor equations of motion and high numerical stiffness associated with the contact equation. The method presented in this thesis, based on the constrained Lagrangian formulation, overcomes these difficulties.

The suggested formulation is equivalent to rigid (infinitely stiff) contact. It is computationally efficient, but would over predict the contact force. The uncertainties can be embedded in the controller. Uncertainties exist in a conventional Hertzian modelling, which requires a mathematical model to represent the contact dynamics, also require quantitative value of model parameters. When roller element bearing are used as retainer bearings, their modelling would introduce further uncertainties. Moreover, the high frequency impulsive contact force generated by the high contact stiffness value will be filtered out by the flexible rotor dynamics, thereby reducing the apparent advantages of the classical approach.

Contacts are treated as constraints on the generalized coordinates on the system, and are incorporated into the system equations through the use of Lagrange multipliers. The use of a constrained Lagrangian multiplier effectively considers the retainer bearing to be a rigid boundary. However, the contact forces can be calculated from the constraint forces, which are automatically evaluated at each time step. The switching logic between contact and non-contact cases is developed based on the zero crossing values of the constraint equations and the constraint forces. The treatment of initial conditions is needed when starting the contact model. This technique is extended to cover multiple contacts cases. It is achieved by initiating the same constraint constraint equation at the other magnetic bearing position. In this way, there is no need to model each case separately. It is also possible to predict destructive backward whirl motion. The suggested modelling technique can detect the rolling mode by the introduction of another constraint and simulates it through an additional Lagrange multiplier.

Another factor for obtaining computational efficiency is the implementation of a model reduction technique when modelling the flexible rotor. It has been shown that it is best to use as many nodal planes as necessary in the finite element modelling for a required accuracy, and then apply the suggested model reduction technique (MSDC). The technique involves two stages, in the first stage the slave coordinates ($\mathbf{q_s}$) are eliminated in terms of the masters ($\mathbf{q_m}$) without loss of model accuracy, but in the second stage the Guyan reduction replacement is used to eliminate the first and second derivatives of the slaves.

The technique combines the system equations such that it represents the system with efficiency. The slaves states are eliminated in terms of the masters. The only assumption is that the salve state derivatives ($\dot{\mathbf{q}}_\mathbf{s}$, $\ddot{\mathbf{q}}_\mathbf{s}$) are zero. This gives superior accuracy compared with reducing the number of nodal planes in the finite element modelling. The reduced order model was shown to predict the first 8 natural frequencies to within 0.1% error compared with those from the full order model. The transient response due to step changes in unbalance was almost indistinguishable between the two cases.

The technique to reduce the order of a rotor finite element model for use in dynamic analysis has been demonstrated. The original model consisted of 52 rectilinear and angular degrees of freedom distributed over 13 nodal planes. For implementation in a magnetic bearing system, the minimum requirement of any rotor model is to allow sensor displacements to be predicted in 4 nodal planes and allow control forces to be applied in 2 further nodal planes. Thus a minimal reduced order model was derived to include 12 rectilinear displacements in 6

nodal planes. The reduction technique required careful choice of the master planes depending on the application. Thus, suitability of the reduction technique in the case of different applications must be examined.

The simulated rotor orbits for the full and reduced order models were again shown to be similar. Thus the potential benefits of using the more efficient reduced order model for future controlled design studies have been shown. This new modelling technique provides an efficient simulation environment to design and test controllers which are capable of recovering the rotor, and also predict constraint forces to assess the damage, and would be suitable for a real-time implementation.

A test rig consisting of a 100 kg and 2 m long flexible rotor with 4 disks, supported by two magnetic bearings, was simulated to study the behaviour of the rotor under single and multiple contacts, and to predict the contact force levels. Contacts were initiated by the introduction of sudden synchronous forces. The friction coefficient between the rotor and the inner surface of the retainer bearing during the contact has a significant effect on the behaviour of the rotor during the contact. For low friction coefficient cases, such as with rolling bearings, a forward whirl orbit is observed. The rotor can be recovered if the additional unbalance force is removed. At very high friction coefficient cases, such as with bush retainer bearings, it is possible to get a backward whirl, and to enter a destructive rolling mode. The suggested modelling technique can detect the rolling mode and simulates it through an additional Lagrange multiplier. It has been shown that once in this mode it is not possible to recover the rotor position even

if the external forces that caused the contact were removed.

Experimental work was undertaken using a flexible rotor/magnetic bearing system, which provides same validation of the modelling technique. Experimental results show single and multiple contact cases. Contacts were initiated by a sudden synchronous force introduced through the magnetic bearings. In all cases, the measured rotor responses were consistent with the simulation results, including the behaviour of the rotor after the removal of the synchronous forces.

The existing open loop adaptive controller has been extended in this thesis to allow an optimum control force to be updated at every sampling interval utilising a recursive Fourier transform algorithm. This recursive open loop adaptive controller (ROLAC) was examined in simulation and applied in real-time to the experimental system. The experimental results show the ability of ROLAC to attenuate vibration due to unknown out of balance forces and also to act quickly in case of sudden change of synchronous force. The controller is able to prevent contact in some cases and to recover rotor position if contact occurs.

7.2 Future Work

There are three main areas of consideration for future work:

- Measuring contact forces experimentally and comparing with the contact forces predicted by the constrained Lagrangian dynamic technique developed by the author in this thesis.
- Extending the recursive open loop adaptive controller (ROLAC) technique to cover multi-frequency excitation.
- Investigate the backward whirl case in more detail using the constrained Lagrangian approach, and validate by using experimental test, which was not possible with the existing experimental setup.

References

[1] S. Earnshaw, "On the nature of the molecular forces which regulate the constitution of the luminiferous ether," *Trans. Camb. Phil. Soc*, vol. 7, pp. 97–112, 1842.

[2] P. Budig and R. Werner, "Stiffness of magnetic bearings," *Proceedings of the Fourth International Symposium on Magnetic Bearings*, pp. 251–256, August 1994.

[3] G. Schwetizer and H. Ulbrich, "Magnetic bearings - a novel type of suspension," *Proceedings of the Second International Conference on Vibrations in Rotating Machinery*, pp. 151–156, 1980.

[4] H. Ulbrich, G. Schwetizer, and E. Bauser, "A rotor supported without contact - theory and application," *Proceedings of the Fifth World Congress on Theory of Machines and Mechanisms*, pp. 181–184, 1979.

[5] E. Brigham, *The Fast Fourier Transform and Its Application.* Prentice-Hall, Inc, 1988.

[6] M. E. F. Kasarda, "An overview of active magnetic bearing technology and

applications," *The Shock and Vibration Digest*, vol. 32, no. 2, pp. 91–99, 2000.

[7] G. Schweitzer, H. Bleuler, and A. Traxler, *Active Magnetic Bearings: Basics, Properties and Applications of Active Magnetic Bearings.* ETZ Zürich, 1994.

[8] G. Schweitzer, "Active magnetic bearings -chances and limitations," *Proceedings of the Sixth International Conference on Rotor Dynamics*, vol. 1, pp. 1–14, 2002.

[9] G. Schweitzer, "Mechatronics for the design of human-oriented machines," *IEEE/ASME Transactions on Mechatronics*, vol. 1, no. 2, pp. 120–126, 1996.

[10] A. Nakajima, "Research and development of magnetic bearing flywheels for attitude of spacecraft," *Proceedings of the Fourth International Symposium on Magnetic Bearings*, pp. 3–12, June 1988. ETH Zürich, Switzerland.

[11] K. L. McLallin, R. H. Jansen, J. Fausz, and R. D. Bauer, "Aerospace flywheel technology development for IPACS applications," *The 36th Intersociety Energy Conversion Engineering Conference*, 2002. NASA Report No. IECEC2001AT82.

[12] S. Sivrioglu, K. Nonami, and M. Saigo, "Low power consumption non-linear control with H_∞ compensator for a zero-bias flywheel AMB system," *Journal of Vibration and Control*, vol. 10, pp. 1151–1166, Aug 2004.

[13] D. J. Clark, M. J. Jansen, and G. T. Montague, "An overview of magnetic bearing technology for gas turbine engines," *National Aeronautics and Space Administration*, 2004. NASA Report No. ARLTR3254.

[14] C. R. Knospe, "Active magnetic bearing for machining applications," *In Press, Control Engineering Practice*, 2006.

[15] M. Brunet, "Practical application of the active magnetic bearings to the industrial world," *Proceedings of the First International Symposium on Magnetic Bearings*, pp. 225–244, June 1988. ETH Zürich, Switzerland.

[16] M. Dussaux, "The industrial application of the active magnetic bearings technology," *Proceedings of the Second International Symposium on Magnetic Bearings*, pp. 33–38, July 1990. Tokyo, Japan.

[17] R. Schoeb and K. Dasse, "Magnetic suspension systems for biomedical applications," *Sixth International Symposium on Magnetic Suspension Technology*, October 2001. Turin, Italy.

[18] J. Lee, P. E. Allaire, G. Tao, J. A. Decker, and X. Zhang, "Experimental study of sliding mode control for a benchmark magnetic bearing system and artificial heart pump suspension," *IEEE Transaction on Control Systems Technology*, vol. 11, no. 1, pp. 128–138, 2003.

[19] C. R. Knospe and E. G. Collins, "Introduction to the special issue on magnetic bearing control," *IEEE Transactions on Control systems Technology*, vol. 4, no. 5, 1996.

[20] C. R. Burrows, P. S. Keogh, and R. Tasaltin, "Closed-loop vibration control of flexible rotors: an experimental study," *Proc. Instn. Mech. Engs. Part C*, vol. 207, pp. 1–17, 1993.

[21] C. R. Knospe, R. W. Hope, S. T. Fedigan, and R. D. Williams, "Experiments

in the control of unbalance response using magnetic bearings," *Mechatronics*, vol. 5, no. 4, pp. 385–400, 1995.

[22] A. G. Abulrub, M. N. Sahinkaya, C. R. Burrows, and P. S. Keogh, "Adaptive control of active magnetic bearings to prevent rotor-bearing contact," *ASME International Mechanical Engineering Congress and Exposition*, 5-10, November 2006. Chicago, Illinois.

[23] C. Ehmann, P. Kytka, and R. Nordmann, "Comparison of PID-, LQR-, and μ-synthesis control for the electromagnetic suspension of a flexible rotor," *The Seventh International Conference on Motion and Vibration Control*, pp. 1–10, 2004.

[24] A. E. Hartavi, O. Ustun, and R. N. Tuncay, "A compartive approach on PD and fuzzy control of AMB using RCP," *International Electric Machines and Drives Conference, IEMD'03*, vol. 3, pp. 1507–1510, 2003.

[25] S. Yu, S. Wu, and T. Lee, "Optimal fuzzy control of radial active magnetic bearing systems," *Proceedings IEEE International Symposium on Computational Intelligence in Robotics and Automation*, vol. 8, pp. 1393–1398, July 16-20 2003. Kobe, Japan.

[26] S. Hong and R. Langari, "Robust fuzzy control of a magnetic bearing system subject to harmonic disturbances," *IEEE Transactions on Control Systems Technology*, vol. 8, no. 2, pp. 366–371, 2000.

[27] M. N. Sahinkaya, A. E. Hartavi, C. R. Burrows, and R. N. Tuncay, "Bias current optimisation and fuzzy controllers for magnetic bearings in turbo

molecular pumps," *Ninth International Symposium on Magnetic Bearings*, vol. 8, pp. 1–6, August 3-6 2004. Lexington, Kentucky, USA.

[28] P. Schroder, B. Green, N. Grum, and P. J. Fleming, "On-line genetic auto-tuning of mixed H_2/H_∞ optimal magnetic bearing controllers," *Proceedings of Control'98*, 1998. Swansea, England.

[29] K. Nakashima, T. Tsujino, and T. Fujii, "Multivariable control of a magnetic levitation system using closed loop identification and H_∞ control theory," *Proceedings of the 35th Conference on Decision and Control*, September 1996. Kobe, Japan.

[30] H. Kwakernaak, "Robust control and H_∞-optimization–tutorial paper," *Automatica*, vol. 29, no. 2, pp. 255–273, 1993.

[31] M. O. T. Cole, P. S. Keogh, M. N. Sahinkaya, and C. R. Burrows, "Towards fault-tolerant active control of rotor-magnetic bearing systems," *Control Engineering Practice*, vol. 12, pp. 491–501, Apr 2004.

[32] P. S. Keogh, M. O. T. Cole, and C. R. Burrows, "Multi-state transient rotor vibration control using sampled harmonics," *Transaction of the ASME, Journal of Vibration and Acoustics*, vol. 124, pp. 186–197, 2002.

[33] S. Sivrioglu and K. Nonami, "LMI approach to gain scheduled H_∞ control beyond PID control for gyroscopic rotor-magnetic bearing systems," *Proceedings of the 35th conference on decision and control*, pp. 3694–3699, 1995.

[34] M. R. Bai and K. Ou, "Experimental evaluation of adaptive predictive con-

trol for rotor vibration suppression," *IEEE Transaction on Control Systems Technology*, vol. 10, no. 6, pp. 895–901, 2002.

[35] F. Betschon and C. R. Knospe, "Reducing magnetic bearing currents via gain scheduled adaptive control," *IEEE/ASME Transaction on Mechatronics*, vol. 6, no. 4, pp. 437–443, 2001.

[36] C. R. Knospe, R. W. Hope, S. J. Fedigan, and R. D. Williams, "New results in the control of rotor synchronous vibration," *Fourth International Symposium on Magnetic Bearings*, pp. 119–124, 1994.

[37] C. R. Burrows and M. N. Sahinkaya, "Vibration control of multi-mode rotor-bearing systems," *Proc. R. Soc. Lond, A 386*, pp. 77–94, 1983.

[38] C. R. Burrows, M. N. Sahinkaya, and S. Clements, "Active vibration control of flexible rotors: an experimental and theoretical study," *Proc. R. Soc. Lond, A 422*, pp. 123–146, 1989.

[39] M. N. Sahinkaya, M. O. T. Cole, and C. R. Burrows, "Fault detection and tolerance in synchronous vibration control of rotor-magnetic bearing systems," *Proc. Instn. Mech. Engs. Part C*, vol. 215, pp. 1401–1416, 2001.

[40] N. Bachschmid, P. Pennacchi, and A. Vania, "Identification of multiple faults in rotor systems," *Journal of Sound and Vibration*, vol. 254, no. 2, pp. 327–366, 2002.

[41] N. S. Vyas and D. Satishkumar, "Artificial neural network design for fault identification in a rotor-bearing system.," *Mech. Syst. Signal Process.*, vol. 36, pp. 157–175, 2001.

[42] P. S. Keogh, M. O. T. Cole, M. N. Sahinkaya, and C. R. Burrows, "On the control of synchronous vibration in rotor/magnetic bearing systems involving auxiliary bearing contact," *Journal of Engineering for Gas Turbines and Power*, vol. 126, no. 2, pp. 366–372, 2004.

[43] A. G. Abulrub, M. N. Sahinkaya, P. S. Keogh, and C. R. Burrows, "Contact dynamics and recursive open loop adaptive controller to recover rotor," *The Tenth International Symposium on Magnetic Bearings*, 21-23, August 2006. Martigny, Switzerland.

[44] M. O. T. Cole, P. S. Keogh, and C. R. Burrows, "Prediction on the dynamic behaviour of a rolling element auxiliary bearing for rotor/amb systems," *8th International Symposium on Magnetic Bearing*, August 26-28 2002. Mito, Japan.

[45] A. Vania and P. Pennacchi, "Experimental and theoretical application of fault identification measures of accuracy in rotating machine diagnostics.," *Mech. Syst. Signal Process.*, vol. 18, no. 2, pp. 329–352, 2004.

[46] G. Schweitzer, "Safety and reliability aspects for active magnetic bearing applications a survey," *Proc. Instn. Mech. Engs. Part I*, vol. 219, pp. 383–392, 2005.

[47] P. S. Keogh and W. Y. Yong, "Thermal assessment of dynamic rotor/auxiliary bearing contact events," *Accepted in ASME J. Tribology*, 2006.

[48] T. W. Reitsma, "Development of long-life auxiliary bearing for critical services turbomachinary and high-speed motors," *8th International Symposium on Magnetic Bearing*, August 26-28 2002. Mito, Japan.

[49] G. Sun, "Auxiliary bearing life prediction using Hertzian contact bearing model," *Transaction of the ASME, Journal of Vibration and Acoustics*, vol. 128, pp. 203–209, 2006.

[50] H. Xie, G. T. Flowers, L. Feng, and G. Lawrence, "Steady-state dynamic behavior of a flexible rotor with auxiliary support from a clearance bearing.," *Transaction of ASME, Journal of Vibration ans Acoustics.*, vol. 121, pp. 78–83, 1999.

[51] P. S. Keogh and M. O. T. Cole, "Rotor vibration with auxiliary bearing contact in magnetic bearing systems Part1: Synchronous dynamics," *Proc. Instn. Mech. Engs. Part C*, vol. 217, pp. 377–392, 2003.

[52] P. S. Keogh, C. Mu, and C. R. Burrows, "Optimised design of vibration controllers for steady and transient excitation of flexible rotors," *Proc. Instn. Mech. Engs., Part C*, vol. 218, pp. 155–168, 1995.

[53] M. N. Sahinkaya, A. G. Abulrub, and P. S. Keogh, "Performance of synchronous controllers for rotor magnetic bearing systems under retainer bearing contact," *The Seventh International Conference on Motion and Vibration Control*, 8-11 August 2004. St.Louis, USA.

[54] M. O. T. Cole and P. S. Keogh, "Rotor vibration with auxiliary bearing contact in magnetic bearing systems Part2: Robust sunchronous control for rotor position recovery," *Proc. Instn. Mech. Engs. Part C*, vol. 217, pp. 393–409, 2003.

[55] F. F. Ehrich, "High order subharmonic response of high speed rotors in

bearing clearance," *Journal of vibration, Acoustics, Stress and Reliability in Design*, vol. 110, pp. 9–16, 1988.

[56] A. Muszynska, "Partial lateral rotor to stator rubs," *IMechE, International Conference on Vibrations of Rotating Machinery*, pp. 327–335, 1984. London.

[57] D. W. Childs, "Rub-induced parametric excitation in rotors," *Transaction of the ASME, Journal of Mechanical Design*, vol. 101, pp. 640–644, 1979.

[58] D. C. Johnson, "Synchronous whirl of a vertical shaft having clearance inone bearing," *Journal Mechanical Engineering Scienec*, vol. 4, no. 1, pp. 85–93, 1962.

[59] J. Schmied and J. C. Pradetto, "Behaviour of a one ton rotor beaing dropped into auxiliary bearings," *3rd International Symposium on Magnetic Bearing*, pp. 145–156, 1992. Alexandria, USA.

[60] G. T. Flowers and F. S. Wu, "A study of the influence of bearing clearance on lateral coupled shaft/disk rotordynamics," *Transaction of the ASME, Journal of Engineering for Gas Turbines and Power*, vol. 115, pp. 279–286, 1993.

[61] F. Wu and G. T. Flowers, "An experimental study of the influence of disk flexibility and rubbing on rotordynamics," *Proceedings ASME Conference on Vibration of Rotating Systems*, vol. 60, September 1993.

[62] J. L. Lawen and G. T. Flowers, "Synchronous dynamics of a coupled shaft/bearing/housing system with auxiliary support from a clearance bearing: analysis and experiment," *NASA report, N95-23214*, pp. 1–8.

[63] R. G. Kirk, K. V. S. Raju, and K. Ramesh, "Modelling of AMB turbomachinery for transient analysis.," *in Proceedings of MAG97.*, pp. 139–153, 1997. Alexandria, USA.

[64] B. O. Bedoor, "Transient torsional and lateral vibrations of unbalanced rotors with rotor-to-stator rubbing," *Journal of Sound and Vibration*, vol. 229, no. 3, pp. 627–645, 2000.

[65] M. Fumagalli and G. Schwetizer, "Measurements ona rotor contacting its houseing.," *Proceedings of Inst. Mech. Engrs. 6th International Conference on Vibration in Rotating Machinery.*, 1996. Paper No. C500/085/96. Alexandria, USA.

[66] G. VonGroll and D. J. Ewins, "A mechanism of low subharmonic response in rotor/stator contact-measurements and simulations.," *Transaction of ASME, Journal of Vibration ans Acoustics.*, vol. 124, pp. 350–358, 2002.

[67] G. Gilardi and I. Sharf, "Literature survey of contact dynamics modelling," *Mechanism and Machine Theory.*, vol. 37, pp. 1213–1239, 2002.

[68] X. wang and S. Noah, "Nonlinear dynamics of a magnetically supported rotor on safety auxiliary bearing," *Transactions of ASME, Journal of Vibration and Acoustics*, vol. 120, pp. 596–606, 1998.

[69] R. G. Kirk, "Evaluation of AMB turbomachinery auxiliary bearings," *Transaction of ASME, Journal of Vibration ans Acoustics.*, vol. 121, pp. 156–161, 1999.

[70] R. G. Kirk, K. V. Raju, and K. Ramesh, "Evaluation of AMB rotor drop

stability," *Virginia Polytechnic Inst. and State Univ , Rotordynamic Instability Problems in High-Performance Turbomachinery*, pp. 197–208, 1996.

[71] R. G. Kirk, E. E. Swanson, F. H. Kavarana, X. Wang, and J. Keesee, "Rotor drop test stand for AMB rotating machniery Part I: Descrption of test stand and initial results," *Fourth International Symposium on Magnetic Bearings*, pp. 207–212, August 1994.

[72] K. Ramesh and R. G. Kirk, "Rotor drop test stand for AMB rotating machniery Part II: Steady state analysis and comparison to experimental results," *Fourth International Symposium on Magnetic Bearings*, pp. 213–218, August 1994.

[73] T. Ishii and R. G. Kirk, "Transient response technique applied to active magnetic bearing machinery during rotor drop.," *Transaction of ASME, Journal of Vibration ans Acoustics.*, vol. 118, pp. 154–163, 1996.

[74] L. Ginzinger and H. Ulbrich, "Control of a rubbing rotor - experiments and theory," *The 11th International Symposium on Transport Phenomena and Dynamics of Rotating Machinery*, pp. 1–8, 2006. Honolulu, Hawaii, USA.

[75] H. Ulbrich, A. Chavez, and R. Dhima, "Minimization of contact forces in case of rotor rubbing using an actively controlled auxiliary bearing," *The 10th International Symposium on Transport Phenomena and Dynamics of Rotating Machinery*, pp. 1–10, 2004. Honolulu, Hawaii, USA.

[76] J. Ahrens and H. Ulbrich, "Determination of contact forces during rubbing considering blade dynamics," *Proceedings of the International Symposium on Stability Control of Rotating Machinery*, pp. 1–10, 2001. California, USA.

[77] S. Faik and H. Witteman, "Modelling of impact dynamics: A literature survey," *Proceedings International ADAMS User Interface Conference*, 2000.

[78] H. Olsson, C. W. K. Åström, M. Gäfvert, and P. Lischinsky, "Friction models and friction compensation," *European Journal of Control,*, vol. 4, pp. 176–195, 1998.

[79] N. Rutland and P. S. Keogh, "Design procedure for an active magnetic bearing," Tech. Rep. 029/1994, University of Bath, England, June 1994.

[80] N. Rutland and P. S. Keogh, "Experimental validation of active magnetic bearing force characteristics," Tech. Rep. 032/1995, University of Bath, England, May 1995.

[81] N. Rutland and P. S. Keogh, "Design of an experimental rotor and active magnetic bearing rig," Tech. Rep. 030/1994, University of Bath, England, June 1994.

[82] H. D. Nelson and J. M. McVaugh, "The dynamics of rotor-bearing systems using finite elemnets," *ASME J. Eng. Ind.*, vol. 98, pp. 561–580, 1976.

[83] A. G. Abulrub, M. N. Sahinkaya, P. S. Keogh, and C. R. Burrows, "Effective model reduction for magnetically levitated flexible rotors including contact dynamics," *Proceedings of ASME 2005 International Design Engineering Technical Conferences and Computers and Information in Engineering Conference*, 24-28 Sep 2005. Long Beach, USA.

[84] J. B. Vernon, *Linear vibration theory, generalized properties and numerical methods.* New York: John wiles & Sons, Inc, 1967.

[85] C. R. Burrows and M. N. Sahinkaya, "Parameter estimation of multi-mode rotor-bearing systems," *Proc. R. Soc. Lond, A 379*, pp. 367–387, 1982.

[86] R. J. Guyan, "Reduction of stiffness and mass matrices," *AIAA Journal*, vol. 3, p. 380, 1965.

[87] Z.-Q. Qu, Y. Jung, and R. P. Selvam, "Model condensation for non-classically damped systems - Part I: Static condensation," *Mechanical Systems and Signal Processing*, vol. 17, no. 5, pp. 1003–1016, 2003.

[88] F. Zhi-chu, "Study on catastrophic mechanism for rotor drop transient vibration following magnetic bearing failure.," *Applied Mathematics and Mechanics.*, vol. 23, no. 11, pp. 1319–1325, 2002.

[89] M. L. Adams, F. Afshari, and M. L. Adams, "An experiment to measure the restitution coefficient for rotor-stator impacts.," *Proceedings of Inst. Mech. Engrs. 7th International Conference on Vibration in Rotating Machinery.*, 2000. Paper No. C576/080/2000. Alexandria, USA.

[90] G. Wegener and R. Markert, "Influence of contact and impacts on the dynamics of an elastic rotor with an elastic retainer bearing," *Dynamics of Vibro-Impact Systems- Proceedings of the EUROMECH Colloquium*, 1998.

[91] M. F. Ashby and D. R. Johnes, *Engineering materials an introduction to their properties and applications.* Pergamon Press Ltd., Oxford, 1985.

[92] S. C. Lim and M. F. Ashby, "Wear-mechanism maps," tech. rep., Cambridge University, 1986.

[93] R. Stanway and C. R. Burrows, "Experimental study of input transducer dynamics in bearing identification," *Winter Annual Meeting ASME*, pp. 1–7, December 1978. Calif. paper 78-WA/DSC-6.

[94] C. R. Burrows, R. Sayed-Esfahani, and R. Stanway, "A comparison of multifrequency techniques for measuring the dynamics of squeeze-film bearings," *Transaction of the ASME, Journal of Lubrication Technology*, vol. 103, pp. 137–143, 1981.

[95] M. N. Sahinkaya, M. O. T. Cole, and C. R. Burrows, "On the use of Schroeder phased harmonic sequences in multi-frequency vibration control of flexible rotor/magnetic bearing systems," *The 8th international symposium on magnetic bearings*, 2002. Mito, Japan.

[96] C. R. Burrows, "An appraisal of Schroeder-phased harmonic signals for bearing identification," *Winter Annual Meeting, ASME*, pp. 1–10, 1980. Chicago, Paper 80-WA/DSC-34.

[97] M. N. Sahinkaya and C. R. Burrows, "Estimation of linearized oil-film parameters from the out-of-balance response," *Proc. Instn. Mech. Engrs., Part C*, vol. 198, no. 8, pp. 131–135, 1984.